




8-2011

## **Dynamics of polymeric solutions in complex kinematics bulk and free surface flows: Multiscale/Continuum simulations and experimental studies**

Arash Abedijaberi  
aabedija@utk.edu

Follow this and additional works at: [https://trace.tennessee.edu/utk\\_graddiss](https://trace.tennessee.edu/utk_graddiss)

 Part of the [Complex Fluids Commons](#), and the [Transport Phenomena Commons](#)

---

### **Recommended Citation**

Abedijaberi, Arash, "Dynamics of polymeric solutions in complex kinematics bulk and free surface flows: Multiscale/Continuum simulations and experimental studies. " PhD diss., University of Tennessee, 2011.  
[https://trace.tennessee.edu/utk\\_graddiss/1050](https://trace.tennessee.edu/utk_graddiss/1050)

This Thesis is brought to you for free and open access by the Graduate School at TRACE: Tennessee Research and Creative Exchange. It has been accepted for inclusion in Doctoral Dissertations by an authorized administrator of TRACE: Tennessee Research and Creative Exchange. For more information, please contact [trace@utk.edu](mailto:trace@utk.edu).

To the Graduate Council:

I am submitting herewith a thesis written by Arash Abedijaberi entitled "Dynamics of polymeric solutions in complex kinematics bulk and free surface flows: Multiscale/Continuum simulations and experimental studies." I have examined the final electronic copy of this thesis for form and content and recommend that it be accepted in partial fulfillment of the requirements for the degree of Doctor of Philosophy, with a major in Chemical Engineering.

Bamin Khomami, Major Professor

We have read this thesis and recommend its acceptance:

Brian J. Edwards, Shanfeng Wang, Ramki Kalyanaraman

Accepted for the Council:

Carolyn R. Hodges

Vice Provost and Dean of the Graduate School

(Original signatures are on file with official student records.)

**Dynamics of polymeric solutions in  
complex kinematics bulk and free  
surface flows:  
Multiscale/Continuum simulations  
and experimental studies**

A Thesis Presented for  
The Doctor of Philosophy  
Degree  
The University of Tennessee, Knoxville

Arash Abedijaberi

August 2011

© by Arash Abedijaberi, 2011  
All Rights Reserved.

*I dedicate this thesis to my wife, Kaishiuan, and my mother whose supports and encouragements are so constant that they are too often taken for granted.*

# Acknowledgements

I would like to express my sincere gratitude to my advisor Dr. Bamin Khomami for being an inexhaustible source of ideas and inspiration during the course of this work. I appreciate his patience and expert guidance in revisions of manuscripts that were prepared during the research period. I would also like to thank him for his unconditional support and timely advices on my personal problems and career decisions which have been extremely informative and beneficial.

I gratefully acknowledge the financial support of my graduate studies provided by research grants from National Science Foundation (NSF) and fellowships from University of Tennessee in Knoxville (UTK).

# Abstract

While rheological and microstructural complexities have posed tremendous challenges to researchers in developing first principles models and simulation techniques that can accurately and robustly predict the dynamical behaviour of polymeric flows, the past two decades have offered several significant advances towards accomplishing this goal. These accomplishments include: (1). Stable and accurate formulation of continuum-level viscoelastic constitutive models and their efficient implementation using operator splitting methods to explore steady and transient flows in complex geometries, (2). Prediction of rheology of polymer solutions and melts based on micromechanical models as well as highly parallel self-consistent multiscale simulations of non-homogeneous flows. The main objective of this study is to leverage and build upon the aforementioned advances to develop a quantitative understanding of the flow-microstructure coupling mechanisms in viscoelastic polymeric fluids and in turn predict, consistent with experiments, their essential macroscopic flow properties e.g. frictional drag, interface shape, etc. To this end, we have performed extensive continuum and multiscale flow simulations in several industrially relevant bulk and free surface flows. The primary motivation for the selection of the specific flow problems is based on their ability to represent different deformation types, and the ability to experimentally verify the simulation results as well as their scientific and industrial significance.

# Contents

<b>List of Tables</b>	<b>ix</b>
<b>List of Figures</b>	<b>x</b>
<b>1 Introduction</b>	<b>1</b>
<b>2 Problem Formulation</b>	<b>4</b>
2.1 Constitutive Equations . . . . .	5
2.1.1 Oldroyd-B model . . . . .	6
2.1.2 FENE-P Model . . . . .	6
2.1.3 FENE-CR Model . . . . .	7
2.1.4 Giesekus Model . . . . .	8
2.2 Kinetic Theory Based Elastic Models . . . . .	9
2.3 Computational Technique . . . . .	10
<b>3 Flow of branched polymer melts in a lubricated cross-slot channel: a combined computational and experimental study</b>	<b>12</b>
3.1 Introduction . . . . .	12
3.2 Flow birefringence of polymer melts . . . . .	14
3.3 Problem formulation . . . . .	16
3.4 Experiment . . . . .	18
3.4.1 Experimental Setup . . . . .	18
3.4.2 Fluids and its Rheological Characterization . . . . .	21

3.5	Results . . . . .	24
3.5.1	Determination of the Slip Velocity . . . . .	24
3.5.2	Results at Moderate Weissenberg Numbers ( $We = 21$ ) . . . . .	26
3.5.3	Results at Large Weissenberg Numbers ( $We = 29$ ) . . . . .	27
3.6	Conclusion . . . . .	28
<b>4</b>	<b>Continuum and multi-scale simulation of mixed kinematics polymeric flows with stagnation points: closure approximation and the high Weissenberg number problem</b>	<b>32</b>
4.1	Introduction . . . . .	32
4.2	Problem formulation . . . . .	36
4.2.1	Domain discretization and boundary conditions . . . . .	36
4.3	Results and discussion . . . . .	38
4.3.1	Solution Accuracy . . . . .	38
4.3.2	Simulation results . . . . .	43
4.4	Conclusion . . . . .	54
<b>5</b>	<b>Sedimentation of a sphere in a viscoelastic fluid: a multiscale simulation approach</b>	<b>55</b>
5.1	Introduction . . . . .	55
5.2	Problem Formulation . . . . .	58
5.2.1	Domain discretization and boundary conditions . . . . .	58
5.3	Fluid Rheology . . . . .	60
5.4	Results and discussion . . . . .	64
5.4.1	Solution accuracy . . . . .	64
5.4.2	Comparison of computed and experimentally measured drag correction factor . . . . .	65
5.4.3	Elastic Effects on the Structure of the Wake . . . . .	79
5.5	Conclusion . . . . .	82

<b>6</b>	<b>A computational study of the influence of viscoelasticity on the interfacial dynamics of dip coating flow</b>	<b>83</b>
6.1	Introduction . . . . .	83
6.2	Problem Formulation . . . . .	88
6.2.1	Boundary Conditions . . . . .	92
6.2.2	Finite Element Formulation of the Governing Equations . . .	94
6.2.3	Free Boundary Formulation . . . . .	95
6.2.4	Boundary conditions on mesh deformation . . . . .	96
6.2.5	Mesh Convergence . . . . .	98
6.3	Results . . . . .	99
6.3.1	Low $Ca$ . . . . .	99
6.3.2	Moderate $Ca$ . . . . .	105
6.4	Conclusion . . . . .	114
<b>7</b>	<b>Plunging of solid surfaces into Newtonian and viscoelastic fluids: an experimental/numerical study</b>	<b>122</b>
7.1	Introduction . . . . .	122
7.2	Experiment . . . . .	123
7.3	Problem formulation and numerical technique . . . . .	124
7.3.1	Mesh Convergence . . . . .	124
7.4	Results and discussion . . . . .	125
7.4.1	Newtonian wet plunging flow . . . . .	127
7.4.2	Effect of fluid elasticity . . . . .	136
7.5	Conclusion . . . . .	140
<b>8</b>	<b>Summary and future work</b>	<b>144</b>
	<b>Bibliography</b>	<b>148</b>
	<b>Vita</b>	<b>165</b>

# List of Tables

3.1	Giesekus parameters: $\eta_i$ , $\lambda_i$ , obtained from linear viscoelasticity data and $\alpha_i$ from steady shear and transient uniaxial extensional data. . .	23
4.1	Degrees of freedom (DOF) for each variable and the ratio of the width of the smallest element of each mesh to the sphere radius. . . . .	40
4.2	Degrees of freedom (DOF) for each variable and the ratio of the width of the smallest element of each mesh to the cylinder radius. . . . .	40
5.1	Degrees of freedom (DOF) for each variable and the ratio of the width of the smallest element of each mesh to the sphere radius. . . . .	59
5.2	Linear viscoelastic properties of the Boger fluid composed of 0.21 wt.% polyisobutylene (PIB), 4.83 wt.% tetradecane (C14), and 94.86 wt.% polybutene (PB). . . . .	62
6.1	Convergence studies: Maximum $We$ attained for fixed $Ca$ and $Bo$ . .	99

# List of Figures

3.1	Schematic view of the computational domain of the cross-slot flow channel. . . . .	17
3.2	Finite element meshes with a) 3492 b) 4500, and c) 6400 elements. (cross-slot flow channel). . . . .	18
3.3	Experimental setup: the cross-slot flow channel is attached to an XYtranslation stage whereas the flow-induced birefringence optical elements are mounted on a fixed stone support plate. . . . .	19
3.4	Storage (open symbols) and loss (full symbols) module at $170^{\circ}C$ together with the calculated spectrum predictions (full lines). . . . .	22
3.5	Steady shear viscosity (open circle symbols), first (full circle symbols) and second (full square symbols) normal stress difference at $170^{\circ}C$ together with the Giesekus model predictions (open square symbols for the second normal stress difference and full lines for the shear viscosity and the first normal stress difference). . . . .	22
3.6	Uniaxial extensional viscosity (open symbols) measured at $170^{\circ}C$ together with the Giesekus model predictions (full lines). Hencky strain rate range: 0.88, 0.25, 0.1, 0.028, and $0.00971 [s^{-1}]$ . . . . .	23

3.7	a) Velocity profile, b) shear stress profile, and c) normal stress profile at $We = 21$ in the channel fully developed inflow region: experimental data (open circles), computational results using no-slip (solid line) and slip (dotted line) boundary conditions with a slip velocity of $u_{slip} = 5.6$ mm/s. . . . .	24
3.8	a) Velocity profile, b) shear stress profile, and c) normal stress profile in the fully developed region at $We = 21$ for different imposed slip velocities $u_{slip}$ at the channel lateral walls. . . . .	26
3.9	Comparison between the birefringence data and the viscoelastic flow simulation using the Giesekus model in the a) inflow and b) outflow channels at $We = 21$ . . . . .	29
3.10	Comparison between the birefringence data and the viscoelastic flow simulation using the Giesekus model in the a) inflow and b) outflow channels at $We = 29$ . . . . .	30
4.1	Schematic of the sedimentation of a sphere in a tube and flow past a cylinder in a channel. . . . .	37
4.2	The computational domain near the surface of the sphere for meshes with 3022 elements, (a), 7500 elements (b) and 18898 elements, (c), $\chi = 0.128$ ; Computational domain near the surface of cylinder for meshes with 2428 elements, (d), 4280 elements, (e) and 17763 elements, (f), $\chi = 0.5$ . . . . .	39
4.3	Comparison of prototypical steady state $\tau_{pzz}$ profiles for the FENE, (a) and (c), and the FENE-P, (b) and (d), models predicted using self-consistent simulations, solid line, Lagrangian-based integration, circles, and FENE-P BCF, dotted line, along streamlines shown in (e) and (f) the surface of the sphere ( (a) and (b) and cylinder ((c) and (d)). . .	42

4.4	(a): $\tau_{p_{zz}}$ vs. $We$ , (b): $d\tau_{p_{zz}}/ds$ vs. $We$ , (c): $\tau_{p_{zz}}$ along the cylinder surface and channel center line. (d): $d\tau_{p_{zz}}/ds$ vs. $b$ (e): $d\tau_{p_{zz}}/ds$ , along the cylinder surface and channel center line. (f) Probability density function (PDF) of nondimensionalized end-to-end distance $ \vec{Q} /b$ . (All the results are at $We = 1.1$ , $b = 900$ and from the mesh $E = 17378$ otherwise mentioned.) . . . . .	45
4.5	(a): $\tau_{p_{zz}}$ and $d\tau_{p_{zz}}/ds$ vs $We$ and (b) Probability density function (PDF) of nondimensionalized end-to-end distance $ \vec{Q} /b$ predicted by the FENE and the FENE-P models. . . . .	46
4.6	(a): $\tau_{p_{zz}}$ vs. $We$ , (b): $d\tau_{p_{zz}}/ds$ vs. $We$ , (c): $\tau_{p_{zz}}$ along the sphere surface and tube center line. (d): $d\tau_{p_{zz}}/ds$ vs. $b$ (e): $d\tau_{p_{zz}}/ds$ , along the sphere surface and tube center line. (f) Probability density function (PDF) of nondimensionalized end-to-end distance $ \vec{Q} /b$ . (All the results are at $We = 2.0$ and from the mesh $E = 18898$ unless otherwise noted.) . .	49
4.7	Probability density function (PDF) of nondimensionalized end-to-end distance $ \vec{Q} /b$ at the point of maximum stress near the rear stagnation point of sphere (a) and cylinder (b). Velocity and stress in the $z$ direction ( $\vec{U}$ and $\tau_{p_{zz}}$ ), along the center line of the tube/channel near the rear stagnation point of the sphere (c) and (d), and cylinder (e) and (f) . . . . .	50
4.8	Probability density function (PDF) of end-to-end distance of polymer molecules along the surface of the sphere predicted by the FENE-P and the FENE models. (a): The location of point along streamline where the PDF's have been calculated. . . . .	51
4.9	Velocity in the $z$ direction ( $\vec{U}$ ), along the center line of the tube near the rear stagnation point of the sphere predicted by the FENE-P,(a,b), and the FENE,(c,d), models. . . . .	52
4.10	Streamlines near the rear stagnation point at $We = 2, 5$ ; a,b FENE-P; c,d, FENE . . . . .	53

5.1	Schematic of the sedimentation of a sphere in a tube; $\chi = a/R$ . . . .	59
5.2	The computational domain near the surface of the sphere for meshes with 3022 elements, (a), 7500 elements (b) and 18898 elements, (c). .	60
5.3	The fluid rheology of the Boger fluid composed of 0.21 wt.% polyisobutylene (PIB), 4.83 wt.% tetradecane (C14), and 94.86 wt.% polybutene (PB) at $25^\circ C$ including (a) $\eta$ vs $\dot{\gamma}$ , $\psi_1$ vs $\dot{\gamma}$ , $\eta'$ vs $\omega$ , and $\eta''/\omega$ vs $\omega$ ., (b) $\eta^E/\eta_0$ vs $\epsilon$ at $\dot{\epsilon} = 1.53s^{-1}$ , (c) $\eta^E/\eta_0$ vs $\epsilon$ at $\dot{\epsilon} = 2.17s^{-1}$ and (d) $\eta^E/\eta_0$ vs $\epsilon$ at $\dot{\epsilon} = 3.72s^{-1}$ . Black circles represent the experimental results and solid, dashed and dasheddotdot lines represent the 3-segment FENE bead spring chain (b=4000), Multi-mode FENE dumbbells and the FENE dumbbell (b=100) respectively.	63
5.4	Comparison of prototypical steady state $\tau_{pzz}$ profiles for FENE model predicted using self-consistent simulations, solid line, Lagrangian-based integration, circles, near streamlines shown in (e) and (f) along the surface of the sphere. . . . .	66
5.5	Comparison of the experimentally obtained steady state normalized drag coefficient correction factor with the corresponding values obtained from FENE and FENE-P calculations at $\chi = 0.121$ . . . . .	70
5.6	Comparison of the experimentally obtained steady state normalized drag coefficient correction factor with the corresponding values obtained from FENE and FENE-P calculations at $\chi = 0.243$ . . . . .	71
5.7	Probability density function (PDF) of nondimensionalized end-to-end distance $ \vec{Q} /b$ at the point of maximum stress near the rear stagnation point of sphere predicted by single mode FENE dumbbell model. . .	73
5.8	Probability density function (PDF) of nondimensionalized end-to-end distance $ \vec{Q} /b$ at the point of maximum stress near the rear stagnation point of sphere predicted by multi-mode FENE dumbbell model. . . .	74

5.9	Probability density function (PDF) of nondimensionalized end-to-end distance $ \vec{Q} /b$ at the point of maximum stress near the rear stagnation point of sphere predicted by FENE model. . . . .	75
5.10	The contribution of purely elastic and viscous stresses as well as the pressure to the traction on the surface of the sphere (a,b,c) and total drag on the sphere (d)at $\chi = 0.121$ . . . . .	77
5.11	The contribution of purely elastic and viscous stresses as well as the pressure to the traction on the surface of the sphere (a,b,c) and total drag on the sphere (d)at $\chi = 0.243$ . . . . .	78
5.12	Predicted velocity along the centerline of the tube and surface of sphere at (a) $\chi = 0.121$ and (b) $\chi = 0.243$ ; $b = 4000$ . . . . .	80
5.13	Stress contour plots in the wake of the sedimenting sphere (multi-segment bead spring FENE model with ( $b = 4000$ )). To facilitate the comparison all the results are plotted at the same range and number of contour levels, i.e. 50 levels in 1-10 range. . . . .	81
6.1	Problem formulation: (a) Cross-section of the flow interface created in dip coating, (b) Schematic of the Hele-Shaw flow. . . . .	88
6.2	Cross-section of the flow interface of a soap film. . . . .	89
6.3	Convergence studies, $\tau_{xx}$ , for two different meshes, for low and high $Ca$ flows. . . . .	100

6.4	Details of the computational grids. The design philosophy is to have fine discretization in the capillary transition region and near the tip of the air-liquid interface close to the plane of symmetry. The average width of smallest element in Capillary transition region is within range of 0.0096 to 0.0250 for meshes with 17136 and 16123 elements, respectively. The computational domain is 14 non-dimensional unit long and 0.5 wide. The position of air-liquid interface near the plane of the symmetry is located at $x = 5$ , and the flow properties are independent of $x$ for $x < 3$ and $x > 7$ . The results with a computational domain which is 10 non-dimensional unit long are exactly the same as the computations performed with the longer domain (i.e. 14 non-dimensional unit long). . . . .	101
6.5	Illustration of the normal stress resolution for different $We$ flows, ( $Ca = 0.1, Bo = 160$ ). $s$ is the distance along the interface measured from the tip of the air-liquid interface near the plane of symmetry. . .	102
6.6	Interface shapes as a function of $Bo$ : (a) $Ca = 0.01, We = 0.5$ , (b) $Ca = 0.05, We = 0.5$ . . . . .	106
6.7	Contour plots of the streamlines and effective strain rate. . . . .	107
6.8	Contour plots of the the normal stress ( $\tau_{xx}$ ). The insets show a magnified view of the stress contours in the region of large stresses downstream of the interfacial stagnation point. Also corresponding to each figure line plots of stress and stress gradients along the interface are shown. $A$ represents the location of the stagnation point and $B$ represents the point where the film thickness variation ( $\frac{dh}{dx}$ ) falls below $10^{-5}$ . . . . .	108
6.9	Maximum normal stress ( $\tau_{xx}^{max}$ ) in the stress boundary layer as a function of $We$ : (a) $Ca = 0.01$ , (b) $Ca = 0.05$ . . . . .	109
6.10	Schematic illustrating the interplay between various forces that determine the overall film thickness. . . . .	110

6.11	Percentage deviation from Newtonian film thickness as a function of $We$ : (a) $Ca = 0.01$ , (b) $Ca = 0.05$ . . . . .	111
6.12	Film thickness made dimensionless with the gap width ( $b$ ) as a function of $We$ : (a) $Ca = 0.01$ , (b) $Ca = 0.05$ . . . . .	112
6.13	Film thickness made dimensionless with Bond number ( $Bo$ ) as a function of $We$ : (a) $Ca = 0.01$ , (b) $Ca = 0.05$ . . . . .	113
6.14	Interface shapes as a function of $Bo$ : (a) $Ca = 0.1, We = 0.5$ , (b) $Ca = 0.2, We = 0.5$ . . . . .	115
6.15	Contour plots of the streamlines and the effective strain rate. . . . .	116
6.16	Contour plots of the the normal stress ( $\tau_{xx}$ ). The insets show a magnified view of the stress contours in the region of large stresses downstream of the interfacial stagnation point. Also corresponding to each figure line plots of stress and stress gradients along the interface are shown. $A$ represents the location of the stagnation point and $B$ represents the point where the film thickness variation ( $\frac{dh}{dx}$ ) falls below $10^{-5}$ . . . . .	117
6.17	Maximum normal stress ( $\tau_{xx}^{max}$ ) in the stress boundary layer as a function of $We$ : (a) $Ca = 0.1$ , (b) $Ca = 0.2$ . . . . .	118
6.18	Percentage deviation from Newtonian film thickness as a function of $We$ : (a) $Ca = 0.1$ , (b) $Ca = 0.2$ . . . . .	119
6.19	Film thickness made dimensionless with gap the width ( $b$ ) as a function of $We$ : (a) $Ca = 0.1$ , (b) $Ca = 0.2$ . . . . .	120
6.20	Film thickness made dimensionless with Bond number ( $Bo$ ) as a function of $We$ : (a) $Ca = 0.1$ , (b) $Ca = 0.2$ . . . . .	121
7.1	Eccentric-cylinder coating apparatus: Plexiglas outer cylinder (a) and acrylic end plate (b) for direct visualization of interfacial dynamics. .	124
7.2	Schematic of wet plunging flow. . . . .	125

7.3	The computational domain near the air-liquid interface for meshes with (a) 5074 elements and (b) 19515 elements. . . . .	126
7.4	Convergence studies for two different meshes used in the wet plunging flow simulations. . . . .	126
7.5	The computational domain near the air-liquid interface for the meshes used as the initial guess for the simulation. . . . .	130
7.6	The interface shape near the air-liquid interface in the two steady state solution families (i.e. sharp and smooth curve) observed in the absence of gravity in the flow direction. . . . .	131
7.7	Film thickness as a function of $Ca$ predicted from various initial guesses. f means that the solution was calculated with a positive step in $Ca$ and b means the opposite. . . . .	132
7.8	Film thickness as a function of $Ca$ predicted by mesh with $h_{initial} =$ 0.025. f means that the solution was calculated with a positive step in $Ca$ and b means the opposite. . . . .	133
7.9	The interface shape near the air-liquid interface at $Ca = 1.0$ with and without inclusion of gravitational force in the flow direction. The line plot shows the normal forces along the free surface for three cases whose interface have been shown in parts a to c. . . . .	134
7.10	Schematic view of two positions of the eccentric coater, i.e. (a) horizontal and (b) vertical . . . . .	136
7.11	Schematic view of eccentricities examined at (a) the horizontal and (b) the vertical positions. . . . .	137
7.12	The air-liquid interface shape recorded by a laser sheet at $Ca = 1.0$ . .	138
7.13	The shape of air-liquid interface at different eccentricities at (a) the horizontal and (b) the vertical positions. The interface shapes have been depicted at the azimuthal positions around the cylinder that they are formed and if several interfaces are formed at the similar angles, they have been shown side by side. . . . .	139

7.14	The interface shape near the air-liquid interface at $Ca = 1.0$ . . . . .	141
7.15	The streamlines near the air-liquid interface at $Ca = 1.0$ . . . . .	142
7.16	(a) Film thickness as a function of $We$ , (b) the normal forces along the free surface. . . . .	142
7.17	Line and contour plots of stress gradient, i.e. $\partial\tau_{xx}/\partial x$ . The line plots are along the line shown in the last contour plot, where zero is on the wall. . . . .	143

# Chapter 1

## Introduction

Polymer and polymer matrix composite industries represent a significant portion (i.e., 15%) of the manufacturing segment of Gross Domestic Product (GDP) [Gilmore et al. (2011)]. These industries produce a variety of products ranging from household utilities to flexible packaging, and from state-of-the-art electronic components to high performance composites used in aeronautical and biomedical applications. Economic projections indicate that these industries can grow by 35% over the next ten years by improving existing products, developing new products for future markets, as well as creating more efficient and environmentally friendly processes [BASF (2010)].

A large percentage of the cost of polymeric materials can be attributed to the expensive fabrication step in processing/manufacturing of these materials [Thayer (1990)]. This is primarily because of the large lead-time from design to production that consists of several expensive experimental trials to estimate the right design and operating conditions that can yield a product with the desired microstructure and solid-state properties [Yourdon (1989)]. Hence, if reliable process models that can describe the inter-relationship between macroscopic processing parameters (e.g. temperature, die geometry, flow rate) and microstructure evolution during processing (that ultimately determines the final solid-state product properties) can be developed, they will greatly facilitate rapid and economical process design leading to significant

reduction in the lead-time and cost associated with product development. Recognition of this fact has led to a number of research initiatives among academia and industry focusing on model-based design of polymeric materials processing [Gupta et al. (2004); Baaijens et al. (1994); Schoonen et al. (1998); Kommu et al. (1998); Keunings (1997)]. However, to date such efforts have been primarily focused on development of the continuum-level process simulation software where macroscopic mass, momentum, and energy conservation laws are coupled with a closed form constitutive equation for prediction of polymer stresses. Although, the use of these simulation tools has aided in process design and optimization, their utility is limited as continuum-level simulation models are inadequate in providing quantitative predictions of critical parameters in design and optimization of the process (e.g., pressure drop in complex shaped dies, residual stresses, onset conditions for hydrodynamic, thermal or thermo-elastic instabilities etc.) [Abedijaberi and Khomami (2011); Baaijens et al. (1994); Beraudo et al. (1998)]. More importantly, the approximations involved in derivation of continuum-level constitutive equations often sacrifice details of microstructure development for the sake of reducing the model/computational complexity. Hence, while such models are excellent exploratory tools, they are incapable of predicting the processing-structure-solid state property/performance relationships that are indispensable for the modern product development and design practice. This motivates the use of multiscale models.

Multiscale engineering, i.e., engineering of systems or processes in which the properties of the final product depend on phenomena that occur at different length and time scales, has emerged as a paradigm for engineering practice for the 21st century. Development of faithful, predictive models of such complex phenomena has been a central goal of the scientific pursuit. Phenomenology and empiricism, traditionally employed to quantify cause-effect relationships, lack predictive capabilities and provide little mechanistic insight. In principle, the most detailed description of a system can be obtained from simulations that track the evolution of a large ensemble of its smallest mutually interacting constituents.

However, due to prohibitively large computational overhead, it is impractical to use such simulations to span the length and/or time scales of interest to practical polymer processing applications. We envision a multiscale simulation as the optimal simulator that accurately and self-consistently links the essential information from different scales required to predict system/process-level features. While the emerging role of multiscale modeling and simulations (MMS) has been reshaping R&D in several areas of materials processing and manufacturing [e.g. see excellent reviews by Vvedensky (2004), Nieminen (2002) and Maroudas (2000)] and influencing graduate curricula in science and engineering [Hung et al. (2004)], it has not yet been systematically pursued for process/system-level design/control in the polymer processing industry.

The main objective of this study is to leverage and build upon the aforementioned advances to develop a quantitative understanding of the flow-microstructure coupling mechanisms in viscoelastic polymeric fluids and in turn predict, consistent with experiments, their essential macroscopic flow properties e.g. frictional drag, interface shape, etc. To this end, we have performed extensive continuum and multiscale flow simulations in several industrially relevant bulk and free surface flows. The primary motivation for the selection of the specific flow problems is based on their ability to represent different deformation types, and the ability to experimentally verify the simulation results as well as their scientific and industrial significance. The thesis is organized as follows. The governing equations and computational techniques used in this study are described in chapter 2. In chapters 3 to 7 the results of our extensive continuum and multiscale simulation of polymeric flow in the cross-slot geometry, flow past bluff objects and the dip coating and wet plunging flows are summarized. To put into context our own studies, in each chapter a basic introduction to the problem as well as a brief overview of the state-of-the art in understanding of the flow-microstructure coupling mechanisms is provided. Finally in chapter 8 an overall summary of aforementioned studies as well as future work directions are presented.

# Chapter 2

## Problem Formulation

The equations of motion and continuity for creeping steady flow of an incompressible fluid in the absence of body forces are:

$$-\vec{\nabla}P + \vec{\nabla}.\boldsymbol{\tau} = 0 \quad (2.1)$$

$$\vec{\nabla}.\vec{u} = 0 \quad (2.2)$$

where  $\vec{u}$ ,  $P$ , and  $\boldsymbol{\tau}$  are the velocity vector, isotropic pressure and the deviatoric stress tensor, respectively. The governing equations are non-dimensionalized with respect to the halved channel width,  $H$ , and average inflow velocity,  $V$ , in the case of cross-slot flow, the sphere radius,  $a$ , and the terminal velocity of the sphere,  $U_s$  in the case of sphere sedimentation in a tube, cylinder radius,  $a$ , and the mean velocity in the channel,  $U_{ave}$ , in the case of flow past a cylinder in a channel and the halved channel width,  $b$ , and wall velocity,  $U_w$ , in free surface displacement flows. In this study, the deviatoric stress is split into a polymeric and a solvent contribution:

$$\boldsymbol{\tau} = \boldsymbol{\tau}_s + \boldsymbol{\tau}_p \quad (2.3)$$

where the solvent contribution is assumed to be Newtonian described by Newton law:

$$\boldsymbol{\tau}_s = 2\beta\dot{\boldsymbol{\gamma}} \quad (2.4)$$

In the above equation,  $\beta = \eta_s/\eta_0$  is the ratio of the solvent to the total viscosity and  $\dot{\boldsymbol{\gamma}}$  is the rate of deformation tensor, which is defined as

$$\dot{\boldsymbol{\gamma}} = \frac{1}{2} \left( \vec{\nabla} \vec{u} + (\vec{\nabla} \vec{u})^t \right) \quad (2.5)$$

The system of equations is closed by selecting an appropriate constitutive equation or a micromechanical model for the polymeric stress. The constitutive models that have been developed to date can be broadly classified as the differential or integral type models with a closed form expression for the polymeric stress, and kinetic theory or atomistic based models in which the polymeric stress is predicted from ensemble-averaged microstructural quantities. In this thesis both closed form constitutive equations and kinetic theory based elastic models have been used to describe the polymeric contribution to the deviatoric stress.

## 2.1 Constitutive Equations

In Newtonian fluid mechanics the constitutive law is the same for all fluids. However, there is no universal constitutive model for polymer solutions and melts which can accurately describe the relation between the polymeric stress and deformation caused by fluid motion. Many constitutive models have been developed through the use of kinetic theory. The selection of an appropriate constitutive model for the polymer solution/melt under study is critical as it greatly impacts the fidelity of the final solution to a given problem, since the accuracy of the computed results is highly dependent on the ability of the constitutive model to realistically model the rheology of the fluid under consideration.

### 2.1.1 Oldroyd-B model

The Oldroyd-B model is derived using the kinetic theory of dilute polymeric solutions [Bird et al. (1987)]. The polymer molecules are modeled as Hookean elastic dumbbells in a Newtonian solvent:

$$\boldsymbol{\tau}_p + We \boldsymbol{\tau}_{p(1)} = 2(1 - \beta) \dot{\boldsymbol{\gamma}} \quad (2.6)$$

where  $We$  is the Weissenberg number defined as  $We = \lambda V/H$ ,  $\lambda$  is the polymer molecule relaxation time,  $V$  is the characteristic velocity,  $H$  is the characteristic length and subscript (1) denotes to the upper-convective derivative defined as:

$$\boldsymbol{\tau}_{p(1)} = \frac{\partial \boldsymbol{\tau}_p}{\partial t} + \vec{u} \cdot \vec{\nabla} \boldsymbol{\tau}_p - (\vec{\nabla} \vec{u})^t \cdot \boldsymbol{\tau}_p - \boldsymbol{\tau}_p \cdot (\vec{\nabla} \vec{u}) \quad (2.7)$$

It has been shown that the Oldroyd-B model provides a reasonable description of the rheological behavior of dilute polymeric solutions in shearing flows. However, in elongational flows Oldroyd-B model predict infinite elongational viscosity at finite strain-rates which is obviously aphysical.

### 2.1.2 FENE-P Model

In order to remedy the aforementioned deficiency of linear Hookean dumbbell model in elongational flows, the dumbbell spring models are formulated based on finitely extensible non-linear elastic (FENE) spring force law instead of the Hookean force law. The commonly used FENE spring force was proposed by Warner [Warner (1972)]:

$$\vec{F} = \frac{H \vec{Q}}{1 - Q^2/b} \quad (2.8)$$

In the above equation,  $H$  is the spring constant,  $\vec{Q}$  is the dumbbell connectivity vector,  $Q$  is the length of the connector vector and  $b$  is the maximum extensibility of the spring. Using this force law, a closed form constitutive equation can not be derived; hence, to arrive at a Constitutive equation a closure approximation has to be

involved. The Peterlin approximation is the most commonly used approximation in driving a closed form constitutive equation for dilute polymeric solutions [Bird et al. (1987)]:

$$\vec{F} \cong \frac{\vec{Q}}{1 - \langle Q^2 \rangle / b} \quad (2.9)$$

where  $\langle Q^2 \rangle$  is the ensemble average square of the end-to-end distance. Utilizing this form of the force law, an evolution equation for the conformation tensor,  $\mathbf{A} = \langle \vec{Q}\vec{Q} \rangle$ , and the corresponding polymeric stress can be obtained,

$$\frac{D\mathbf{A}}{Dt} = \boldsymbol{\kappa} \cdot \mathbf{A} + \mathbf{A} \cdot \boldsymbol{\kappa}^t - \frac{1}{We} \frac{\mathbf{A}}{1 - Tr(\mathbf{A})} + \frac{\boldsymbol{\delta}}{We} \quad (2.10)$$

$$\boldsymbol{\tau}_p = \left( \frac{1 - \beta}{We} \right) \left( \frac{b + 3}{b} \right) \left( \frac{\mathbf{A}}{1 - Tr(\mathbf{A})/b} - \boldsymbol{\delta} \right) \quad (2.11)$$

where  $\boldsymbol{\delta}$  is the unit tensor  $Tr(.)$  is the tensor trace operation.

### 2.1.3 FENE-CR Model

It has been shown that the FENE-P model gives rise to a shear rate dependent viscosity [Bird et al. (1987)]. Since many experimental studies make use of Boger fluid which has practically a shear rate independent viscosity while being highly elastic, Chilcott and Ralison [Chilcott and Ralison (1988)] have developed a constitutive model which is still based on the FENE-P description but gives rise to a constant shear viscosity. The polymeric stress contribution to deviatoric stress for this model (CR) is given by

$$\boldsymbol{\tau}_p = \frac{1 - \beta}{We} f(R) (\mathbf{A} - \boldsymbol{\delta}) \quad (2.12)$$

where, similar to FENE-P model,  $\mathbf{A}$  is the configuration tensor obeying the following evolution equation

$$We\mathbf{A}_{(1)} = f(R)(\boldsymbol{\delta} - \mathbf{A}) \quad (2.13)$$

where  $f(R)$  is the connector force. Upon elimination of tensor  $\mathbf{A}$  from the above equations, we obtain the following equation to describe the polymeric stress

$$\boldsymbol{\tau}_p + We(\boldsymbol{\tau}_p/f)_{(1)} = 2(1 - \beta)\dot{\boldsymbol{\gamma}} \quad (2.14)$$

where

$$f = \frac{(b + \frac{1-\beta}{We}Tr(\boldsymbol{\tau}_p))}{(b - 3)} \quad (2.15)$$

#### 2.1.4 Giesekus Model

Up to now we have described constitutive equations that have been mainly developed to describe the rheological properties of dilute polymeric solutions. However, The Giesekus model [Giesekus (1982)] which is also derived from an elastic dumbbell theory, is capable of describing the behavior of concentrated polymer solutions and melts. Because of the large polydispersity of the LDPE melt used in the cross-slot study (see chapter 3), a multi-mode Giesekus model has been used to model the system. In this model the polymeric contribution to the total deviatoric stress associated with each mode  $i$  ( $1 \leq i \leq M$ ) is described by

$$\boldsymbol{\tau}_{p_i} + \lambda_i \boldsymbol{\tau}_{p_i(1)} + \frac{\alpha_i \lambda_i}{\eta_i} (\boldsymbol{\tau}_{p_i} \cdot \boldsymbol{\tau}_{p_i}) = 2\eta_i \dot{\boldsymbol{\gamma}} \quad (2.16)$$

and the total polymeric stress is given by

$$\boldsymbol{\tau}_p = \sum_{i=1}^M \boldsymbol{\tau}_{p_i} \quad (2.17)$$

The parameter  $\alpha_i$  in Eq. (2.16) is the mobility parameter and satisfies  $0 \leq \alpha_i \leq 1$ . In chapter 3, The values of  $\alpha_i$  are set less than 0.5 to ensure monotonic increase of shear stress with shear rate. The origin of this term is associated with the anisotropic

hydrodynamic drag observed in concentrated solutions and melts. For each mode, we introduce the dimensionless relaxation time  $\Lambda_i = \lambda_i/\bar{\lambda}$  and the dimensionless polymeric viscosity  $\beta_i = \eta_i/\eta_0$  so that Eq. (2.16) can be rewritten in dimensionless form as

$$\boldsymbol{\tau}_{\mathbf{p}_i} + We\Lambda_i\boldsymbol{\tau}_{\mathbf{p}_{i(1)}} + \frac{\alpha_i We\Lambda_i}{\beta_i}(\boldsymbol{\tau}_{\mathbf{p}_i} \cdot \boldsymbol{\tau}_{\mathbf{p}_i}) = 2\beta_i\dot{\boldsymbol{\gamma}}, \quad (2.18)$$

## 2.2 Kinetic Theory Based Elastic Models

In kinetic theory based description of the polymer molecules, the polymer dynamics at the mesoscopic level is described by a FENE dumbbell or a bead-spring chain and  $\boldsymbol{\tau}_p$  is evaluated using the Kramers' expression [Bird et al. (1987)]:

$$\boldsymbol{\tau}_p = \left(\frac{1-\beta}{We}\right) \left(\frac{b_s+5}{b_s}\right) \sum_{i=1}^N \left( \left\langle \vec{F}_i \vec{Q}_i \right\rangle - \left\langle \vec{F}_i \vec{Q}_i \right\rangle_{eqbm} \right) \quad (2.19)$$

where,  $N$  is the number of segments in the bead-spring chain,  $b_s = NHQ_0^2/k_B T$ ,  $Q_0$  is the maximum extensibility of each segment,  $H$  is the spring constant,  $\vec{Q}_i$  is the segmental connectivity vector which is non-dimensionalized with respect to its equilibrium length  $\sqrt{k_b T/H}$ ,  $\left\langle \vec{F}_i \vec{Q}_i \right\rangle_{eqbm} = \boldsymbol{\delta}$  and  $\langle . \rangle$  is the average (or the expectation) over the entire ensemble, and  $\vec{F}_i$  is the nonlinear FENE force law for the  $i^{th}$  segment given by:

$$\vec{F}_i = \frac{\vec{Q}_i}{1 - (NQ_i^2/b_s)} \quad (2.20)$$

Where  $Q_i$  is the length of  $i^{th}$  segment.

The temporal evolution of the segmental connectivity vector  $\vec{Q}_i$  of  $i^{th}$  segment of the FENE bead-spring model under flow is determined using the BCF approach [Hulsen et al. (1997); Somasi and Khomami (2000)] since it is ideally suitable for implementation in the finite element context. The BCF evolution equation for the segmental connectivity is given as:

$$d\vec{Q}_i(x, t) = \left[ -\vec{u}(x, t) \cdot \vec{\nabla} \vec{Q}_i(x, t) + \boldsymbol{\kappa}(x, t) \cdot \vec{Q}_i(x, t) - \frac{\vec{F}_i^E}{4W_e} \right] dt + \sqrt{\frac{1}{2W_e}} \left[ d\vec{W}_{i+1}(t) - d\vec{W}_i(t) \right] \quad (2.21)$$

where

$$\vec{F}_i^E = \begin{cases} -2\vec{F}_i + \vec{F}_{i+1}; & i = 1, \\ \vec{F}_{i-1} - 2\vec{F}_i + \vec{F}_{i+1}; & 1 < i < N, \\ \vec{F}_{i-1} - 2\vec{F}_i; & i = N \end{cases} \quad (2.22)$$

and  $\boldsymbol{\kappa}$  is the transpose of the velocity gradient (i.e.  $\boldsymbol{\kappa} = (\vec{\nabla} \vec{u})^t$ ), and  $d\vec{W}_i(t)$  is the Wiener process which accounts for the Brownian force experienced by the  $i^{th}$  beads. The Wiener process is mathematically represented by a Gaussian random vector with zero mean and variance  $dt$ , the time step in the problem.

## 2.3 Computational Technique

We have used the DEVSS-G (Discrete Elastic Viscous Split Stress - Gradient of velocity) finite element method to solve the set of governing equations [Khomami et al. (1994); Koppol et al. (2007); Somasi et al. (2002); Talwar et al. (1994); Talwar and Khomami (1992)]. As has been shown in previous studies [Szady et al. (1995)], this is an efficient and robust technique to solve steady and time-dependent viscoelastic flow problems. The weak forms of the momentum and mass conservation equations using the Galerkin procedure is given below:

$$\left[ (\vec{\nabla} \vec{v}) : \left( \vec{\nabla} \vec{u} + (\vec{\nabla} \vec{u})^t - P\boldsymbol{\delta} + \boldsymbol{\tau}_p - (1 - \beta)(\boldsymbol{G} + \boldsymbol{G}^t) \right) \right] = [\vec{v} : \vec{\sigma}]_{\Gamma} \quad (2.23)$$

$$\left[ q; \vec{\nabla} \cdot \vec{u} \right] = 0 \quad (2.24)$$

$$\left[ g : (\mathbf{G} - \vec{\nabla} \vec{u}) \right] = 0 \quad (2.25)$$

In the above equations  $\mathbf{G}$  is the discrete interpolant for the velocity gradient  $(\vec{\nabla} \vec{u})$ .  $[a : b]$  (or  $[a; b]$ ) and  $[a : b]_\Gamma$  are the standard inner products of  $(a, b)$  in the domain  $\Omega$  and on the boundary  $\Gamma$ , respectively;  $\vec{\sigma}$  is the traction vector on the boundary. Standard polynomials based on the Legendre functions are used as the weighting functions [Szabo and Babuska (1987)]. Specifically, we have used continuous biquadratic polynomials for the velocities and continuous bilinear polynomial for pressure and the velocity gradient [Szabo and Babuska (1987)].

The closed form constitutive equation, FENE-P for example, and the segmental connectivity vector equations are discretized using the SUPG technique [Brooks and Hughes (1982)]:

$$\left[ \left( \boldsymbol{\tau}_p + We (\boldsymbol{\tau}_p z)_{(1)} + (1 - \beta) (\mathbf{I} z)_{(1)} \right) : \mathbf{Y} \right] = 0 \quad (2.26)$$

$$\left[ \begin{array}{l} d\vec{Q}_i - \left( -\vec{u} \cdot \vec{\nabla} \vec{Q}_i + \boldsymbol{\kappa} \cdot \vec{Q}_i + \frac{1}{4We} \vec{F}_i^E \right) dt \\ - \sqrt{\frac{1}{2We}} \left( d\vec{W}_{i+1}(t) - d\vec{W}_i(t) \right) \end{array} \right] : \mathbf{Y} = 0 \quad (2.27)$$

where  $\mathbf{Y}$  is selected from the bilinear continuous polynomial space (p=1).

For the FENE dumbbell or the bead-spring chain,  $\boldsymbol{\tau}_p$  is evaluated using the Kramers' expression via a Galerkin projection method:

$$\left[ \left( \boldsymbol{\tau}_p - \frac{(1 - \beta)}{We^*} \sum_{i=1}^N \left( \langle \vec{F}_i \vec{Q}_i \rangle - \boldsymbol{\delta} \right) \right) : \mathbf{m} \right] = 0 \quad (2.28)$$

where  $\mathbf{m}$  is chosen from the bilinear continuous polynomial space (p=1).

# Chapter 3

## Flow of branched polymer melts in a lubricated cross-slot channel: a combined computational and experimental study

### 3.1 Introduction

The non-Newtonian flow characteristics of polymer melts strongly impact the vast majority of processing operations used to manufacture polymeric products such as mixing, extrusion, fiber spinning, film blowing or injection molding [Dealy and Wissbrun (1990)]. Quantitative prediction of velocity and stress distributions in complex flows of polymers is a challenging goal which offers the promise of more effective processing operations and designs. Advances in computational algorithms have largely resolved the long-standing Weissenberg or Deborah number problem that had limited numerical simulations to weakly elastic conditions for many years [Keunings (2001)]. The steady growth of computational power has made it possible to employ multiple-mode differential or integral constitutive equations that accurately

reflect the distribution of relaxation times of real polymers and to perform time-dependent calculations in complex geometries. To date, stress distributions from flow birefringence measurements together with finite element (FE) computational studies in stagnation flows have shown to provide effective critical tests of constitutive model performances in complex flows [Li et al. (1998, 2000); Burghardt et al. (1999a); Feigl and Ottinger (1996)]. In this context, it has become highly relevant to derive constitutive models which can not only predict the linear and non-linear flow behavior of polymeric fluids in shear or extension but also be proven effective in describing non-homogeneous flows involving mixed shear and extensional deformations. In recent years, coordinated experimental/computational studies of polymeric systems have typically employed multiple-mode versions of various differential (Giesekus, Phan-Thien Tanner, Bird-DeAguiar) or integral (Wagner, Papanastasiou-Macosko-Scriven) constitutive equations [Bird et al. (1987)]. Such models have had reasonable but not universal success in predicting the behavior of polymer melts and solutions. Specifically, it has been established that the multimode Giesekus model performs exceptionally well in predicting the flow kinematics and stress field of moderately concentrated polymeric solutions under steady state conditions up to moderate Weissenberg numbers [Li et al. (1998, 2000); Burghardt et al. (1999a)]. In cross-slot geometries for instance, the Giesekus model has been used by Schoonen [Schoonen et al. (1998)] to perform a three-dimensional (3D) analysis of the stagnation flow of a polyisobutylene solution. However, the presence of end effects close to the stagnation point led to experimental birefringence optical data up to three times higher than the numerical simulation predictions. In a flow channel similar to Schoonen et al., Peters [Peters et al. (1999)] studied the performances of the Giesekus model in predicting the complex flow of a polyethylene melt using birefringence isochromatic fringe pattern measurements. Large deviations between the 2D viscoelastic simulations and the experimental results were located downstream of the stagnation point and mainly attributed to end effects and beam deflections. In the same cross-slot device, Verbeeten [Verbeeten et al. (2002)] further compared the extended Pom-Pom and

Giesekus model predictions with experimental results along the channel symmetry line and observed an over predicted maximum stress in the vicinity of the stagnation point due to possible end effects in the stagnation region of the flow cell. To date, end effects in flow birefringence experiments have largely prevented from a rigorous evaluation of the Giesekus model predictions in complex mixed flows of polymeric systems. In this study, we aim at assessing the performances of the multi-mode Giesekus model in describing the flow behavior of a LDPE melt flowing in an actual 2D flow channel recently developed by Soulages [Soulages (2007)].

## 3.2 Flow birefringence of polymer melts

Stress distribution measurements using flow birefringence in mixed kinematics flows of polymer melts provide a stringent test of the predictive capabilities of constitutive equations. Flow-induced birefringence is one of the most prevalent non-invasive techniques which allow a complete mapping of stress fields in polymeric systems under flow. In flow birefringence experiments, the direct relationship between the optical and molecular anisotropy expressed by the stress-optical rule is exploited to measure the flow induced polymeric stresses [Fuller (1995)]. Most methods for measuring flow birefringence involve passing a light beam through a flowing birefringent medium in order to capture the resulting optical anisotropy averaged along the optical path. Thus, the flow should be 2D in order to guarantee that the optical properties do not vary along the light path. In reality however, the confining walls of the experimental geometry inevitably lead to end effects. That is why many researchers have resorted to utilizing large aspect ratio flow channels to minimize the influence of the parasitic shear gradients near the sidewalls. Indeed, they commonly refer to the study of Wales generally considered as an experimental evidence that end effects become negligible in channels having an aspect ratio greater than 10 [Wales (1976)]. Contrary to this generally accepted view, working with a large aspect ratio is not sufficient to guarantee 2D flows. Recently, systematic

studies have conclusively shown that the stress gradients along the beam path near the confining walls cause uncertainties in the effective extinction angle measurement which can possibly be eliminated working with large aspect ratios [McHugh et al. (1987); Ottinger (1999)]. To circumvent the difficulties associated with creating 2D flows, a few researchers have used axisymmetric geometries and compared the integrated optical measurements with numerical simulation predictions to assess the performances of various constitutive models [Li et al. (1998, 2000); Burghardt et al. (1999a)]. Although the computational demands in such studies are equivalent to those encountered for simulating 2D flows, accurate experimental measurements are very challenging due to parasitic wall effects or laser beam spread. Alternatively, one can perform 3D simulations and compare the integrated stresses along the light path with experimental data. However, the computational burden associated with performing 3D simulations in complex flow geometries with realistic multimode constitutive equations is orders of magnitude higher than 2D simulations and requires significant super computing resources. In addition, end effects in 3D flows prevent from a reliable measurement of the extinction angle as the small retardance approximation is not valid for polymer melts exhibiting multiple orders of retardation. Those difficulties have motivated a recent work by Soulages [Soulages et al. (2008)] based on a novel optical cross-slot channel rheometer whose front and back viewing windows are lubricated so that a complex two-dimensional isothermal flow is created. Lubricating sidewalls not only eliminates the stress gradients near the walls and subsequently the end effects but also makes it possible to use small aspect ratios. This latter property presents the advantage of working with a perfectly collimated beam over the entire channel depth and offers a better control of the temperature in the flow cell.

### 3.3 Problem formulation

The test fluid in this study is described using multimode Giesekus model and the numerical technique used in this study is the higher-order-discrete-elastic-viscous-stress (hp-DEVSS) finite element method, see chapter 2. Both slip and symmetry boundary conditions have been used. In particular, we introduce a slip velocity  $u_{\text{slip}}$  so that the velocities on the sidewalls verify  $\vec{u} \cdot \vec{t} = u_{\text{slip}}$  and  $\vec{u} \cdot \vec{n} = 0$  where  $\vec{t}$  and  $\vec{n}$  represent unit vectors respectively tangent and normal to the boundary walls in the laboratory frame defined in figure 3.1. In addition, the in- and outflow channel centerline velocities together with the  $\tau_{xy}$  component of the stress tensor are set to zero due to symmetry. At the channel inlet, the velocity profile ( $u_y = u_y(x)$  and  $u_x = 0$ ) and the necessary components of the stress tensor are specified by assuming a fully developed flow. At the exit, a fully developed velocity profile ( $u_x = u_x(y)$  and  $u_y = 0$ ) is also specified. For most nonlinear constitutive equations such as the Giesekus model, analytical solutions are not available even under fully developed conditions. Thus, the fully developed inlet and outlet boundary conditions were generated numerically in a mesh with the same number of nodes and node locations as the mesh used in the inflow and outflow channels of the flow computations. Due to the inherent symmetry of the flow channel, the computational domain is restricted to one quarter of the flow domain as shown in figure 3.1. It is divided into a number of quadrilateral elements to obtain an approximation to the exact solution. In order to check the accuracy of the calculations, we have selected three structured meshes based on the same topology and illustrated in figure 3.2. The mesh with the lowest discretization in figure 3.2a was chosen according to the results from meshes used to generate the fully developed inlet and outlet boundary conditions. In all meshes, the nodes were pushed towards the experimental geometry walls in order to capture the sharp velocity and stress gradients close to these boundary layers. The other node positions were calculated in order to guarantee a satisfactory number of nodes near the stagnation point while avoiding drastic size differences between nearby elements.

The finest meshes in figures 3.2b–c were designed to provide refinements in the regions where oscillations in stresses were observed. The full system of discretized equations is solved using a frontal solver Newton-Raphson iteration method. Details of this method can be found in [Talwar and Khomami (1992)]. In the Newton-Raphson method, convergence is ensured if the initial guess is sufficiently close to the exact solution. To ensure a good initial guess, we have used the Weissenberg number,  $We$  as the continuation parameter in our calculation. To do so,  $We$  was first set to zero and the linear Newtonian flow problem was solved. Next, the solution of this calculation was used as a guess for the next  $We$ . Increments of 0.01 to 0.25 were used to capture the solution up to  $We$  equals 29. The convergence criterion used in the Newton-Raphson scheme is  $\sum_{i=1}^e \Delta a_i^2 \leq 10^{-6}$  where  $\Delta a_i^2 = (a_i^{k+1} - a_i^k)^2$  and  $a_i^k$  represents the value of the unknown expansion coefficients at the  $k^{\text{th}}$  iteration.

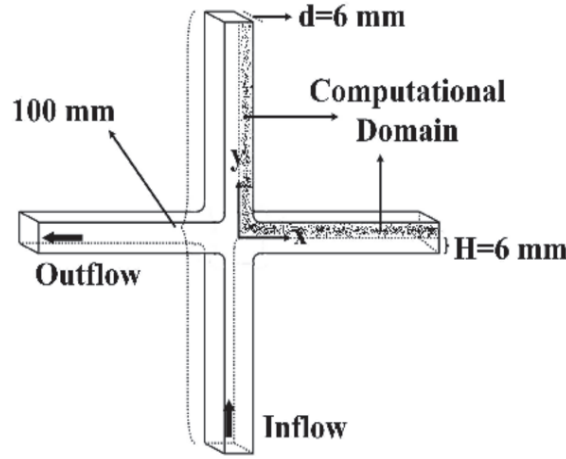


**Figure 3.1:** Schematic view of the computational domain of the cross-slot flow channel.

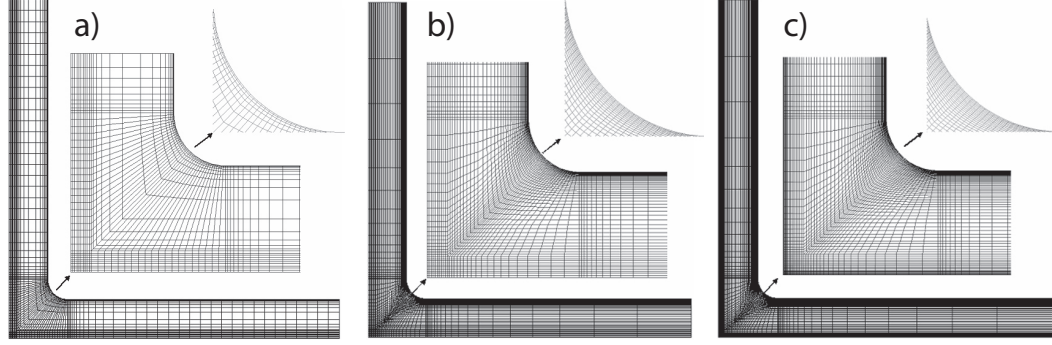


**Figure 3.2:** Finite element meshes with a) 3492 b) 4500, and c) 6400 elements. (cross-slot flow channel).

## 3.4 Experiment

### 3.4.1 Experimental Setup

A complete description of the flow geometry and lubrication technique can be found in [Soulages et al. (2008)]. The experimental geometry is shown in figure 3.3. The channel consists of four transparent arms of length 50 mm, which are made visible using flush-mounted glass viewing windows. The width and height of the flow cell equal 12 and 6 mm so that its aspect ratio is 0.5. In the vicinity of the stagnation point, rounded corners with a radius of 3 mm ensure a smooth transition between the channel in and outlets. At each arm entrance, a set of two opposite oil slits delivers the lubricant (silicone oil) at a constant volumetric flow rate. The lubricant flow rate can be optimized at any time during an experiment using birefringence and particle tracking velocimetry measurements and the oil pressure is monitored so that planar conditions can effectively be reached. The lubricant is dragged along the glass windows by the incoming polymer streams, resulting in an oil film whose thickness is of the order of several microns. The two opposed polymer melts impinge in the middle of the flow cell and exit the channel through its two horizontal arms. The entire channel is fixed to a computer-controlled XY-translation stage so that flow birefringence can be measured in the channel transparent section.

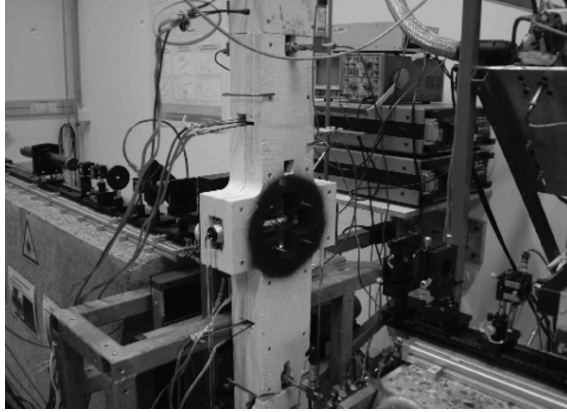


**Figure 3.3:** Experimental setup: the cross-slot flow channel is attached to an XYtranslation stage whereas the flow-induced birefringence optical elements are mounted on a fixed stone support plate.

In our study, the stress field is obtained from pointwise flow-induced birefringence measurements [Fuller (1995)]. The optical rail is visible in figure 3.3 and is identical to [Galante (1991)]. This technique is based on a polarization modulation method which is thoroughly described in [Soulages (2007)]. It allows a direct measurement of the retardation  $\delta$  and extinction angle  $\chi$  of the birefringent polymer melt within the laser beam diameter of  $120 \mu\text{m}$ . The *dc* component ( $I_{\text{dc}}$ ) of the modulated light intensity collected at the detector is measured by means of a low pass filter whilst the first and second Fourier components ( $I_{\omega}$  and  $I_{2\omega}$ ) are sampled using two lock-in amplifiers. After the experimental determination of the calibration constants ( $J_1$  and  $J_2$ ), the ratios of the Fourier components to the *dc* intensity make it possible to define optical signals which directly relate the optical properties to the sample retardation  $\delta$  and extinction angle  $\chi$  and read

$$\begin{aligned} R_{\omega} &= -\frac{I_{\omega}}{2J_1 I_{\text{dc}}} = \sin(\delta) \cos(2\chi), \\ R_{2\omega} &= \frac{I_{2\omega}}{2J_2 I_{\text{dc}}} = \sin^2\left(\frac{\delta}{2}\right) \sin(4\chi). \end{aligned} \tag{3.1}$$

Eq. (3.1) only involves trigonometric functions of  $\chi$  and  $\delta$ . In practice, polymer melts show very large levels of birefringence with retardations  $\delta$  often exceeding  $2\pi$ . Except in the fully developed region, we could not easily spatially determine the number of multiples of  $2\pi$  for the retardation in the entire flow cell. That is why we have restricted our analysis to the optical data of Eq. (3.1) in which  $\chi$  and  $\delta$  could be numerically computed from the stress tensor simulation predictions using the stress-optical rule and according to

$$\chi = \frac{1}{2} \tan^{-1} \left( \frac{2\tau_{xy}}{\tau_{xx} - \tau_{yy}} \right), \quad \delta = \frac{4\pi d C}{\lambda} \frac{\tau_{xy}}{\sin(2\chi)}, \quad (3.2)$$

where the  $x$ -axis is associated to the flow direction in figure 3.1,  $\lambda$  is the wavelength of the light beam,  $d$  is the channel thickness and  $C$  is the stress-optical coefficient. This coefficient was set to  $C = 1.7 \times 10^{-9} \text{ Pa}^{-1}$  as determined in [Soulages (2007)]. For polymer melts, the validity of the stress-optical rule has extensively been shown in shear flows [Janeschitz-Kriegl (1983); Wales (1976); Rajagopalan et al. (1992)]. In uniaxial elongational flows, it has recently been proven for applied stresses not exceeding 1 MPa [Venerus et al. (1999); Luap et al. (2005, 2006)]. Beyond this value, the failure of the rule is often associated to the chain finite extensibility [Kroger (2004)] but the critical stress levels are generally not accessible in practice [Kroger et al. (1997)].

In this work, the velocity field in the fully developed inflow region of the flow cell is obtained from particle tracking velocimetry measurements to allow us to determine the slip velocity at the channel lateral walls in Section 3.5.1. The experimental technique is extensively described in [Soulages (2007)]. Tracer particles mixed with the polymer melt are illuminated from the front so that the marker displacements can be tracked as a function of time and imaged onto a CCD camera. Anywhere else in this work, the velocity field is directly derived from the finite element calculations and used to compute the predicted optical results.

### 3.4.2 Fluids and its Rheological Characterization

Our test fluid is a commercial grade of low density polyethylene (LDPE 1810H from Basell). In this study we have used 11-mode Giesekus model as it provides a good fit to the rheological measurements. The parameters of this model (i.e.  $\lambda_i, \eta_i, \alpha_i$ ) associated with each mode can be determined from the linear and nonlinear rheological characterization of test fluid. Specifically, the relaxation spectrum can be determined from linear viscoelastic measurements via regression analysis and the nonlinear parameters (i.e.  $\alpha_i$ ) can be determined from shear and elongation characterizations. The linear viscoelastic data with the model fit of the parameters is shown in figure 3.4. The solid lines in figure 3.4 represent the 11-mode fit to the linear viscoelastic properties; the linear viscoelastic parameters are given in Table 3.1. After obtaining the relaxation time and viscosity spectrum by fitting the linear viscoelastic properties, the nonlinear model parameters,  $\alpha$ , are determined as follows; first considering the same value of  $\alpha$  for all modes, the optimum  $\alpha$  value is obtained by fitting the model predictions to the steady shear data, namely the shear viscosity and the first normal stress difference N1 (see figure 3.5). This is done by minimizing the weighted least squares of the deviations of the model predictions from the N1 and shear viscosity experimental data. Next, the  $\alpha$  for each mode is individually fine-tuned to fit the uniaxial extensional viscosity data, figure 3.6. The nonlinear parameters calculated in this way are also given in Table 3.1. Overall the Giesekus model is capable of providing a good description of shear (i.e., viscosity and first and second normal (figure 3.5) stresses) and elongation rheology (figure 3.6) for a branched entangled polymer, LDPE.

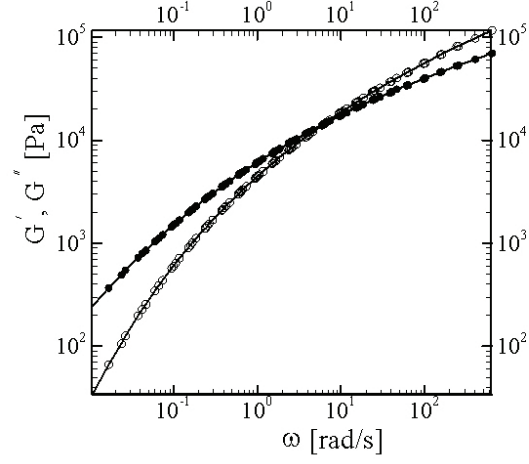


**Figure 3.4:** Storage (open symbols) and loss (full symbols) module at  $170^{\circ}\text{C}$  together with the calculated spectrum predictions (full lines).

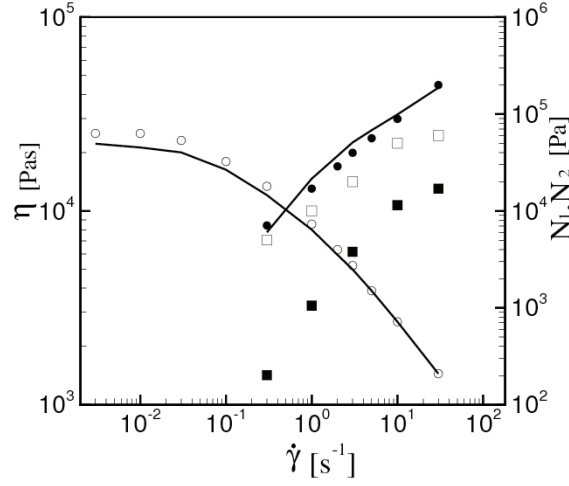


**Figure 3.5:** Steady shear viscosity (open circle symbols), first (full circle symbols) and second (full square symbols) normal stress difference at  $170^{\circ}\text{C}$  together with the Giesekus model predictions (open square symbols for the second normal stress difference and full lines for the shear viscosity and the first normal stress difference).

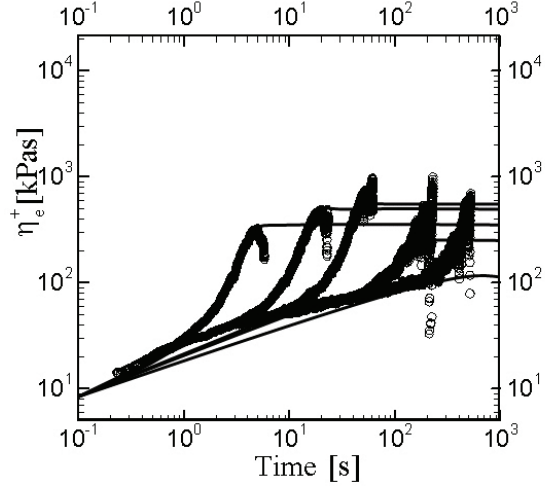


**Figure 3.6:** Uniaxial extensional viscosity (open symbols) measured at  $170^\circ\text{C}$  together with the Giesekus model predictions (full lines). Hencky strain rate range: 0.88, 0.25, 0.1, 0.028, and  $0.00971 \text{ [s}^{-1}\text{]}$ .

**Table 3.1:** Giesekus parameters:  $\eta_i$ ,  $\lambda_i$ , obtained from linear viscoelasticity data and  $\alpha_i$  from steady shear and transient uniaxial extensional data.

Mode ( $i$ )	1	2	3	4	5	6
$\eta_i$ (Pa.s)	60.900	62.213	159.691	496.439	711.020	1333.339
$\lambda_i$ (s)	0.0005	0.0016	0.0051	0.0166	0.0534	0.1718
$\alpha_i$	0.3	0.3	0.3	0.3	0.3	0.3
Mode ( $i$ )	7	8	9	10	11	Mean
$\eta_i$ (Pa.s)	2462.8	3471.9	5545.3	3310.3	5111.1	
$\lambda_i$ (s)	0.5522	1.7750	5.7080	18.3500	59.0000	16.5
$\alpha_i$	0.3	0.3	0.25	0.2	0.05	—

## 3.5 Results

In this section, we recall that the Weissenberg number is defined as  $We = \bar{\lambda}V/H$ , where  $V$  represents the mean inflow velocity and  $H$  denotes the halved channel width ( $H = 6$  mm).

### 3.5.1 Determination of the Slip Velocity

The computational results with no-slip boundary conditions at the channel lateral walls did not compare favorably with the experimental results even in the fully developed region as shown in figure 3.7a. Upon further examination of the experimental cross-slot flow, it was determined that some of the lubricant used to coat the transparent windows of the flow cell had migrated towards the brass solid walls giving rise to a fully developed encapsulated polymer flow. Hence, all solid surfaces in the experimental setup are lubricated with a very thin lubricant layer in the order of several microns. Therefore, we had to incorporate this effect into our computations in order to better capture the experimental flow conditions. The simplest way to do so was to introduce a slip velocity  $u_{\text{slip}}$  at the channel sidewalls.

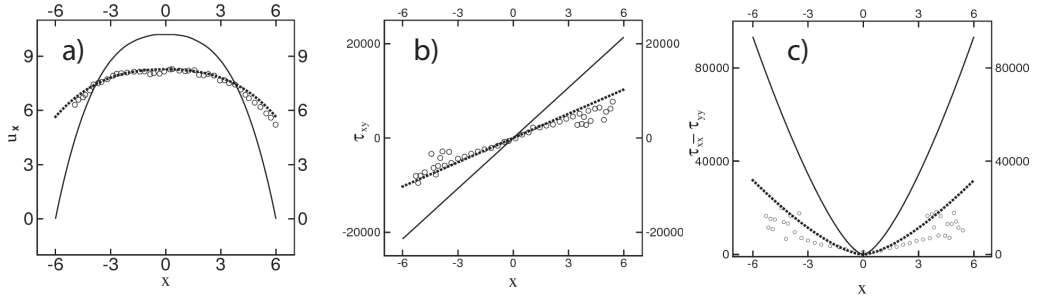


**Figure 3.7:** a) Velocity profile, b) shear stress profile, and c) normal stress profile at  $We = 21$  in the channel fully developed inflow region: experimental data (open circles), computational results using no-slip (solid line) and slip (dotted line) boundary conditions with a slip velocity of  $u_{\text{slip}} = 5.6$  mm/s.

In the fully developed region of the flow cell, the polymer kinematics were derived from particle tracking velocimetry measurements. However, it was especially difficult to obtain reliable results close to the channel solid boundaries because of parasitic light reflections at the brass sidewalls perturbing the marker recognition. Hence, the slip velocity could not experimentally be obtained at the channel lateral walls. Therefore, we have numerically simulated results for different slip velocities in order to determine its optimum value for each Weissenberg number. The best slip velocity was obtained via a regression analysis by minimizing the overall differences between the computed and measured velocity (figure 3.7a) and stress fields (figures 3.7b–c) in the channel fully developed region. Indicated by solid lines in figures 3.7a–c, the numerical results corresponding to no-slip boundary conditions at  $We = 21$  are also given for comparison. Following this procedure, the best agreement was found for a slip velocity of 5.6 and 6.1 mm/s at  $We = 21$  and 29, respectively. It should be noted that the assumption of a uniform slip velocity in the fully developed region is quite reasonable as the thickness of the lubricant layer is expected to remain nearly constant. However, one would expect variations in the lubricant thickness around the rounded corners next to the stagnation region. Since the lubricant reflections prevent us from measuring a reliable slip velocity at the channel lateral walls, we have used a unique slip velocity all along the sidewalls. As a regression technique has been used to obtain the optimum slip velocity  $u_{\text{slip}}$ , it is highly relevant to assess the influence of small changes in the slip velocity on the predicted stress and velocity profiles. Figures 3.8a–c show the different velocity and stress profiles for variations of the slip velocity of the order of  $\pm 0.001$ , 0.005, 0.01 and 0.5 mm/s at a Weissenberg number of  $We = 21$ . It can clearly be seen in these figures that differences in the velocity and stress profiles in the fully developed region of the flow cell become visible for variations in the slip velocity of the order of 0.005 mm/s. However, variations of the order of 0.001 mm/s do not give rise to observable changes in the kinematics and stress profiles.

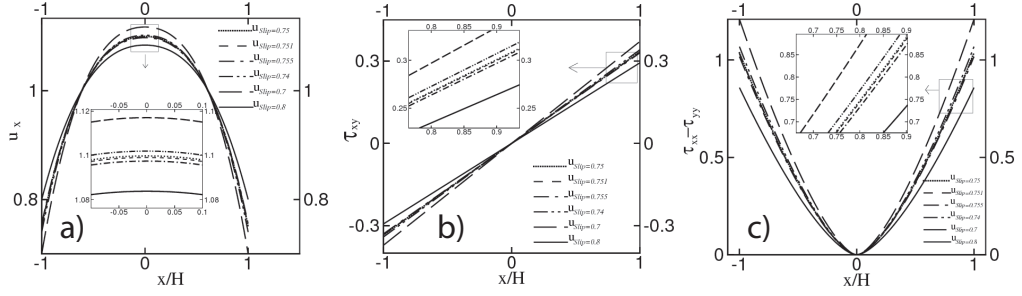


**Figure 3.8:** a) Velocity profile, b) shear stress profile, and c) normal stress profile in the fully developed region at  $We = 21$  for different imposed slip velocities  $u_{slip}$  at the channel lateral walls.

### 3.5.2 Results at Moderate Weissenberg Numbers ( $We = 21$ )

In order to evaluate the Giesekus model capabilities in predicting the complex flow of our test fluid, we have focused our data analysis on various locations in the inflow ( $y/H = 0.2, 1.5$ , and  $5$ ) and outflow ( $x/H = 0.2, 1.5$ , and  $5$ ) channel as represented by the cross-slot schematic view in figures 3.9 and 3.10. These locations have been chosen to assess the ability of the Giesekus model to capture the flow behavior in simple shear, mixed shear and extensional kinematics and planar extension. Figure 3.9a shows the experimental and computational optical results in the inflow channel arm. Because of the lubricant light reflections leading to unreliable experimental optical results at the channel edges, the data presented in figures 3.9 and 3.10 are restricted to the range  $-0.6 \leq x/H \leq 0.6$  and  $-0.6 \leq y/H \leq 0.6$ .

At  $y/H = 5$  (open triangle symbols), the model provides a good prediction of both the  $R_\omega$  and  $R_{2\omega}$  optical signals of Eq. (3.1). This result was quite expected as the slip velocity has been chosen by matching the stress and velocity profiles in this region of the flow cell. The slight differences observed between the predicted and experimental values are due to the fact that the slip velocity was obtained by minimizing the overall deviations between the measured and computed velocity and stress fields. At  $y/H = 1.5$  (filled square symbols), a good agreement is also found between the optical

and model data. Thus, in the region of mixed kinematics where the polymer melt extensional thickening is not very pronounced, the Giesekus model is successful in predicting the flow behavior. However, in the region of planar extensional flow at  $y/H = 0.2$  (open circle symbols), the model predictions although reasonable are not quantitative. Specifically, the  $R_{2\omega}$  optical signal is under predicted by the model. This discrepancy becomes more pronounced as one approaches the stagnation point. However, it should be noted that the quality of the experimental data in this region of the channel is not very good. In particular, oil film reflections together with multiple orders of retardation occurring within the laser beam make the experimental results questionable close to the stagnation point where the lubricant tends to accumulate and large stress variations take place within the beam width. In the outflow channel in figure 3.9b, although the simulations are successful in qualitatively predicting the flow behavior at  $x/H = 0.2$ , the predictions along the channel centerline are not very accurate. Specifically, they show the same number of peaks for  $R_\omega$  as experimentally observed but their location and magnitude are not exactly reproduced. The  $R_{2\omega}$  optical data predictions in the outflow channel are in qualitative agreement with the experimental data.

### 3.5.3 Results at Large Weissenberg Numbers ( $We = 29$ )

Figures 3.10a–b present the experimentally measured and computed optical signal distribution at a Weissenberg number of  $We = 29$  in the inflow and outflow channels, respectively. The quality of the predictions in the inflow channel is very similar to the one obtained at  $We = 21$ , except for  $y/H = 0.2$ . At this location, the model predictions are not as accurate as their  $We = 21$  counterpart. If the experimental  $R_{2\omega}$  optical signal is qualitatively well captured by the model, large discrepancies are observed for the  $R_\omega$  optical data. The Giesekus model deficiency in predicting the experimental data at high  $We$  numbers becomes even more evident in the outflow channel. In figure 3.10b, the experimental data predictions are poor at  $x/H = 0.2$ . In

particular, the number of peaks in the measured optical signals is not well predicted by the Giesekus model. This discrepancy is not observed at  $x/H = 1.5$  where the number of peaks is the same as experimentally observed. The  $R_\omega$  predictions at  $x/H = 5$  are as good as in figure 3.9b at  $We = 21$ . It should be mentioned here that the effect of multiple retardation orders at length scale of the beam diameter becomes even more visible at large Weissenberg numbers in the presence of high stress boundary layers. That is why the averaged optical properties measured using the existing experimental setup are again questionable. Therefore, the disagreement observed between the measured and computed quantities at  $We = 29$  cannot be inferred to the constitutive model only and might also be due to experimental uncertainties.

Current experimental limitations in terms of lubricant reflections and multiple orders of retardation within the laser beam diameter do not allow to fully appreciating the Giesekus model predictions in the region of planar extension close to the stagnation point. Even though the model seems to accurately capture the flow behavior in the inflow region of mixed kinematics, the Giesekus model predictions in the outflow region of planar extension cannot be distinctively attributed to the constitutive modeling or to experimental artifacts, especially at large Weissenberg numbers where the experimental constraints are enhanced. We are currently working on possible improvements of the actual experimental setup in order to try to minimize the experimental artifacts. These would involve a new oil delivery design together with a reduction of the laser beam dimensions.

## 3.6 Conclusion

Numerical simulations of a well-characterized, branched, low-density polyethylene melt in a lubricated cross-slot channel geometry have been performed for a range of Weissenberg numbers. Due to the fact that all the side walls of the cross-slot rheometer are lubricated, comparison of the experimental flow birefringence measurements had to be made with self-consistent 2D flow simulation with an

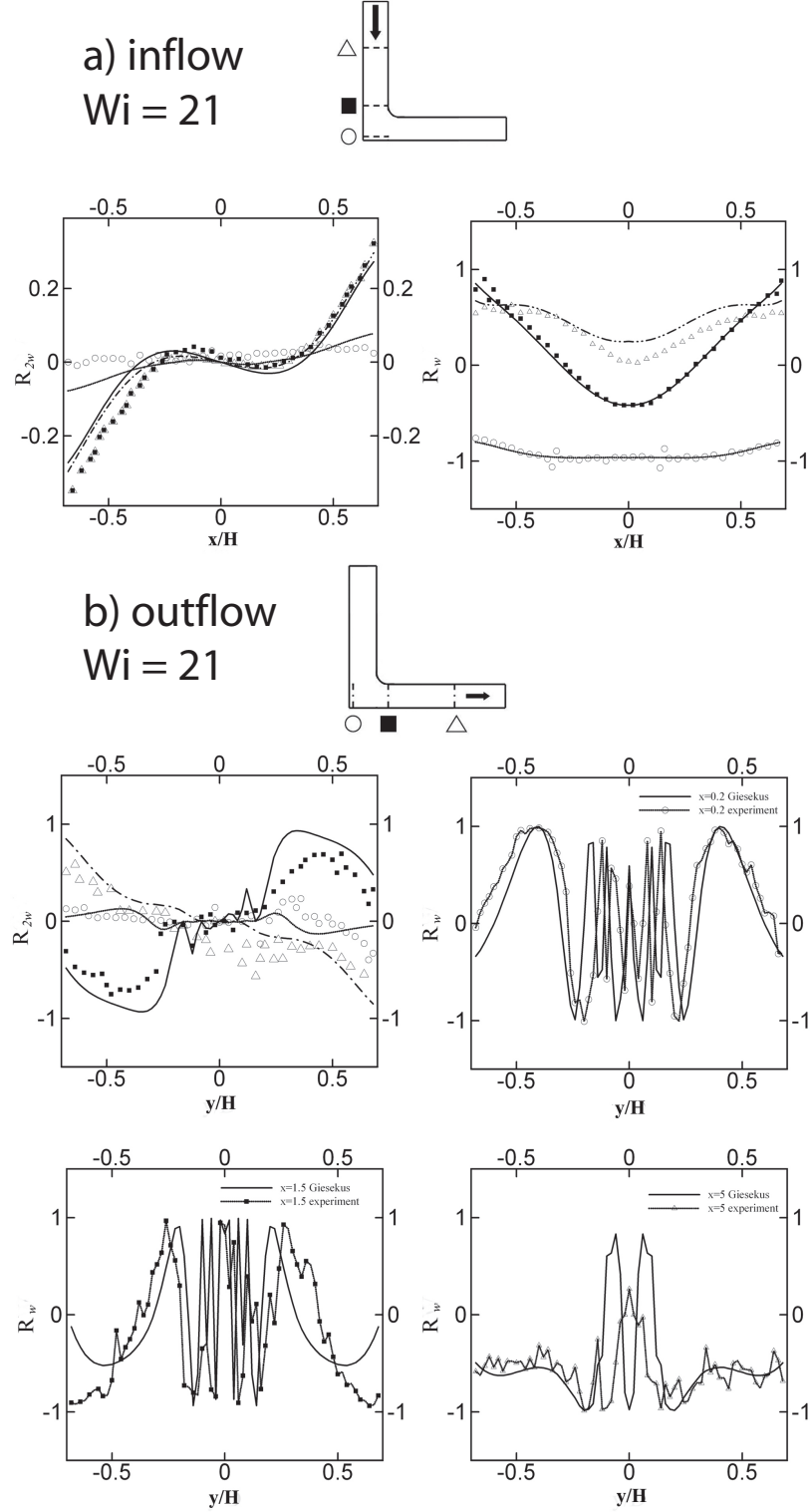


**Figure 3.9:** Comparison between the birefringence data and the viscoelastic flow simulation using the Giesekus model in the a) inflow and b) outflow channels at  $We = 21$ .

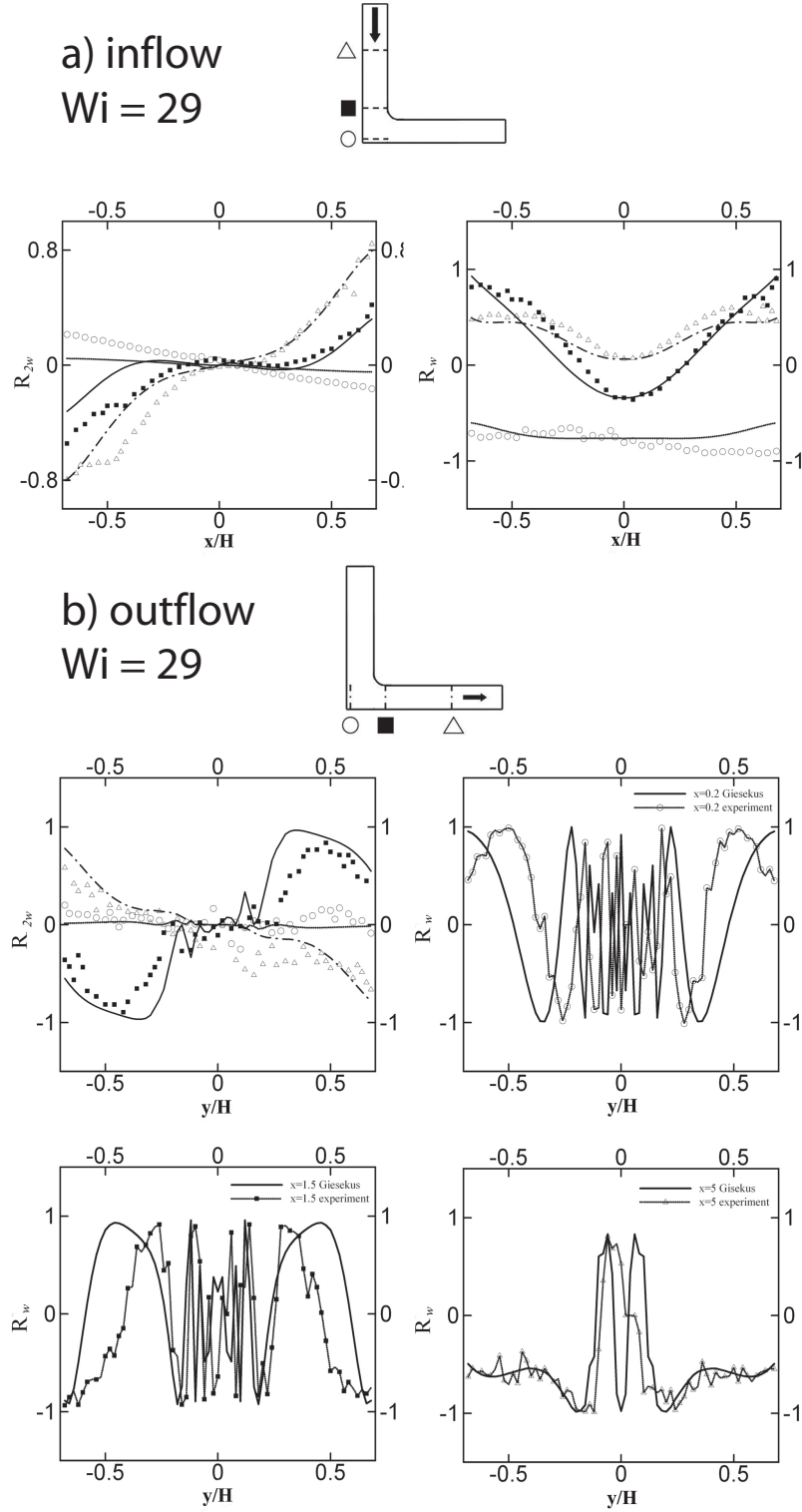


**Figure 3.10:** Comparison between the birefringence data and the viscoelastic flow simulation using the Giesekus model in the a) inflow and b) outflow channels at  $We = 29$ .

optimum slip velocity. Based on these comparisons, it can be concluded that the Giesekus model can accurately predict the flow characteristics at  $We = 21$ . However, the model predictions  $We = 29$  remain qualitative at best. The discrepancy between the numerically predicted and experimentally measured optical properties cannot be solely attributed to the inadequacy of the constitutive model, as the current experimental protocol is ineffective near the stagnation point, as well as along the plane of symmetry in the outlet channel. The limitation of the current experimental technique stems from multiple orders of retardation within the cross section of the laser beam and oil film reflections occurring close to the stagnation point. Overall, this study has clearly demonstrated the potential of this approach to accurately determine the kinematics and stresses in a 2D flow geometry that can be used to evaluate the fidelity of constitutive equations or mesoscopic models of polymer dynamics in mixed kinematic flows. To make this promise a reality, improvements in the experimental method are required. These would involve a new oil delivery design together with a reduction of the laser beam dimensions, as well as more advanced data analysis strategies.

# Chapter 4

## Continuum and multi-scale simulation of mixed kinematics polymeric flows with stagnation points: closure approximation and the high Weissenberg number problem

### 4.1 Introduction

Polymer dynamics in strong flows typically encountered downstream of stagnation points in complex kinematics flows play a central role in determination of many essential fluid dynamics quantities. Examples include, frictional drag on particle and particle-particle interactions [Grillet et al. (1999b)], drop and bubble shape evolution and dynamics [Milliken and Leal (1991); Tiefenbruck and Leal (1982); Arigo et al. (1995)], film thickness in coating flows [Lee et al. (2002)] and a host of internal and

free surface instabilities [Li et al. (2000, 1998); Somasi and Khomami (2000, 2001); Lee et al. (2005, 2002); Bhatara et al. (2004b, 2005a)]. To this end, the non-Newtonian fluid community has developed a number of benchmark problems, namely, flow past a cylinder confined in a channel [Baaijens et al. (1994, 1995)] and sedimentation of sphere in a tube [Yang and Khomami (1999); Arigo et al. (1995)] to examine flow micro-structure coupling downstream of stagnation points on the flow properties including hydrodynamics drag on the objects as well as flow transitions.

Most of the aforementioned studies have had as their focus continuum level computations based on well known constitutive equations for dilute polymeric solutions such as the Oldroyd-B (OLD- B) and Upper Convected Maxwell (UCM) models. However, recently, computations of flow past a cylinder in a channel with the OLD-B constitutive equation has provided evidence of divergent normal stresses in the wake of the cylinder at Weissenberg numbers ( $We$ , defined as the product of the mean polymer relaxation time and a characteristic shear rate) of order 1 [Bajaj et al. (2008)]. Specifically, it has been suggested that this divergence is linked to the unbounded extensional viscosity in the wake of the cylinder. These recent observations based on self-consistent continuum level simulations support earlier assertions by Rallison and Hinch [Rallison and Hinch (1988)] that Hookean dumbbell based constitutive equations such as the UCM, and OLD-B can give rise to unbounded or very large stresses in strong straining flows. Specifically, it was suggested that in presence of unbounded stresses, if the stress tensor is either divergent free or has infinite divergence that is highly spatially localized, there is a negligible effect on the flow, i.e., the flow will not adapt to inhibit infinite stresses or stress gradients.

The influence of finite extensibility of macromolecules on the stress singularity in internal stagnation flows that exhibit divergent free stresses has also been a subject of a number of studies in the past decade. Renardy [Renardy (2006)] utilizing an idealized planar extensional Newtonian flow kinematics has shown that for the Giesekus model, which limits the growth of extensional stresses, although the stress profiles remain finite, the stress gradients can become infinite if  $\alpha$ , the Giesekus

mobility parameter, is less than  $(2 - \sqrt{3})/4$ . Similar behavior has also been observed in idealized uniaxial extensional Newtonian flow kinematics [Becherer et al. (2008, 2009)]. Specifically, it has been shown that although the FENE-P model predicts finite stresses at any  $We$ , for sufficiently large  $bs$ , i.e. square of the maximum molecular extension, there exist a range of  $We$  for which the stress gradients become infinite.

Although to date, observation of infinite stress gradients in strong straining flows with constitutive models that bound extensional stresses has been based on idealized Newtonian kinematics in flows that exhibit divergent free stresses (e.g., flow generated near internal stagnation points in cross-slot and four-roll mill flows), the existence of infinite stress gradients in strong straining flows in a specific parameter range that correspond to highly strain hardening fluids is very intriguing. In fact, one might question the relevance of this interesting finding to the strong dependence of the upper  $We$  limit on the finite extensibility parameter in careful flow computations of dilute polymeric solutions with constitutive equations that bound extensional stresses (e.g., Chilcott-Rallison [Chilcott and Rallison (1988)], FENE-P [Yang and Khomami (1999); Arigo et al. (1995)], the multimode version of the Verhoef et al. model [Verhoef et al. (1999); Arigo et al. (1995)] in geometries with internal stagnation points on solid surfaces (e.g., flow past a cylinder in a channel or sedimentation of a sphere in a tube).

Currently, the cause of the upper  $We$  limit in computation of flows with internal stagnation points on solid surfaces is not known. Clearly, if there is a connection between the aforementioned infinite extensional stresses and the computed stresses in the wake of the cylinder or sphere then one can correlate the existence of an upper bound in  $We$  with appearance of infinite stress gradients in this region. On the other hand the breakdown of the numerical solution at high  $We$  could be solely due to deficiency of numerical techniques [Bajaj et al. (2008)]. To this end, Fattal, [R. Fattal (2004, 2005)] have suggested that the high  $We$  limit could be the result of a numerical instability that can be overcome by use of a variable transformation, namely, a logarithmic transformation of the stresses. However, careful numerical computations of flow past a cylinder in a channel by Hulsén

[Hulsen et al. (2005)] produced converged results with the same upper bound in  $We$  with or without use of this transformation. Finally, it should be noted that the multiscale Brownian Configuration Fields method (BCF) does not suffer from the aforementioned numerical instability. However, one can not correlate the robustness of this simulation technique and its ability to produce converged numerical results at high  $We$  [Hulsen et al. (1997); Laso and Ottinger (1993); Koppol et al. (2009)] solely to this fact since in the BCF formulation a vector field, namely, the connectivity vector of the micromechanical model is convected by the fluid motion (for example in the FENE model) as oppose to a tensor field, namely, the conformation of the macromolecule in the corresponding closed form constitutive equation, i.e., the FENE-P model [Mangoubi et al. (2009)].

To provide further insight into the high  $We$  limitations in continuum level computations of flows with internal stagnation points on solid surfaces, we have performed extensive continuum and multiscale flow simulations in two benchmark flow problems, namely sedimentation of sphere in a tube and flow past a cylinder in a channel, utilizing the FENE-P (continuum and BCF) and Giesekus (continuum) constitutive equations as well as the FENE (BCF) dumbbell micromechanical model. Extremely large stress gradients in the axial normal stress along the plane of symmetry in the wake of the cylinder and sphere are observed in both FENE-P and Giesekus predictions using both multiscale and continuum numerical techniques at  $We$  of  $O(1)$  where the numerical simulations begin to breakdown for significantly strain hardening fluids, i.e.,  $b > 300$ ,  $\alpha < 0.005$ . These very large stress gradients (nearly singular) are a direct consequence of significant over prediction of macromolecular extension by the closed form constitutive equations in the extensionally dominated region of the flow. The inability of the aforementioned constitutive equations to accurately describe the flow microstructure coupling downstream of stagnation points in complex kinematics flows should motivate use of regularization techniques for the stresses [Bhave et al. (1993); Woo et al. (2004a,b)] or utilization of more sophisticated

constitutive equations [Keunings (1997); Lielens et al. (1998); Ghosh et al. (2002)] in flows with strong straining components.

## 4.2 Problem formulation

We consider sedimentation of a sphere along the centerline of a tube and flow past a cylinder mounted in the center of a channel, where both tube and channel are assumed to be filled with a dilute polymeric solution as depicted in figure 4.1 -(a) and (b) respectively. Specifically, we consider two geometries with the sphere-to-tube radius ratios of  $a/R = 0.121$  and cylinder-to-channel radius of  $a/R = 0.5$ . The choice of these two geometries has been motivated by the fact that there is a wealth of experimental data on the drag coefficient and the flow kinematics of well characterized dilute polymeric solution in these two geometries. These systems have been modeled by solving the conservation equations while we have used closed form constitutive equations and a kinetic theory based elastic dumbbell model to describe the polymer's contribution to the total stress, see chapter 2. The simulation parameters have been chosen based on the rheological properties of the same test fluid discussed in chapter 5.

### 4.2.1 Domain discretization and boundary conditions

To find an approximation to the exact solution, the domain  $\Omega$  is divided into a number of four-sided elements, in which the basis functions are defined. Figure 4.2 depict typical domain discretizations used in this study. Mesh refinement has been performed with the criteria that upon each refinement the size of the smallest element near the front and rear stagnation points is reduced by an order of magnitude (see tables 4.1 and 4.2 for details).

The boundary conditions are no-slip and symmetry conditions. Specifically in the case of sedimentation of sphere in a tube, at the tube walls,  $u_r = 0$  and  $u_z = -U_s$ ,

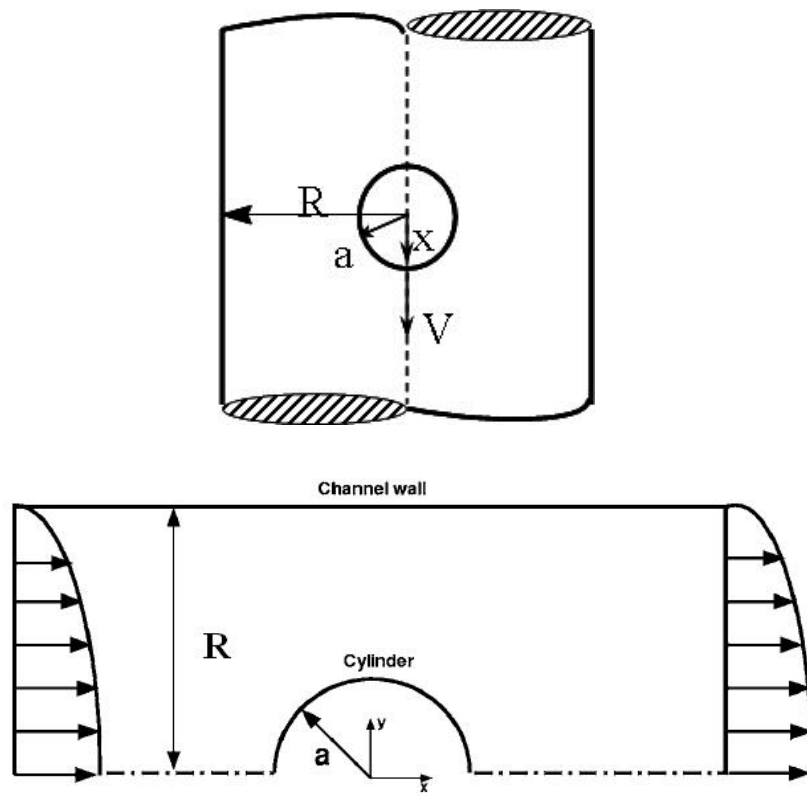


**Figure 4.1:** Schematic of the sedimentation of a sphere in a tube and flow past a cylinder in a channel.

while on the surface of the sphere,  $u_r = u_z = 0$ . In the case of flow past a cylinder confined in a channel, the velocities are set to zero on both channel walls and cylinder surface and fully developed velocity and stress profiles are assumed in the inlet and outlet of the channel. Moreover, at the centerline of both problems  $u_r = \tau_{rz} = 0$ .

## 4.3 Results and discussion

### 4.3.1 Solution Accuracy

The smallest domain discretization used in this study, i.e. 3022 elements, has been shown to provide accurate solutions in prior continuum level simulation with the FENE-P constitutive equation [Yang and Khomami (1999)]. To demonstrate the accuracy of the self-consistent multiscale simulations, the self-consistently computed stress profiles have been compared with those obtained based on a combined Lagrangian/Brownian Dynamics (BD) technique. This approach for establishing the solution accuracy has been adopted since the conventional method of comparing solutions from multiple meshes is highly computationally intensive in the case of multiscale simulations, as evinced by the large number of degrees of freedom at each time step reported in tables 4.1 and 4.2. Specifically, the comparisons are based on the  $\tau_{p,zz}$  component of the polymeric stress because it exhibits large variation with  $We$  along the surface of the sphere and cylinder and near the wake stagnation point, and it greatly influences the total drag on the sphere and cylinder [Arigo et al. (1995); Harlen et al. (1990); Baaijens et al. (1994, 1995)].

Similar to our earlier studies [Koppol et al. (2009)] the Lagrangian determination of the stress involves two steps. First, particle paths are determined via integration of the local self-consistent velocity vector ( $\vec{u}$ ) using the fourth-order Runge-Kutta method. In turn, for the FENE model the BD simulations are conducted along selected streamlines utilizing the semi-implicit predictor scheme of Somasi [Somasi et al. (2002)] with the ensemble size  $N_t = 1024$ . The integrations are carried out

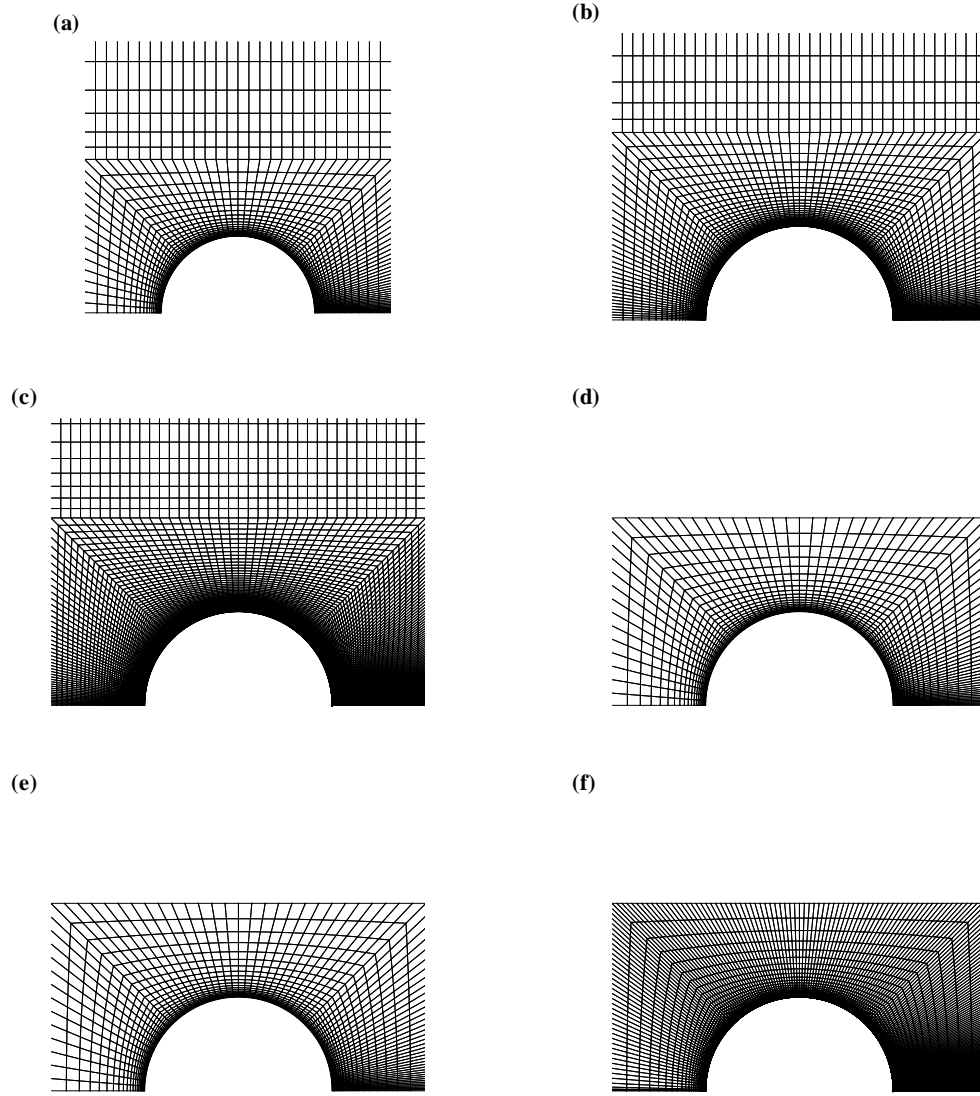


**Figure 4.2:** The computational domain near the surface of the sphere for meshes with 3022 elements, (a), 7500 elements (b) and 18898 elements, (c) ,  $\chi = 0.128$ ; Computational domain near the surface of cylinder for meshes with 2428 elements, (d), 4280 elements, (e) and 17763 elements, (f),  $\chi = 0.5$ .

Variable	3022 elements	7577 elements	18898 elements
DOF: $\vec{u}$	40,535	100,443	232,678
DOF: $\underline{\underline{G}} \& \underline{\underline{\tau}}$	25,288	62,344	144,128
DOF: $\vec{Q}$ ; $N_f = 960$	28,657,626	177,142,683	1,021,399,104
Aspect ratio of smallest element	0.01	0.001	0.0001

**Table 4.1:** Degrees of freedom (DOF) for each variable and the ratio of the width of the smallest element of each mesh to the sphere radius.

Variable	2428 elements	4280 elements	17378 elements
DOF: $\vec{u}$	32,567	46,736	213,963
DOF: $\underline{\underline{G}} \& \underline{\underline{\tau}}$	20,317	35,216	132,535
DOF: $\vec{Q}$ ; $N_f = 960$	23,024,724	100,062,120	939,246,144
Aspect ratio of smallest element	0.01	0.001	0.0001

**Table 4.2:** Degrees of freedom (DOF) for each variable and the ratio of the width of the smallest element of each mesh to the cylinder radius.

by varying  $\delta t$  such that the magnitude of  $\vec{u}\delta t$  is fixed to a constant,  $4 \times 10^{-4} \leq A \leq 2 \times 10^{-2}$ . Specifically, the constant is set to  $A$  when  $z \in [20, 40]$ ,  $5A$  when  $z \in [10, 20]$  and  $[40, 50]$ , and  $25A$  when  $z \in [0, 10]$  and  $[50, 60]$ . With  $1 \times 10^{-4} \geq A$ , converged results in the  $We$  range of interest are obtained. At this level of refinement, highly spatially resolved polymer stresses are obtained. Hence, the computed stresses utilizing the Lagrangian/BD procedure should provide a stringent test of the self-consistent computed stresses.

To investigate the effect of Peterlin approximation on the polymer segmental connectivity distribution function, the distribution functions predicted by FENE and FENE-P models are compared. To this end, we have also used the stochastic description of the FENE-P dumbbell model. In our first approach, the kinematics is calculated from self consistent continuum level flow simulation using the closed form FENE-P model. These kinematics are in turn used to calculate the flow streamlines using Lagrangian integration. By solving the stochastic equation with known kinematics, the polymer configurations and stresses along specified streamlines

are obtained. The BD simulation for the FENE-P model is performed with a similar algorithm used for the FENE model, except, due to the presence of the term  $\langle \vec{Q}\vec{Q} \rangle$ , which depends on  $\vec{Q}$  values of all the dumbbells, the second step upon rearrangement results in a set of highly nonlinear system of equations [Koppol et al. (2009)]. In order to solve this set of equations, we split the term  $\langle \vec{Q}\vec{Q}^{n+1} \rangle$  into  $\langle \vec{Q}\vec{Q}^{n+1} \rangle$  for the dumbbell for which  $|\vec{Q}|$  is being solved and  $\langle \vec{Q}\vec{Q}^n \rangle$  for the rest of the dumbbells. This again leads to a cubic equation that can be easily solved [Li et al. (2006)]. Once every  $\langle \vec{Q}^{n+1} \rangle$  is known, the residual  $\epsilon$  is calculated as the difference between the solutions  $\vec{Q}$  and  $\langle \vec{Q}^{n+1} \rangle$  according to the following equation:

$$\epsilon = \sqrt{\sum_{i=1}^{N_s} (\vec{Q}_i^{n+1} - \vec{Q}_i)^2} \quad (4.1)$$

where  $N_s$  is the number of dumbbells. The corrector step is repeated until numerical convergence is achieved. Once all the  $\vec{Q}$ s have been evaluated, the polymeric stress  $\underline{\underline{\tau_p}}$  is obtained using the Kramer's expression. Finally, this algorithm is used to perform self consistent BCF simulations with the FENE-P model.

Figures 4.3-(a) and (c) depict comparison of prototypical steady state  $\tau_{pzz}$  profiles along streamlines near the centerline of the channel in the vicinity of the sphere and cylinder respectively, at  $We = 2$  and finite chain extensibility,  $b = 900$ . Overall, the excellent agreement between the self-consistent simulations with 18898 and 17378 elements and the Lagrangian-based results clearly demonstrate the accuracy of the self-consistent multiscale simulation results.

Figures 4.3-(b) and (d) also depict a comparison between the Eulerian (continuum), multiscale (BCF) and Lagrangian FENE-P results for the sphere and cylinder cases respectively. The agreement between the self-consistent continuum simulations, the Lagrangian-based and the BCF results (10 % maximum deviation), justifies the use of the Lagrangian/BD simulation to construct accurate (in comparison to BCF due to smaller number of fields to make computations tractable) probability density function of the segmental connectivity vector of the FENE-P model.

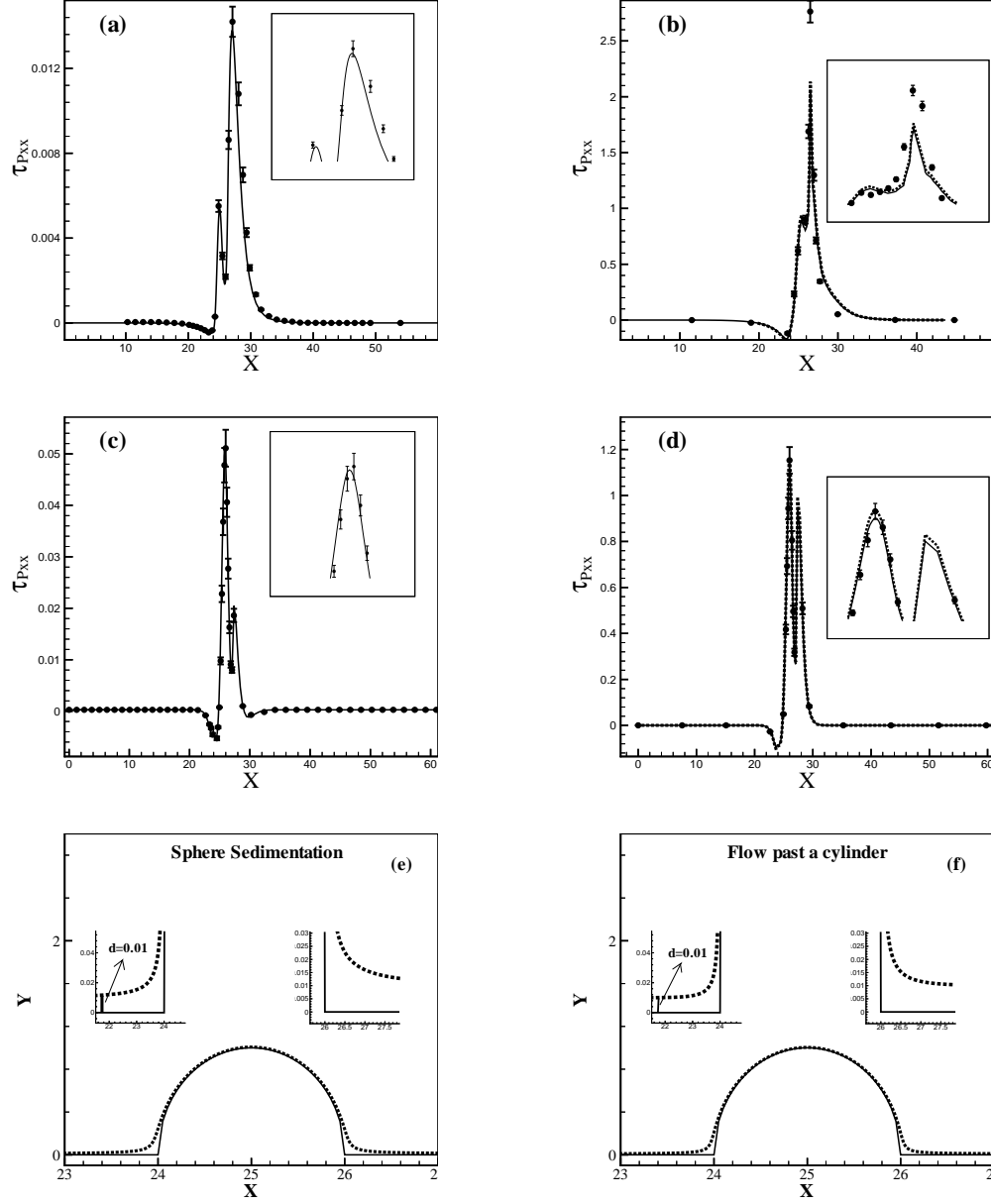


**Figure 4.3:** Comparison of prototypical steady state  $\tau_{pzz}$  profiles for the FENE, (a) and (c), and the FENE-P, (b) and (d), models predicted using self-consistent simulations, solid line, Lagrangian-based integration, circles, and FENE-P BCF, dotted line, along streamlines shown in (e) and (f) the surface of the sphere ( (a) and (b) and cylinder ((c) and (d)).

### 4.3.2 Simulation results

It has been suggested that the use of OLD-B constitutive equation (Hookean dumbbell model) in simulations of flow past a cylinder confined in a channel will lead to solution divergence in the wake of the cylinder, at  $We \approx 1.1$  [Bajaj et al. (2008)]. The solution divergence has been linked to the prediction of an unbounded extensional viscosity in the planar extensional flow region downstream of the cylinder. It has also been conjectured that using models that bound the extensibility of polymer molecules such as the FENE-P constitutive equation, should enable numerical simulations at much higher  $We$ . However, our simulations in the two aforementioned flow geometries with a typical mesh; one with a uniaxially (sedimentation of sphere) dominated wake regime and the other with a planar extensional (flow past a cylinder confined in a channel) dominated wake flow regime begin to breakdown for  $b > 300$  at  $We \approx 2.0$  and  $We \approx 1.0$  respectively. To investigate the possible numerical and physical underpinning of this divergence, the calculations were repeated with much more refined meshes. Specifically, computations with highly refined meshes near the stagnation points of these flows for a vast range of chain maximum extensibilities have been performed. The results of our hi-fidelity computations are summarized below.

#### Flow past a cylinder confined in a channel

Our continuum (DEVSS-SUPG; 2428 to 17378 elements) and multiscale (BCF; 4280 elements) FENE-P simulations of flow of a dilute polymeric solution past a cylinder with  $b = 900$  breakdown at  $We = 1.1$ . However computations with  $b < 300$  could be continued until they were stopped at  $We \approx 5$ . Moreover, simulations with the FENE micromechanical model could also be continued well beyond  $We$  of 1 for  $b = 900$ . Specifically, we were able to find converged solutions up to  $We \approx 3$  where the simulations were stopped.

The origin of the failure of computations with the FENE-P model at  $O(1)$   $We$  with  $b > 300$  is the rapid increase in the axial polymeric stresses and their gradients

as a function of  $We$  in the wake of cylinder as depicted in figures 4.4-(a), (b) and (d). The existence of very high stress and stress gradients for strain hardening fluids at the  $We$  where the solution begins to breakdown is further demonstrated in figure 4.4-(c) where the  $\tau_{pzz}$  profile along the channel center line and the surface of the cylinder using meshes with different level of refinement is shown. The lack of mesh converged axial stresses near the point of the maximum stresses is attributed to the exponential growth of stress gradients near the stagnation point for  $b > 300$ . It should also be noted that the FENE-P stress gradients computed based on continuum and BCF techniques are at least an order of magnitude greater than the FENE stress gradients at the same  $b$  (see figure 4.4-(e) and 6-(a)). To ascertain the origin of this very large localized stresses and stress gradients in FENE-P computations, we have examined the details of the macromolecular configuration at various  $We$  for both models.

Using the aforementioned combined Lagrangian/BD techniques and the BCF simulation of FENE and FENE-P models, the probability distribution function of the dumbbell connectivity vector along selected streamlines, shown in figure 4.3-f, is examined. A close inspection the PDF of  $|\vec{Q}|$  at the point where  $\tau_{pzz}$  is maximum downstream of the stagnation point (see figures 4.4-(f)), demonstrates that a large fraction of the total stress, up to 65%, are due to configurations with  $|\vec{Q}|$  larger than the maximum extensibility of the polymer molecule. Although extended states have been previously observed in the turbulent channel flow and uniaxial channel flow of dilute polymeric solutions, [Keunings (1997); Gupta et al. (2004)], their influence on flow micro-structure coupling in complex kinematics flows has not been examined. The occurrence of the over-extended states and the corresponding large localized polymeric stresses and stress gradients at the critical  $We$  where both continuum and multiscale FENE-P calculations begin to breakdown is not observed in multiscale FENE simulations (see figure 4.5).

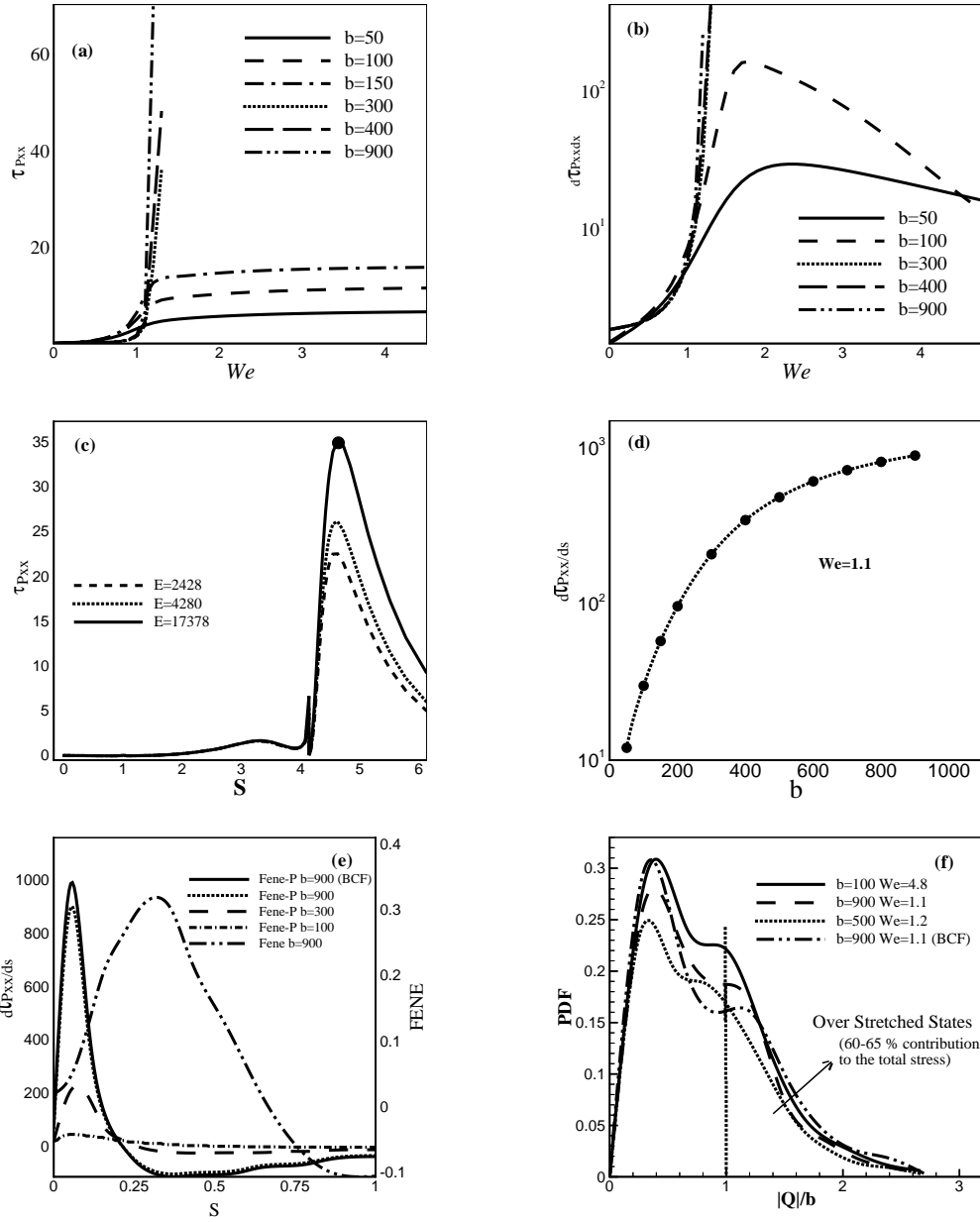


**Figure 4.4:** (a):  $\tau_{p_{zz}}$  vs.  $We$ , (b):  $d\tau_{p_{zz}}/ds$  vs.  $We$ , (c):  $\tau_{p_{zz}}$  along the cylinder surface and channel center line. (d):  $d\tau_{p_{zz}}/ds$  vs.  $b$  (e):  $d\tau_{p_{zz}}/ds$ , along the cylinder surface and channel center line. (f) Probability density function (PDF) of nondimensionalized end-to-end distance  $|\vec{Q}|/b$ . (All the results are at  $We = 1.1$ ,  $b = 900$  and from the mesh  $E = 17378$  otherwise mentioned.)

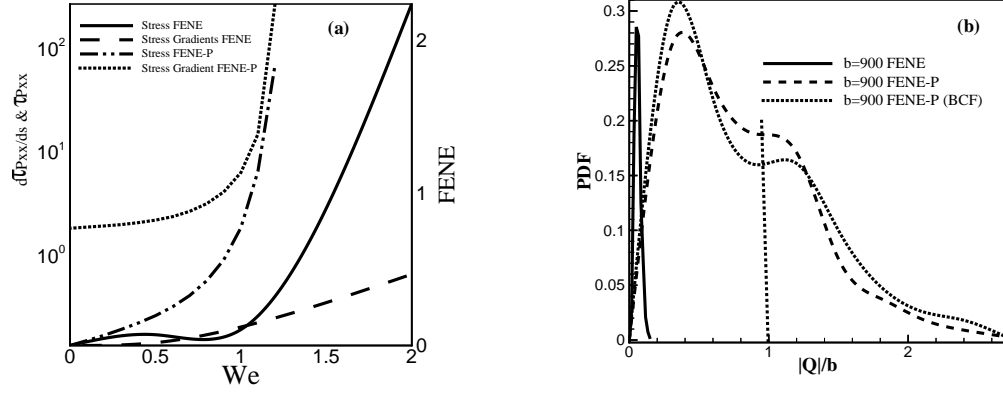


**Figure 4.5:** (a):  $\tau_{pzz}$  and  $d\tau_{pzz}/ds$  vs  $We$  and (b) Probability density function (PDF) of nondimensionalized end-to-end distance  $|\vec{Q}|/b$  predicted by the FENE and the FENE-P models.

### Sedimentation of a sphere in a tube

In the wake region of the sphere at the  $We \approx 2$  when the computations with the FENE-P model for  $b > 300$  begins to breakdown, we observe very similar behavior in axial stresses to that of flow past a cylinder, namely, very large and highly localized stresses as well as very large stress gradients (see figure 4.6). We also observe the over-extended states and in this flow problem their contribution to the total stress is  $\approx 70\%$ . Moreover, the BCF multiscale FENE-P simulations could only be continued up to  $We = 1.95$  for  $b = 900$  with a 7577 elements mesh and  $b = 900$ . As expected, the probability distribution function of the dumbbell connectivity vector computed with both BCF and the Eulerian/Lagrangian method based on continuum level self consistent velocities are very similar. Moreover, the predicted kinematics and stresses by BCF and continuum simulations with the FENE-P model are similar (see figure 4.7). Hence, it is reasonable to assume that the breakdown of continuum and multi-scale computations with the FENE-P model is directly related to the highly localized and large polymeric stresses and stress gradients in the wake of the sphere.

To further examine the relationship between large polymeric stresses and stress gradients and the upper  $We$  limitations in complex kinematics flows with stagnation

points on solid surfaces, we have performed continuum level simulations with the Giesekus model with various mobility parameters and have found that for  $\alpha < 0.006$  the computations begin to breakdown at  $We \approx 2$  (see figure 4.6) due to existence of very large axial stresses and stress gradients in the wake of the sphere. Interestingly, the Giesekus model with  $\alpha$  of 0.006 gives rise to the same steady elongational viscosity as the FENE-P model with  $b = 333$  in the limit of high extension rates ( $b \approx \frac{2}{\alpha}$  in this limit). Once again, the large stress and stress gradients computed with commonly used closed form constitutive equations for dilute polymeric solutions in the wake of the solid object for highly strain hardening fluids is not observed in multiscale simulations with the FENE model. Specifically, the computed axial stress and its gradient is at least an order of magnitude smaller than the FENE-P and Giesekus model for fluids with similar strain hardening characteristics. (see figure 4.6-(e)). Moreover, we were able to find converged solutions with the FENE micromechanical model well beyond  $We$  of 2 for  $b = 900$ .

To this point, a strong correlation between significant contribution of over stretched states to the total polymeric stress and its gradient, and divergence of numerical simulations in both benchmark problems with the FENE-P and Giesekus models for highly strain hardening fluids, irrespective of the numerical method, i.e. continuum (DEVSS-SUPG) or multiscale (BCF) has been established. Clearly, in this class of flows the macromolecules are pre-stretched before entering the wake of the solid object. To ascertain the degree of molecular stretch computed in the shear dominated region of the flow near the solid surface and its implications on the rapid stress growth observed in the wake of the solid objects, we have computed the PDF of the polymer molecules along selected streamlines very close to the surface of the cylinder. Sample PDFs for both the FENE and FENE-P models at various locations along a typical streamline are shown in figure 4.8. Clearly, a higher polymer stretch is observed near the surface of the sphere with the closed form constitutive equation. Once these stretched polymers are convected into the wake of the sphere where the flow is extensionally dominated, a very large jump in the axial polymeric stresses

is observed. Moreover, this jump in stresses is much more significant for the closed form constitutive equation due to a large pre-stretch. This finding further supports the existence of large localized polymeric stresses and stress gradients downstream of the stagnation point in computations with FENE-P model.

To examine the consequence of the over prediction of polymeric stresses and stress gradients by the FENE-P model on the kinematics in the wake of the sphere, we have carefully examined the axial velocity downstream of the sphere at the centerline. For highly strain hardening fluids, i.e.,  $b = 900$ , a transition in the velocity profile at  $We = 1.95$  is observed. Specifically, very near the stagnation point a small region with a high strain rate is observed (see figure 4.9-a). In fact, the strain rate in this region is at least twice that of the region further downstream of the sphere. This finding is consistent with observation of highly localized large stresses and nearly infinite stress gradients downstream of the stagnation point predicted by the closed form constitutive equations. This phenomenon is not observed in FENE simulations at a similar  $b$  and  $We$  (see figure 4.9-c). Moreover, this localized high strain rate region is not observed in FENE-P computations with  $b < 300$ . Despite this fact, the kinematics downstream of the sphere computed with the FENE-P model with  $b < 300$  could be qualitatively different than those computed by FENE simulations. For example, at  $b = 100$ , FENE-P computations show a separated flow regime close to the stagnation point downstream of the sphere (see figures 4.9-(b) and 4.10) while FENE simulations do not exhibit a recirculation regime (see figures 4.10). Therefore, the fidelity of FENE-P model predictions at  $We$  where a significant portion of the polymeric stress arises due to over-stretched states is questionable. Since, over-stretched states exist in all strong straining flows irrespective of  $b$  values, regularization techniques for polymeric stresses should be considered where utilizing the FENE-P and Giesekus constitutive equations in flows with strong straining components.

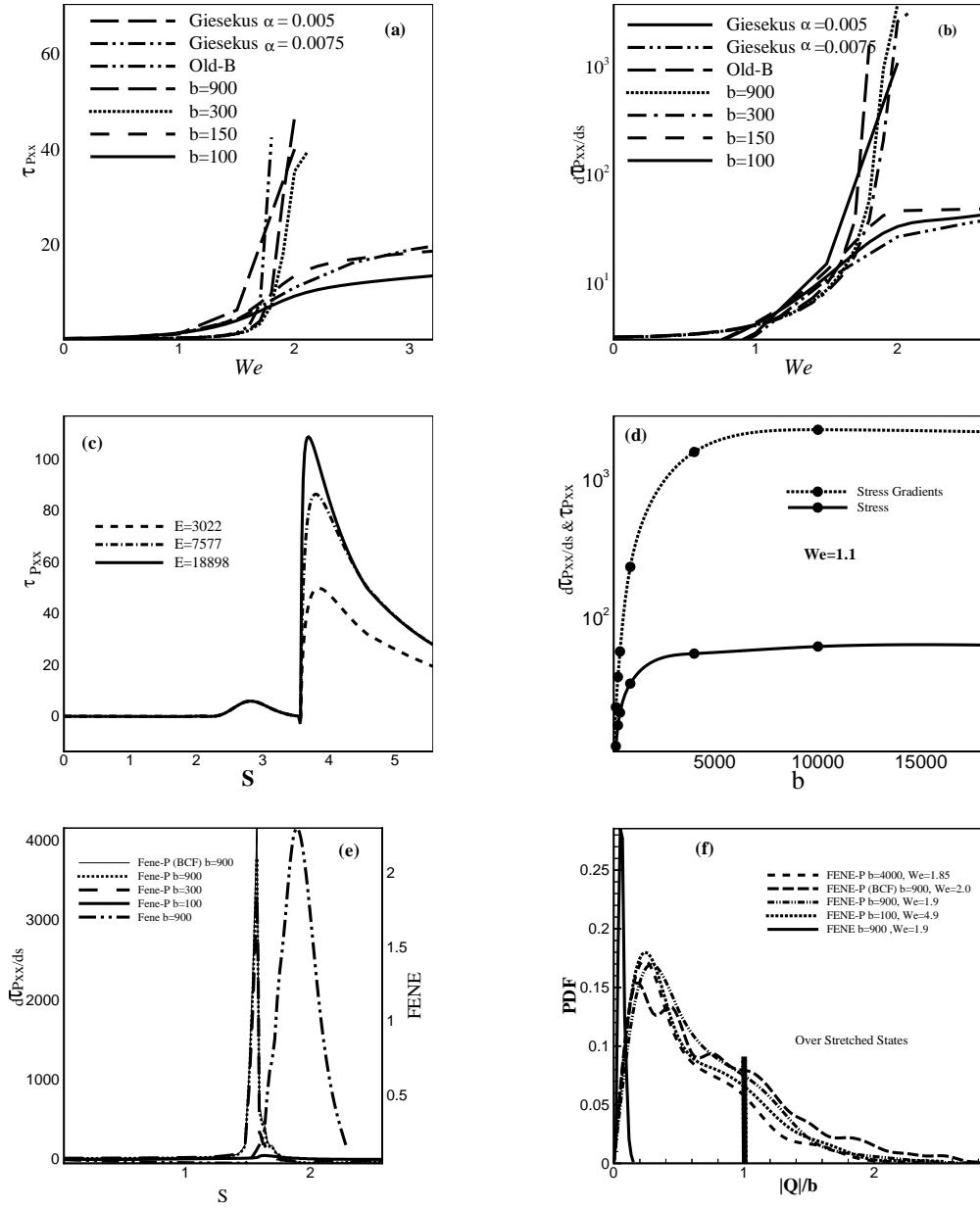


**Figure 4.6:** (a):  $\tau_{pzz}$  vs.  $We$ , (b):  $d\tau_{pzz}/ds$  vs.  $We$ , (c):  $\tau_{pzz}$  along the sphere surface and tube center line. (d):  $d\tau_{pzz}/ds$  vs.  $b$  (e):  $d\tau_{pzz}/ds$ , along the sphere surface and tube center line. (f) Probability density function (PDF) of nondimensionalized end-to-end distance  $|\vec{Q}|/b$ . (All the results are at  $We = 2.0$  and from the mesh  $E = 18898$  unless otherwise noted.)

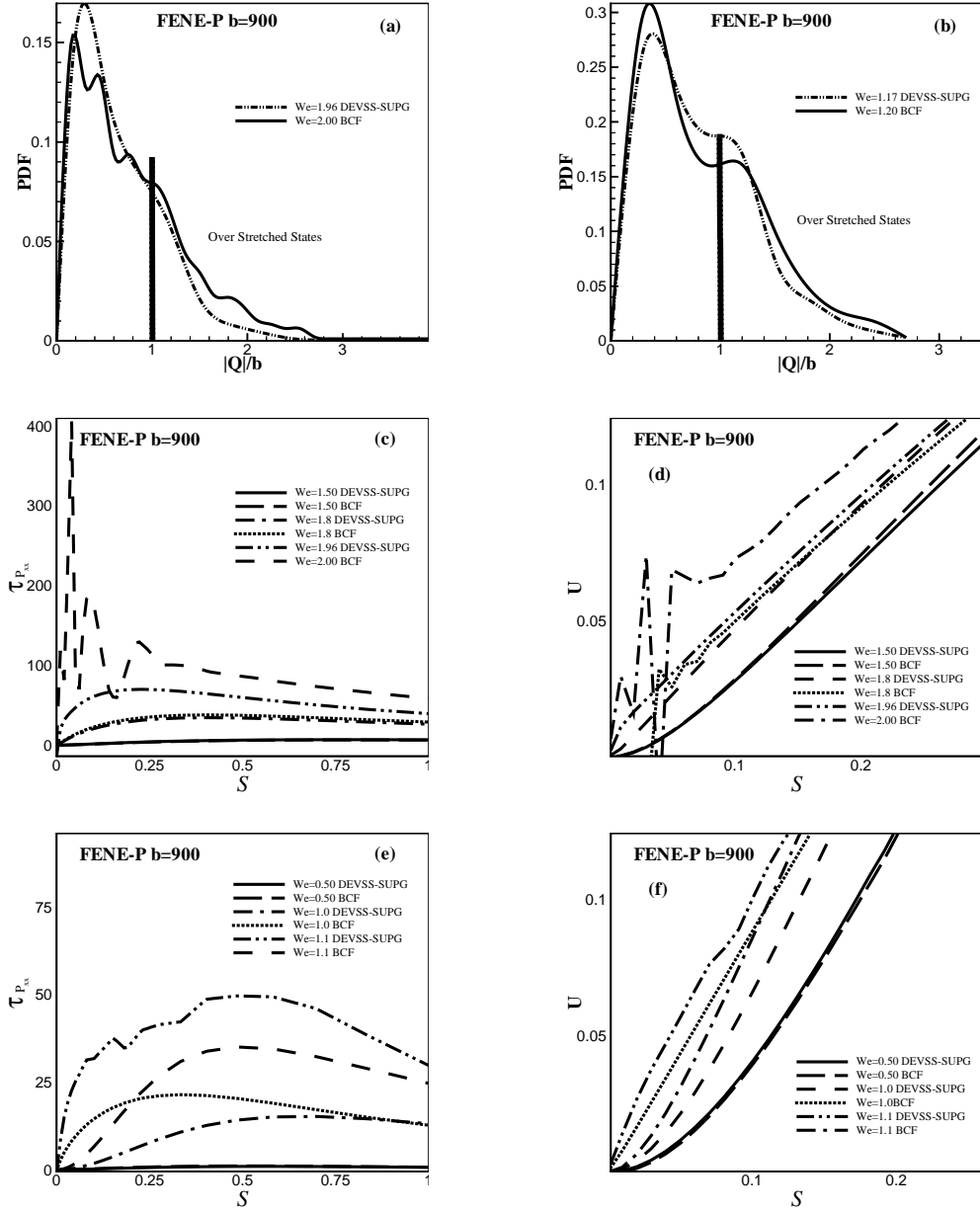


**Figure 4.7:** Probability density function (PDF) of nondimensionalized end-to-end distance  $|\vec{Q}|/b$  at the point of maximum stress near the rear stagnation point of sphere (a) and cylinder (b). Velocity and stress in the  $z$  direction ( $\vec{U}$  and  $\tau_{p_{zz}}$ ), along the center line of the tube/channel near the rear stagnation point of the sphere (c) and (d), and cylinder (e) and (f)

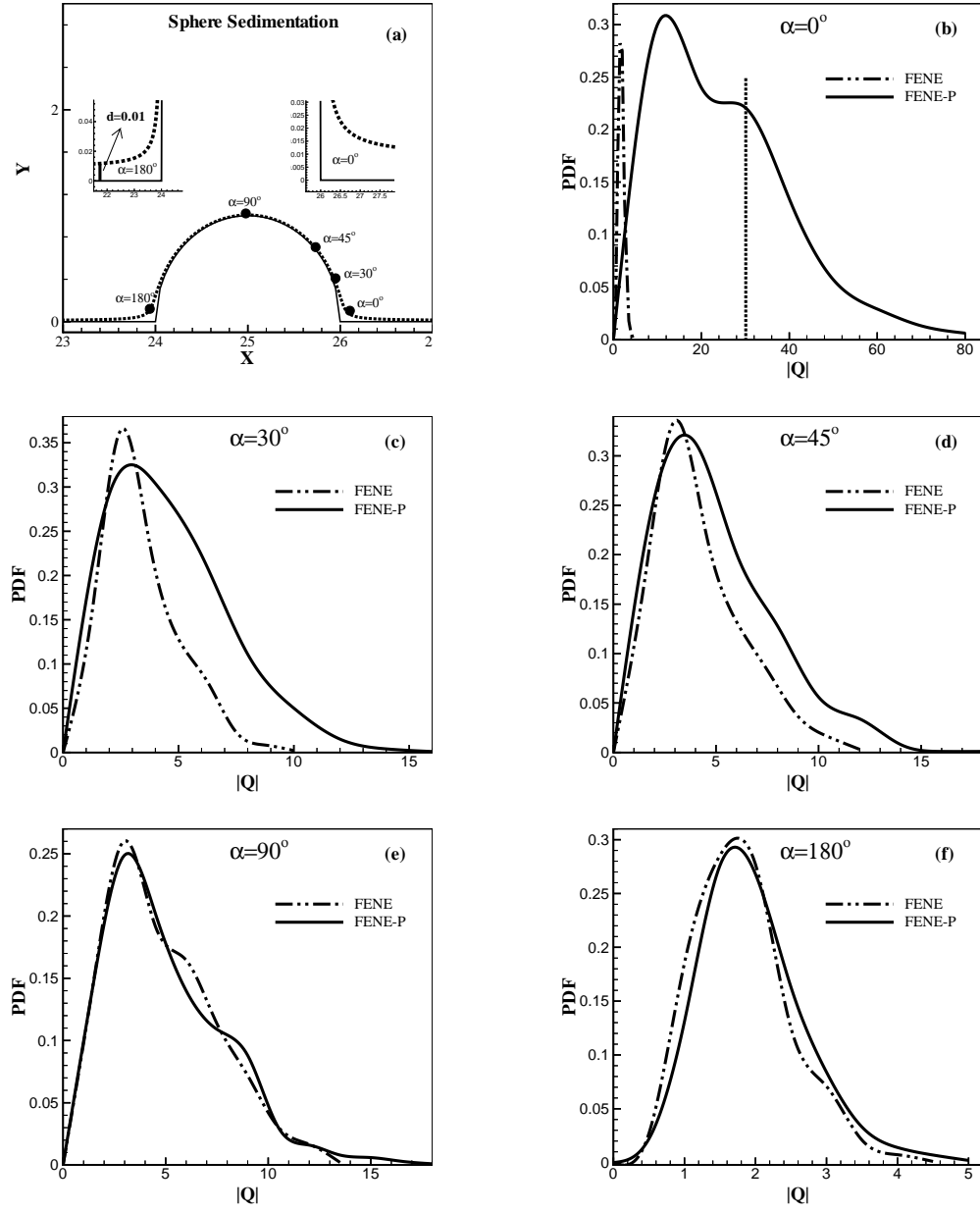


**Figure 4.8:** Probability density function (PDF) of end-to-end distance of polymer molecules along the surface of the sphere predicted by the FENE-P and the FENE models. (a): The location of point along streamline where the PDF's have been calculated.

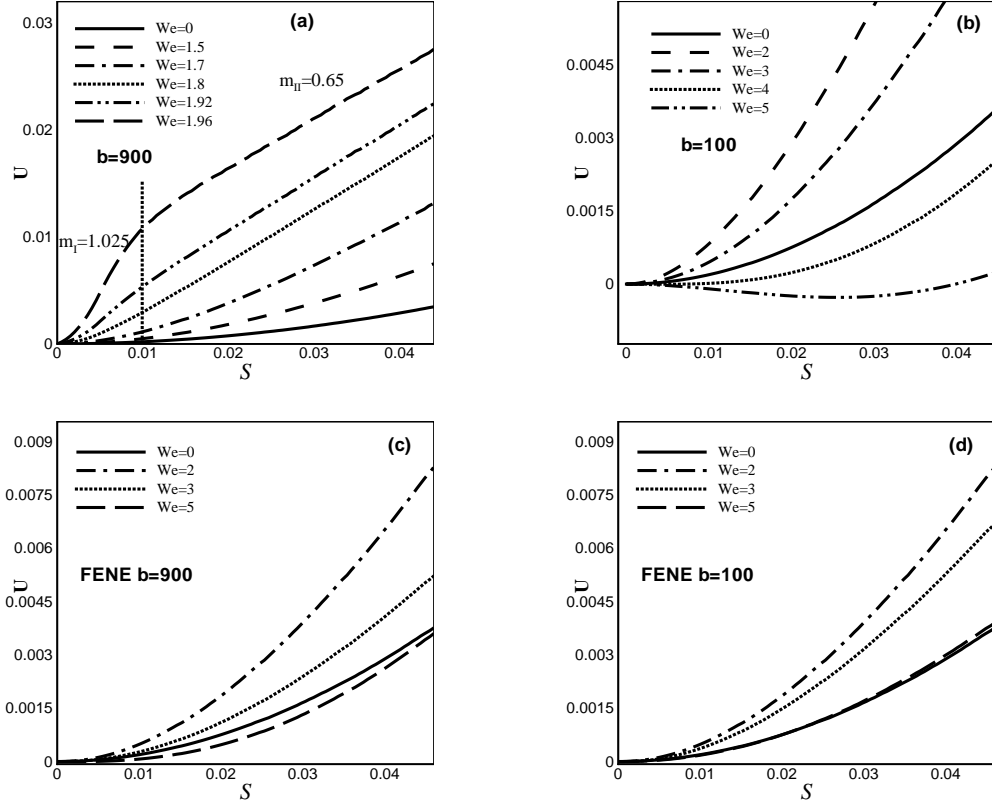


**Figure 4.9:** Velocity in the  $z$  direction ( $\vec{U}$ ), along the center line of the tube near the rear stagnation point of the sphere predicted by the FENE-P,(a,b), and the FENE,(c,d), models.

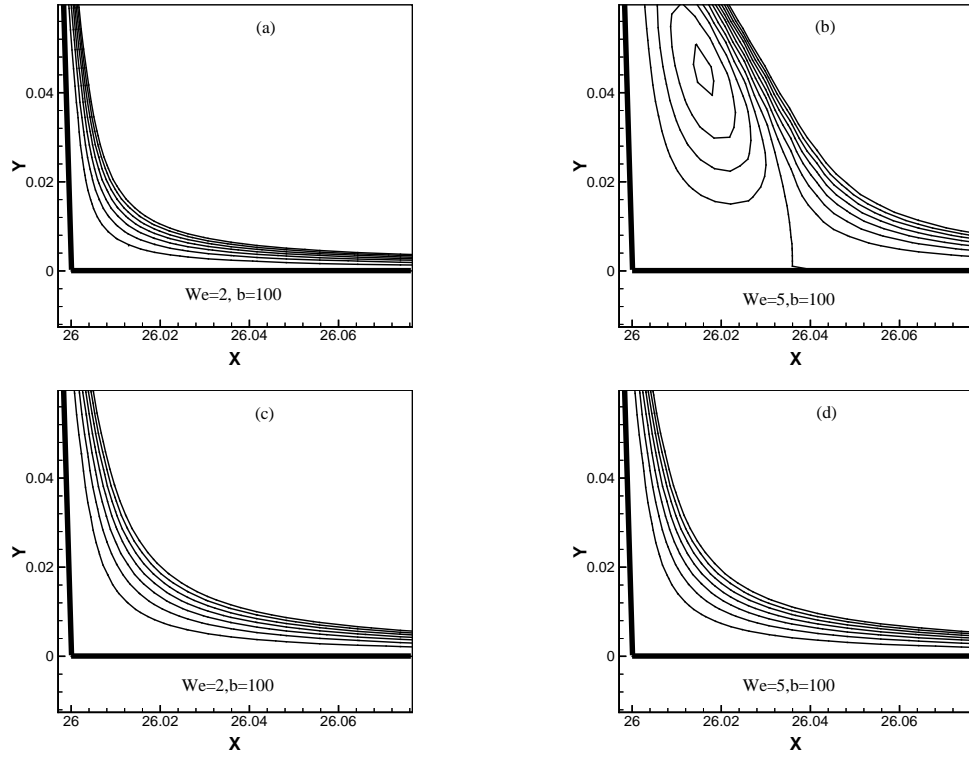


**Figure 4.10:** Streamlines near the rear stagnation point at  $We = 2, 5$ ; a,b FENE-P; c,d, FENE

## 4.4 Conclusion

We have performed extensive continuum and multiscale flow simulations in two benchmark flow problems, namely sedimentation of sphere in a tube and flow past a cylinder in a channel, utilizing the FENE-P (continuum and BCF) and Giesekus (continuum) constitutive equations as well as the FENE (BCF) dumbbell micromechanical model to provide insight into the dependence of the upper We limit encountered in continuum level viscoelastic flow simulations with typical constitutive equations for dilute polymeric solutions that predict bounded extensional viscosities in geometries with internal stagnation points on solid surfaces. To this end, a strong correlation between significant contribution of over-stretched states to the total polymeric stress and existence of very large and localized polymeric stress gradients and divergence of numerical simulations in both benchmark problems with the FENE-P and Giesekus models for highly strain hardening has been established. The consequence of the over prediction of polymeric stresses and stress gradients by the FENE-P model in comparison to the FENE model on the kinematics in the wake of the solid objects has also been examined. In general, closed form constitutive equations can either give rise to very highly localized region of high strain rate or recirculation regions downstream of the object that are absent in the corresponding multiscale simulations with the FENE model. Hence, the accuracy of FENE-P model predictions at  $We$  and  $b$  values where a significant portion of the polymeric stress arises due to over-stretched states is questionable. Hence, regularization techniques for polymeric stresses should be used in FENE-P computation of flows with strong straining components.

# Chapter 5

## Sedimentation of a sphere in a viscoelastic fluid: a multiscale simulation approach

### 5.1 Introduction

One of the principal concerns of fluid mechanics is to develop a fundamental and quantitative understanding of global variables such as pressure drop, hydrodynamic drag and dissipation as functions of flow rate, geometry and boundary conditions. The technological importance of such knowledge cannot be overemphasized. For Newtonian flows, especially under laminar flow conditions, these relationships can be easily determined using either well established analytical techniques or with the aid of readily available commercial software packages. However for polymeric flows, despite the tremendous progress in development of numerical techniques and constitutive theories in the past decade, continuum level computations are still incapable of quantitatively predicting macroscopic variables such as frictional resistance enhancement (FRE) in prototypical extension-dominated, mixed kinematics creeping flows of dilute polymeric solutions such as contraction/expansion flows [Quinzani et al.

(1994); Rothstein and McKinley (1999, 2001); Koppol et al. (2009)], and flow past bluff objects [Li et al. (1998, 2000); Baaijens et al. (1994, 1995); Arigo et al. (1995); Yang and Khomami (1999)].

In the past two decades, coordinated experimental/computational studies of dilute polymeric solutions in a number of benchmark problems have clearly demonstrated that the aforementioned lack of quantitative prediction of FRE is due to the inability of constitutive equations to quantitatively capture the polymeric body forces that result from the configurational complexity of the macromolecules in mixed kinematics flows with strong straining components [Abedijaberi and Khomami (2011); Abedijaberi et al. (2008); Burghardt et al. (1999b); Li et al. (1998, 2000); Perkins et al. (1997); McKinley (2001); Lunsmann et al. (1993); Satrape and Crochet (1994); Arigo et al. (1995); Rasmussen and Hassager (1996); Yang and Khomami (1999); Grillet et al. (1999b); Talwar and Khomami (1995)]. In fact this realization has been the main motivating factor for development of multiscale simulation techniques that couple kinetic theory based micromechanical models for polymer dynamics at the mesoscopic level with macroscopic equations of change to self consistently capture the intricate coupling between flow deformation and macromolecular configuration during flow [Laso and Ottinger (1993); Ottinger et al. (1997); Hulsen et al. (1997); Halin et al. (1998); Somasi and Khomami (2000, 2001); Wapperom et al. (2000); Gigras and Khomami (2002)]. However, despite significant algorithmic advances in the past several years, multiscale flow simulation techniques still remain highly computationally intensive in comparison to their continuum level counterpart. Hence, to date most of the large scale complex kinematics multiscale flow simulations of dilute polymeric solutions have been performed with the simplest micromechanical model for polymer molecules, namely, the elastic dumbbell model. Although this class of simulations have provided significant insight in understanding the influence of closure approximations on prediction of polymeric stresses in mixed kinematics flows of dilute polymeric solutions, they are still unable to quantitatively predict FRE and other important flow quantities such as vortex dynamics, velocity wake and stress wake

structure in creeping flow benchmark problems such as contraction/expansions flows or flow past bluff objects [Wapperom et al. (2000); Rothstein and McKinley (1999, 2001)].

The inability of multiscale simulations with single segment kinetic theory based models to provide quantitative prediction of macroscopic flow quantities in extension dominated complex kinematics flows can be rationalized in terms of recent fluorescence microscopy studies of model macromolecules, namely DNA, under flow that have clearly demonstrated the necessity of multi-segment micromechanical models such as bead rod and bead spring chains for quantitative prediction of macromolecular dynamics [Doyle et al. (1998); Shaqfeh (2005); Larson (2005); Somasi and Khomami (2000, 2001)]. These findings clearly underscore the fact that a multi-segment description of the macromolecule or reduced order coarse grained models capable of retaining the essential physics associated with the internal degrees of freedom of the macromolecule are required for accurate modeling of dilute polymer solutions under flow [Venkataramani et al. (2008a,b)]. To this end, we have recently performed multiscale simulations of flow of a highly elastic dilute polymeric solution through a 4:1:4 axisymmetric contraction and expansion geometry and for the first time demonstrated that the pressure drop evolution as a function of flow rate can be accurately predicted when the chain dynamics is described by multi-segment bead spring micromechanical models that closely captures the transient extensional viscosity of the experimental fluid. Specifically, for the first time the experimentally observed doubling of the dimensionless excess pressure drop at intermediate flow rates was predicted [Koppol et al. (2009)].

Motivated by the aforementioned success in quantitatively describing the frictional resistance enhancement in flow of dilute polymeric solutions in contraction/expansion flows, we have turned our attention to flow of dilute polymeric solutions past bluff objects. This choice has been motivated by the fact that in creeping viscoelastic flows past objects such as cylinders or spheres the relationship between FRE and the flow rate and the wake structure (velocity and stresses) cannot be accurately

predicted by continuum level or multiscale simulations with simple micromechanical models [Baaijens et al. (1994, 1995); Lunsmann et al. (1993); Satrape and Crochet (1994); Arigo et al. (1995); Rasmussen and Hassager (1996); Yang and Khomami (1999); McKinley (2001)]. Specifically, in the case of the two well known benchmark flow problems, namely, flow past a cylinder in a channel and sedimentation of a sphere in a tube, utilization of commonly used constitutive equations such as FENE-P and Giesekus models for significantly strain hardening fluids leads to unrealistically large localized polymeric stresses and stress gradients in the wake of the object, thereby preventing accurate prediction of FRE and the wake structure [Abedijaberi and Khomami (2011); Baaijens et al. (1994); Somasi (2001); Baaijens et al. (1995)]. To this end, results of a self consistent multiscale flow simulation for sedimentation of a sphere in a tube filled with a Boger fluid composed of 0.21 wt% polyisobutylene (PIB), 4.83 wt.% tetradecane (C14), and 94.86 wt% polybutene (PB), is presented that for the first time provides a quantitative prediction of the enhanced drag coefficient and the extended wake structure observed experimentally at high  $We$ .

## 5.2 Problem Formulation

We consider sedimentation of a sphere along the centerline of a tube filled with a dilute polymeric solution as depicted in figure 5.1. Specifically, we consider two geometries with the sphere-to-tube radius ratio of  $\chi = a/R = 0.121$  and  $\chi = 0.243$ . This choice has been motivated by the fact that there is a wealth of experimental data on the drag coefficient and the flow kinematics of well characterized dilute polymeric solution in these two geometries [Arigo et al. (1995)].

### 5.2.1 Domain discretization and boundary conditions

To find an approximation to the exact solution, the domain  $\Omega$  is divided into a number of four-sided elements, in which the basis functions are defined. Figure 5.2

depict typical domain discretizations used in this study. Mesh refinement has been performed with the criteria that upon each refinement the size of the smallest element near the front and rear stagnation points of the sphere is reduced by an order of magnitude (see tables 5.1 for details).

The boundary conditions are the standard no slip boundary condition ( $u_z = u_r = 0$ ) along the wall, symmetry boundary condition ( $u_z = 0, \partial u_z / \partial r = 0$ ) along the centerline ( $r = 0$ ). Fully developed unidirectional velocity profile and stresses are enforced at the entrance and exit. The reference value for  $P$  is also set to zero at the exit.

Variable	3022 elements	7577 elements	18898 elements
DOF: $\vec{u}$	40,535	100,443	232,678
DOF: $\underline{\underline{G}} \& \underline{\underline{\tau}}$	25,288	62,344	144,128
DOF: $\vec{Q}$ ; $N_f = 960$	28,657,626	177,142,683	1,021,399,104
Aspect ratio of smallest element	0.01	0.001	0.0001

**Table 5.1:** Degrees of freedom (DOF) for each variable and the ratio of the width of the smallest element of each mesh to the sphere radius.

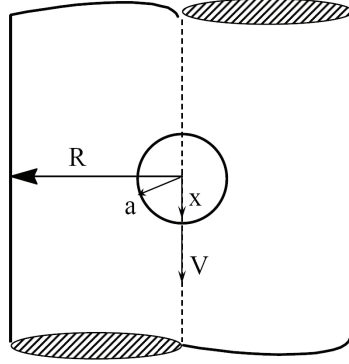


**Figure 5.1:** Schematic of the sedimentation of a sphere in a tube;  $\chi = a/R$ .

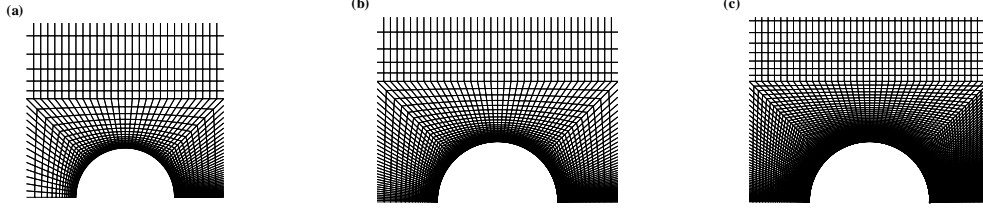


**Figure 5.2:** The computational domain near the surface of the sphere for meshes with 3022 elements, (a), 7500 elements (b) and 18898 elements, (c).

### 5.3 Fluid Rheology

Figure 5.3 depicts the experimentally measured steady shear viscosity ( $\eta$ ) and first normal stress coefficient ( $\psi_1$ ) as a function of the shear rate ( $\dot{\gamma}$ ). The test fluid which is a Boger fluid composed of 0.21 wt.% polyisobutylene (PIB), 4.83 wt.% tetradecane (C14), and 94.86 wt.% polybutene (PB), has a zero shear rate viscosity of  $\eta_0 = 13.76 Pa.s$  and a solvent viscosity of  $\eta_s = 8.12 Pa.s$ . The zero shear rate first normal stress coefficient  $\psi_{1,0} = 8.96 pa.s^2$ . The ratio of the solvent viscosity to fluid zero shear viscosity defined as  $\beta = \eta_s/\eta_0 = 0.59$  [Arigo et al. (1995)].

In addition, the small amplitude oscillatory shear flow properties of this fluid, i.e., the dynamic viscosity ( $\eta'$ ) and rigidity ( $\eta''/\omega$ ) versus the frequency of oscillation ( $\omega$ ), as well as its transient extensional viscosity ( $\eta^E$ ), at various strain rates ( $\dot{\epsilon}$ ) [Arigo et al. (1995)] are also shown in Figure 5.3. Various models, namely, FENE bead-spring chain, FENE dumbbell, and the FENE-P closed form constitutive equation have been used to describe the rheological behavior of the test fluid. Linear viscoelastic fits for  $\eta'$  and  $\eta''/\omega$  demonstrate that three modes are required to quantitatively describe the small amplitude oscillatory shear flow behavior of the polymer molecules (see table 5.2). The mean relaxation time of the polymer molecule ( $\lambda_m$ ) based on these three modes is found to be 0.7925 s.

To determine the model time constant,  $\lambda_H$ , for the FENE dumbbell and the FENE-P constitutive equation a standard technique, namely matching of the mean relaxation time of the solution,  $\lambda_m$ , to the characteristic zero shear relaxation time ( $\psi_{10}/2\eta_{p0}$ ) of the model has been adopted [Somasi et al. (2002)]. In the case of the FENE bead-spring chains,  $\lambda_H$ , has been evaluated using the following expression [Wiest and Tanner (1989)]

$$\lambda_H = \frac{\lambda_m}{d}, d = \left( \frac{b+7}{15N} \right) \left( \frac{1}{b/N+5} \right) \left( (2(N+1)^2+7) - \frac{12((N+1)^2+1)}{(N+1)(b/N+7)} \right) \quad (5.1)$$

In the above expression,  $N$  is the number of segments in the chain and  $b$  is the maximum chain or dumbbell extensibility.  $b$  of the FENE models has been selected based on two criteria, firstly to reproduce closely the steady shear and the transient extensional rheology of the fluid and secondly to be in the range of the molecular estimates for the maximum extensibility of the specific PB used in the test fluid ( $b \approx 5000 - 10000$  [McKinley et al. (1993)]). However, it should be noted that as the predictions of the steady shear and the transient extensional rheology of the test fluid do not significantly change for  $4000 < b < 10000$ , hence,  $b = 4000$  has been chosen to facilitate computational expenses of capturing steep stress boundary layers associated with very high  $b$  values in the wake of the sphere.

In case of the multi-mode FENE model,  $b = 4000$  was assigned to the mode with the longest relaxation time and other  $b$ 's were chosen to optimize the fit of the transient extensional rheology of the test fluid, i.e.  $b = 10$  and  $b = 100$ . We have also performed calculations with single mode FENE dumbbell model with  $b = 10$  and  $b = 100$  for comparison with the multi-mode description.

It should be noted that the rheological predictions of the FENE based models have been obtained via Brownian dynamics simulations using a semi-implicit predictor-corrector scheme [Somasi et al. (2002); Koppol et al. (2007, 2009)] with the ensemble size  $N_t = 960$ , while those of the FENE-P closed form constitutive model has been

obtained using the Newton-Raphson scheme described in detail in our earlier studies [Yang and Khomami (1999); Li et al. (1998, 2000); Talwar et al. (1994); Talwar and Khomami (1992)].

b	$\eta_i$ (Pa.s)	$\lambda_i$ (s)
10	3.5315	0.1
100	1.1084	1.1520
4000	1.0002	2.8395
$\lambda_m =$	$\sum_{i=1}^2 \eta_i \lambda_i / \sum_{i=1}^2 \eta_i =$	$0.7925s$

**Table 5.2:** Linear viscoelastic properties of the Boger fluid composed of 0.21 wt.% polyisobutylene (PIB), 4.83 wt.% tetradecane (C14), and 94.86 wt.% polybutene (PB).

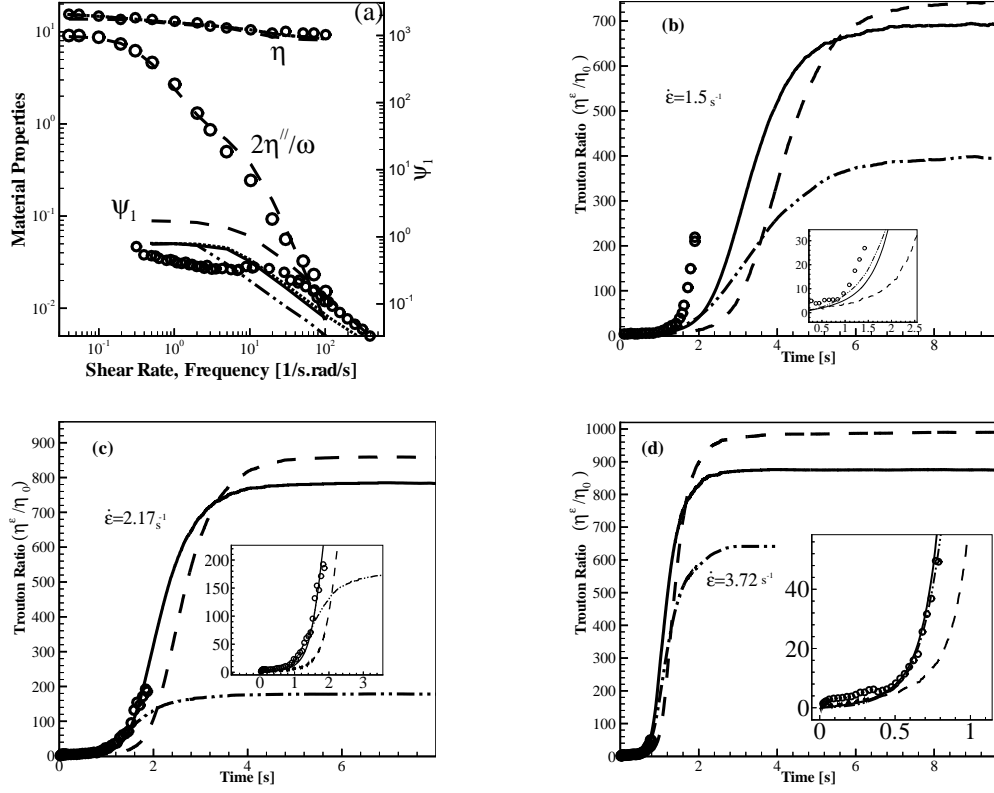


**Figure 5.3:** The fluid rheology of the Boger fluid composed of 0.21 wt.% polyisobutylene (PIB), 4.83 wt.% tetradecane (C14), and 94.86 wt.% polybutene (PB) at  $25^\circ\text{C}$  including (a)  $\eta$  vs  $\dot{\gamma}$ ,  $\psi_1$  vs  $\dot{\gamma}$ ,  $\eta'$  vs  $\omega$ , and  $\eta''/\omega$  vs  $\omega$ , (b)  $\eta^E/\eta_0$  vs  $\epsilon$  at  $\dot{\epsilon} = 1.53 \text{ s}^{-1}$ , (c)  $\eta^E/\eta_0$  vs  $\epsilon$  at  $\dot{\epsilon} = 2.17 \text{ s}^{-1}$  and (d)  $\eta^E/\eta_0$  vs  $\epsilon$  at  $\dot{\epsilon} = 3.72 \text{ s}^{-1}$ . Black circles represent the experimental results and solid, dashed and dashed-dotted lines represent the 3-segment FENE bead spring chain ( $b=4000$ ), Multi-mode FENE dumbbells and the FENE dumbbell ( $b=100$ ) respectively.

## 5.4 Results and discussion

### 5.4.1 Solution accuracy

The smallest domain discretization used in this study contains 3022 elements. This level of discretization has been previously shown to provide converged solutions up to  $We \approx 2$  at  $\chi = 0.121$  and  $\chi = 0.243$  in continuum level simulation with the FENE-P constitutive equation with  $b$ 's in the range of 10 to 900 [Yang and Khomami (1999)]. Hence, The self-consistent multiscale simulations have been performed in three different meshes with 3022, 7577 and 18898 elements respectively and all the reported results are based on the most refined mesh. Comparisons with different discretization levels are based on the  $\tau_{pzz}$  component of the polymeric stress because it exhibits large variation with  $We$  along the surface of the sphere and near the wake stagnation point, and it greatly influences the total drag on the sphere [Arigo et al. (1995); Harlen et al. (1990); Baaijens et al. (1994, 1995)]. To demonstrate the accuracy of multiscale simulations, the self-consistently computed stress profiles with the 18898 elements mesh have been compared with those obtained based on a combined Lagrangian/Brownian Dynamics (BD) technique. This approach for establishing the solution accuracy has been adopted since the conventional way of comparing solutions from multiple meshes is highly computationally intensive in the case of multiscale simulations, which is evident from the large number of degrees of freedom at each time step reported in table 5.1.

Similar to our earlier studies [Koppol et al. (2009)] the Lagrangian determination of the stress involves two steps. First, particle paths are determined via integration of the local self-consistent velocity vector ( $\vec{u}$ ) using the fourth-order Runge-Kutta method. In turn, for the FENE model the BD simulations are conducted along selected streamlines utilizing the semi-implicit predictor scheme of Somasi et al. (2002) with the ensemble size  $N_t = 1024$ . The integrations are carried out by varying  $\delta t$  such that the magnitude of  $\vec{u}\delta t$  is fixed to a constant. Specifically, the constant is set to

$A$  when  $z \in [20, 40]$ ,  $5A$  when  $z \in [10, 20]$  and  $[40, 50]$ , and  $25A$  when  $z \in [0, 10]$  and  $[50, 60]$ . With  $A \approx 1 \times 10^{-4}$ , converged results in the  $We$  range of interest are obtained. At this level of refinement, highly spatially resolved polymer stresses are obtained. Hence, the computed stresses utilizing this Lagrangian/BD procedure should provide a stringent test of the self-consistent computed stresses.

Figures 5.4 depict comparison of prototypical steady state  $\tau_{pzz}$  profiles along streamlines near the centerline of the tube in the vicinity of the sphere calculated using the mesh with 18898 elements, with finite chain extensibility,  $b = 4000$ . Overall, the excellent agreement between the self-consistent simulations and the Lagrangian-based results clearly demonstrate the accuracy of the self-consistent multiscale simulation results.

#### 5.4.2 Comparison of computed and experimentally measured drag correction factor

Consistent with prior experimental findings, in this study the drag correction factor  $K$  is defined such that the steady state drag force on the sphere is given by

$$F_D = 6\pi\eta_0 a U_s K \quad (5.2)$$

where the drag correction factor  $K \equiv K(We, \chi)$ . In the limit of  $We \rightarrow 0$ ,  $K$  can be described by the well-known Faxen correction  $K_N(\chi)$  for creeping motion of a sphere through a Newtonian liquid [Happel and Brenner (1973)]:

$$K_N(\chi) \equiv \frac{1}{1 - f(\chi)} \quad (5.3)$$

with

$$f(\chi) = [2.10444(\chi) - 2.08877(\chi)^3 + 0.94813(\chi)^5 + 1.372(\chi)^6 - \dots] \quad (5.4)$$

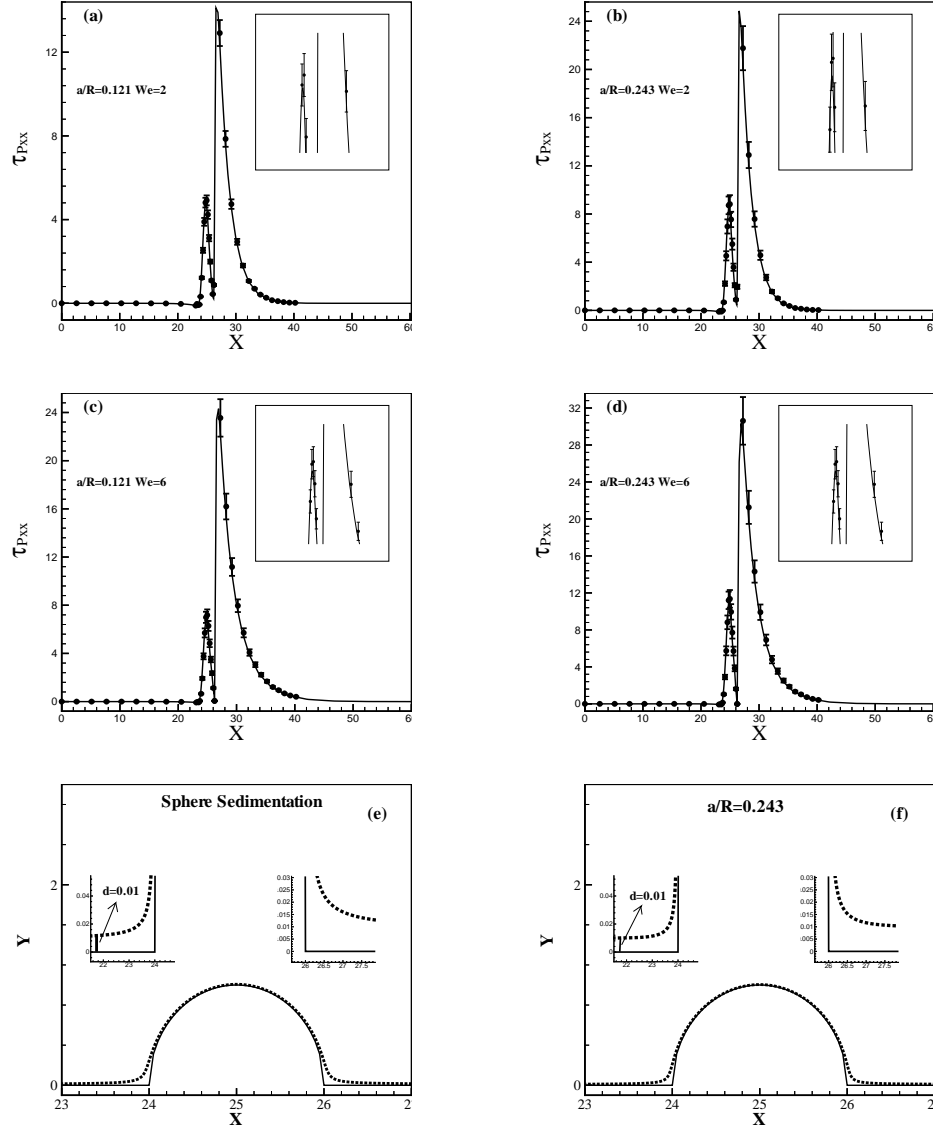


**Figure 5.4:** Comparison of prototypical steady state  $\tau_{p_{zz}}$  profiles for FENE model predicted using self-consistent simulations, solid line, Lagrangian-based integration, circles, near streamlines shown in (e) and (f) along the surface of the sphere.

For  $(\chi) = 0.243$  one obtains  $K_N = 1.932$  and for  $(\chi) = 0.121$ ,  $K_N = 1.335$  [Happel and Brenner (1973); Arigo et al. (1995)]. These results are in good agreement with our simulated drag correction factors. Hence, they have been used to compute the normalized drag correction factor  $K/K_N$  where  $K$  is the computed drag correction factor. Care must be taken in comparing the results of numerical calculations with the experimentally measured values [Arigo et al. (1995)]. In purely experimental or purely numerical studies, the data are usually reduced to a plot of the drag correction factor  $K(We, \chi)$  vs. Weissenberg number,  $We$ . However as noted by Arigo et al. (1995) such a presentation is not very helpful when one is interested in comparing the experimental steady settling velocity of a sphere of given density through a viscoelastic fluid of known properties with steady state numerical simulation since the unknown velocity appears in both the abscissa and the ordinate. In the experiments, spheres of varying densities are dropped in the fluid and the terminal velocity of the sphere is established when the reduced weight of the sphere ( $F_w$ ) is exactly balanced by the drag force ( $F_D$ ) exerted by the fluid. By contrast, in the simulations, the steady terminal velocity of the sphere and the relaxation time of the fluid (and hence the  $We$ ) are specified a priori, and the force exerted by the fluid on the sphere in steady motion is calculated. Since this force must be balanced by the weight of the sphere, numerical calculations implicitly determine the density of the settling sphere required to attain a given  $We$ . The nonlinear variation in the drag correction factor with respect to the aspect ratio and Weissenberg number preclude simple interconversion between the two approaches. To resolve this issue, following earlier studies [Arigo et al. (1995)], we have defined the dimensionless effective weight of the sphere in the experiment as  $2a(\rho_s - \rho_f)g\lambda/9\eta_0$  which is equivalent to  $We \times K(We, \chi)$  in the simulation. In turn, the flow properties computed in numerical simulations are compared with the experimental measurements at the  $We^*$  which gives the same value of the product  $We^* \times K(We^*, \chi)$  as the experiment, i.e.,  $We_{exp} \times K_{exp}(We, \chi)$ . In our calculations, the calculated and measured dimensionless weight match at multiple  $We$  where the difference between  $We^*$  and  $We_{exp}$  is less than 1%. Therefore we are confident that

a direct comparison of drag correction factor between our numerical predictions and experimental results can be performed.

As mentioned earlier, prior studies [Lunsmann et al. (1993); Satrape and Crochet (1994); Arigo et al. (1995); Rasmussen and Hassager (1996); Yang and Khomami (1999); McKinley (2001)] have shown that simulations of a sphere sedimenting in a viscoelastic fluid with closed form constitutive equations, for example the FENE-P model, are limited to  $We < 3.0$  for highly strain hardening fluids and even in the range where converged numerical solutions can be obtained the predicted drag on the sphere as a function of  $We$  and  $\chi$  are at best qualitative [Yang and Khomami (1999); McKinley (2001)]. In a recent study [Abedijaberi and Khomami (2011)] the deficiencies of closed form constitutive equations in providing realistic macroscopic flow properties predictions in flows past bluff objects has been thoroughly investigated and it has been shown that extremely large stress gradients along the plane of symmetry in the wake of the sphere observed in FENE-P based computations leads to breakdown of numerical simulations at  $We \approx 1$  for significantly strain hardening fluids, i.e.  $b > 300$ . Consequently, in earlier studies aimed at simulating the aforementioned experiments, unphysically low values of  $b$  (not consistent with the molecular parameters of PB used in the test fluid) were used in order to obtain converged results in a region where significant drag enhancement in the experiments was observed. Hence, the simulations were unable to capture the drag enhancement quantitatively. In this study for the first time we have computed the drag on the sphere at high  $We$  with  $b$  values that are consistent with molecular parameters of the macromolecule used in the test fluid [McKinley et al. (1993)]. To do so we have used the FENE model in appropriately refined meshes where the mesh is refined near both stagnation points of the sphere. Specifically, beside the commonly observed steep stress boundary layer for highly strain hardening fluids near the rear stagnation point which forms at  $We \approx 1$ , one also observes a stress boundary layer close to the front stagnation point at  $We \approx 3$  for  $b = 4000$  which needs to be resolved or it would lead

to breakdown of numerical simulation irrespective of how refined the mesh is near the rear stagnation point.

The normalized drag correction factor predicted by FENE dumbbell model as well as the experimentally measured values [Arigo et al. (1995)] are plotted as a function of the  $We$  in figures 5.5 and 5.6 for  $\chi = 0.121$  and  $\chi = 0.243$  respectively. The drag correction factor for  $b = 10$ , decreases monotonically while for  $b = 100$  and  $b = 4000$ , FENE dumbbell model predicts a slight decrease followed by monotonic increase in drag correction factor. This difference in the trend in the computed drag correction factor vs  $We$  for small and large  $b$  values is consistent with earlier studies [Yang and Khomami (1999); McKinley (2001)]. However, as can be seen in figures 5.5 and 5.6, the FENE dumbbell model with the appropriate finite extensibility ( $b = 4000$ ) that can faithfully capture the experimentally measured  $\eta^E$  at high strain rates, provide a good prediction of the drag on the sphere at higher  $We$ .

Although the FENE dumbbell model with small  $b$  can predict the small decrease observed in experimental measurements of drag correction factor at small  $We$  it fails to predict the significant increase in the drag at high  $We$ , while simulations with large  $b$  show the opposite trend. To this end we have performed simulations with a three modes model (see table 5.2 for more details). The results of these multi-mode FENE dumbbell simulations are also shown in figures 5.5 and 5.6. Clearly, the drag correction factor predicted by the multi-mode FENE dumbbell model using the parameters given in table 5.2, increases monotonically as a function of  $We$ , for both  $\chi$ 's. In fact, the predicted drag is significantly higher than both the experimentally measured values and computations based on a single dumbbell model. To elucidate the physical underpinning of this observation, we have plotted the probability density function (PDF) of polymer molecules end-to-end distance predicted by single and multi-mode FENE model using different  $b$  values at the point of maximum stress downstream of the rear stagnation point. As can be seen in figures 5.7 and 5.8 smaller polymer molecules get stretched at lower  $We$ . Specifically, in a single mode calculation with  $b = 10$ , the molecules are already stretched at  $We \approx 0.5$  while at  $b = 100$  and

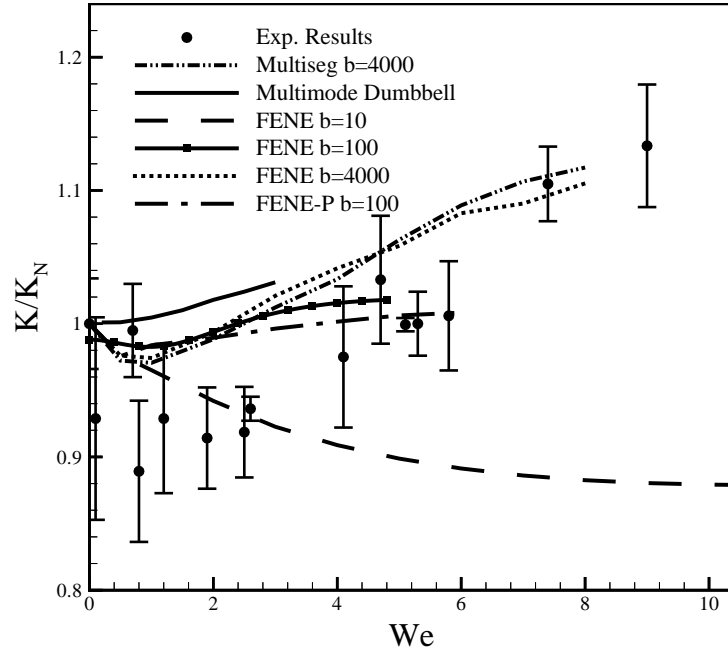


**Figure 5.5:** Comparison of the experimentally obtained steady state normalized drag coefficient correction factor with the corresponding values obtained from FENE and FENE-P calculations at  $\chi = 0.121$ .

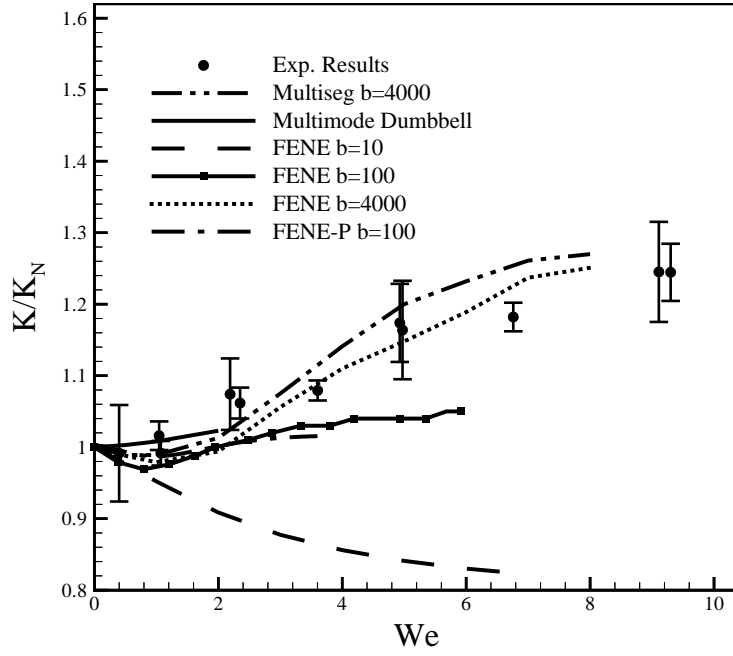


**Figure 5.6:** Comparison of the experimentally obtained steady state normalized drag coefficient correction factor with the corresponding values obtained from FENE and FENE-P calculations at  $\chi = 0.243$ .

$b = 4000$  the molecules are near their equilibrium configuration for  $We \leq 1$ . On the other hand, due to the way that  $We_{mean} = U\lambda_{mean}/a$  is defined in the multi-mode calculations (see table 5.2) , the polymer molecules of the modes with  $\lambda_i/\lambda_{mean} > 1$  experience  $We_{eff}$  which is larger than  $We_{mean}$  and consequently get fully stretched at lower  $We_{mean}$  compared to single mode calculations. Consequently, even at small  $We$  the mode with the longest relaxation time dominates the contribution of various modes to the polymeric stresses, hence, the system effectively behaves as a single dumbbell with  $b = 4000$  and  $\lambda = 2.84$ . In fact the drag correction factor predicted with a dumbbell model with  $b = 4000$  is reproduced closely by shifting the multi-mode calculation results with a factor of  $2.84/0.7925$ . To this end, the PDF of polymer molecules of each mode in a multi-mode calculation is compared with single mode calculation with the same  $b$  (see figure 5.9). The comparison is done at  $We_{mean}$  where the  $We_{eff}$  the polymer molecules are experiencing is close to  $We$  of single mode calculations. The similarity between the PDFs clearly suggest that different modes more or less function independently of each other in the multi-mode simulations. Based on the above discussions it is not surprising that multi mode FENE dumbbell model predictions over predict the experimentally measured drag at both  $\chi$ s. This is due to the fact that in strong straining flows the coupling of polymer dynamics with momentum equations does not give rise to significant mode-mode interaction through modifications of the flow kinematics. This observation has motivated examination of micromechanical models that allow implicit mode-mode coupling. The simplest model with these features is the bead-spring chain model composed of  $N$  beads and  $N-1$  springs obeying the FENE force law. Specifically, the use of this model allows both configurational diversity and mode-mode coupling that has been shown to be essential in quantitatively describing macromolecular dynamics in simple kinematics flows [Doyle et al. (1998); Shaqfeh (2005); Larson (2005)].

The normalized drag correction factor predicted by three segment FENE bead-spring chain model as a function of  $We$  and  $\chi$  are also shown in figures 5.5 and 5.6. Overall, the predicted drag at high  $We$  is slightly higher than the single segment

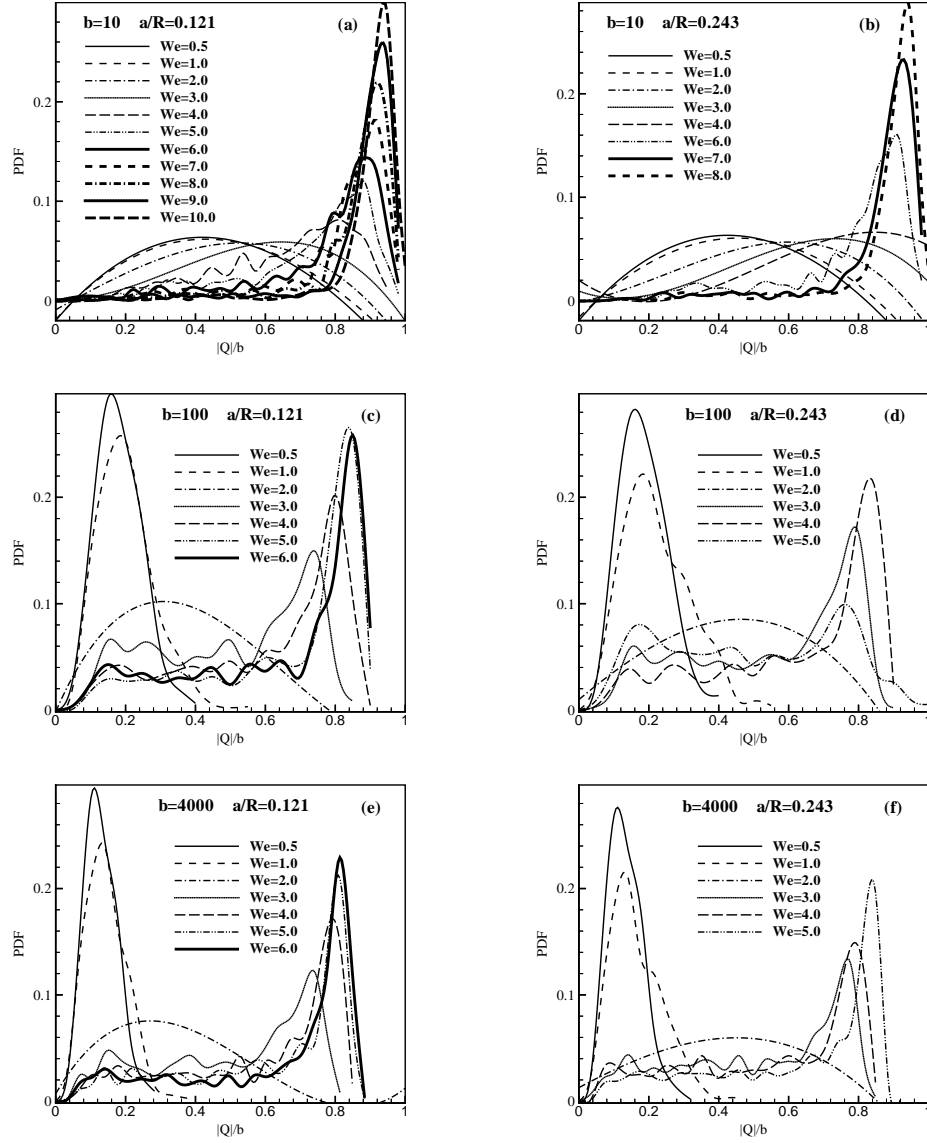


**Figure 5.7:** Probability density function (PDF) of nondimensionalized end-to-end distance  $|\vec{Q}|/b$  at the point of maximum stress near the rear stagnation point of sphere predicted by single mode FENE dumbbell model.

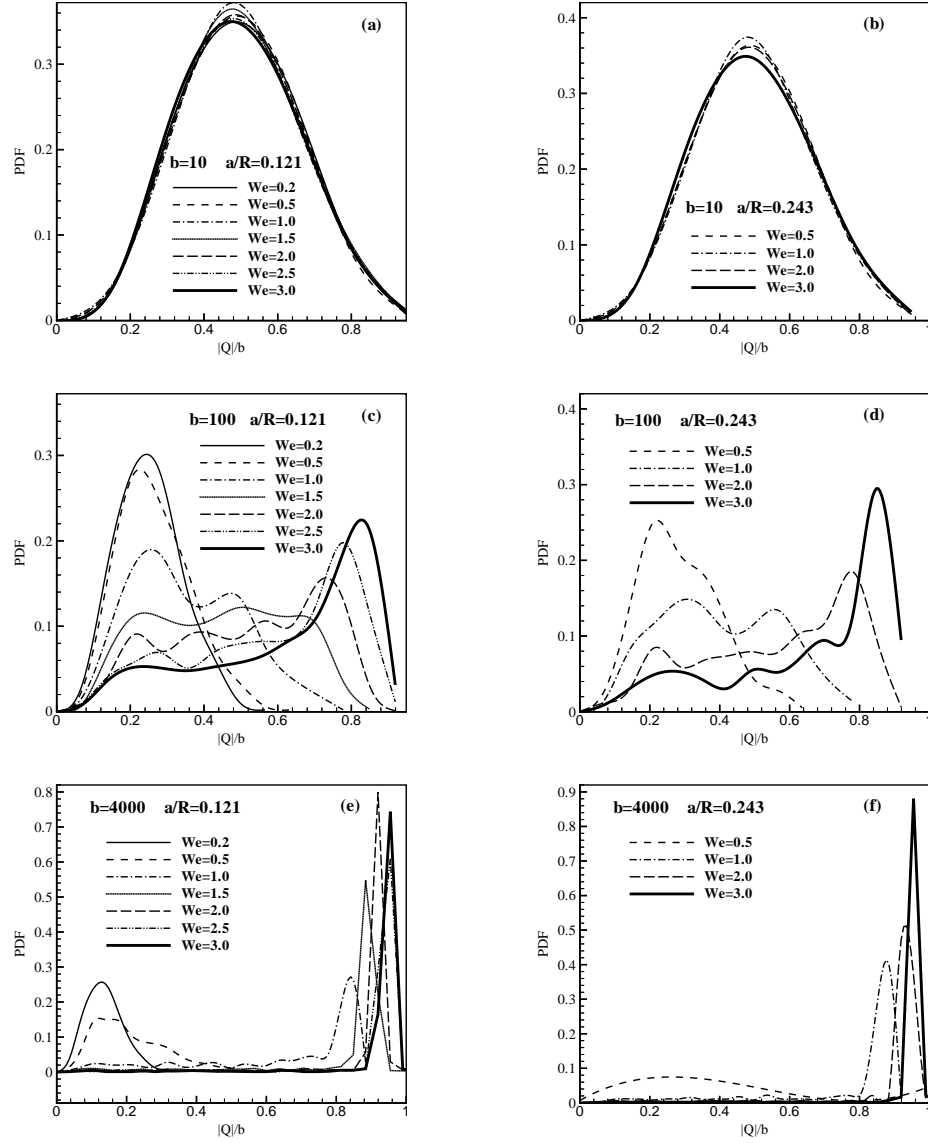


**Figure 5.8:** Probability density function (PDF) of nondimensionalized end-to-end distance  $|\vec{Q}|/b$  at the point of maximum stress near the rear stagnation point of sphere predicted by multi-mode FENE dumbbell model.

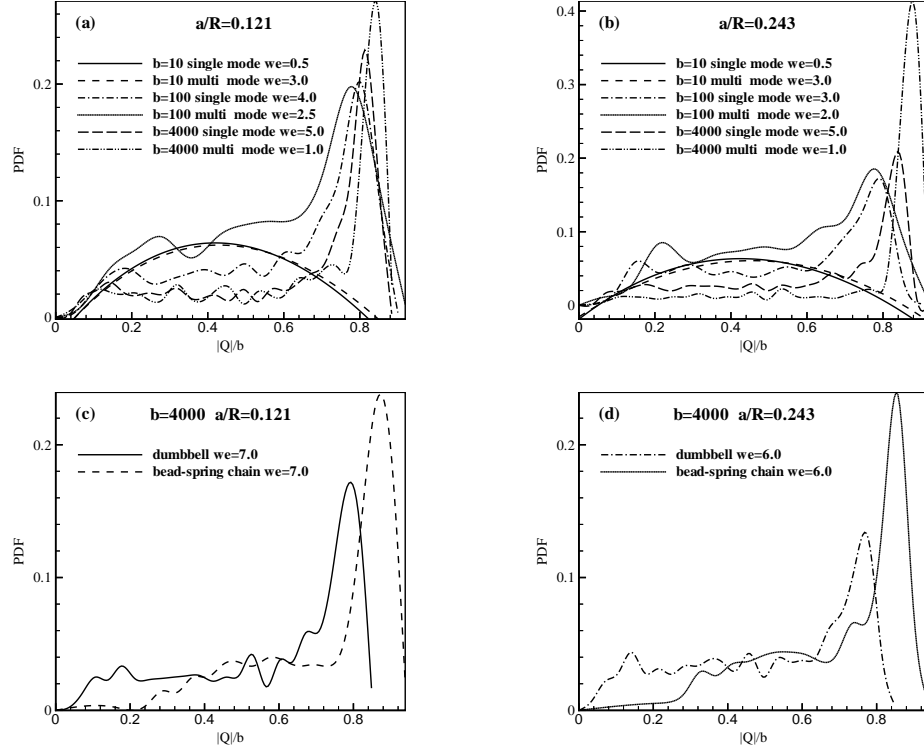


**Figure 5.9:** Probability density function (PDF) of nondimensionalized end-to-end distance  $|\vec{Q}|/b$  at the point of maximum stress near the rear stagnation point of sphere predicted by FENE model.

model and somewhat larger at lower  $We$ , (more aligned with the experimental measurements). To more closely examine the differences between the predictions of the single segment dumbbell and the multi-segment chain models, the PDF of the end-to-end distance for both models is shown in figure 5.9. Clearly, the polymer molecules near the rear stagnation point of the sphere described by FENE bead-spring chain model get more stretched as compared to the FENE dumbbell model, which clearly suggests the existence of distinct flow microstructure coupling at different level of Coarse graining (see figure 5.9). This intricate coupling also influence the total traction on the sphere and its components, i.e. purely elastic and viscous stresses as well as the pressure. Hence, the total traction along the surface of the sphere shows significant localization near the rear stagnation point (see figures 5.10 and 5.11). Consequently, the effect of distinct flow microstructure couplings predicted by various FENE dumbbell and chain models on the drag is mainly limited to the region near the rear stagnation point of the sphere. Since the drag is obtained by integration of the traction over the entire surface of the sphere, this measure cannot accurately capture the overall effect of fluid elasticity on the flow dynamics predicted by the FENE dumbbell and three-segment chain models. However, as it will be shown later, the aforementioned flow microstructure coupling has a very significant effect on the wake structure formed downstream of the rear stagnation point.

In order to better understand the mechanism of the drag enhancement we have examined the contribution of purely elastic and viscous stresses as well as the pressure to the computed drag [Yang and Khomami (1999)]. Overall, elastic effects tend to give rise to a reduction in the drag coefficient while viscous effects give rise to an increase in the drag coefficient. However, the trend in the variation of drag coefficient as a function of  $We$  more or less follows the variations observed in the pressure contribution to the drag, particularly at high  $We$ . This clearly indicate that the pressure particularly near the rear stagnation point is the dominant factor in determining the overall drag on the sphere at high  $We$  (see figures 5.10-(d) and 5.11-(d)).

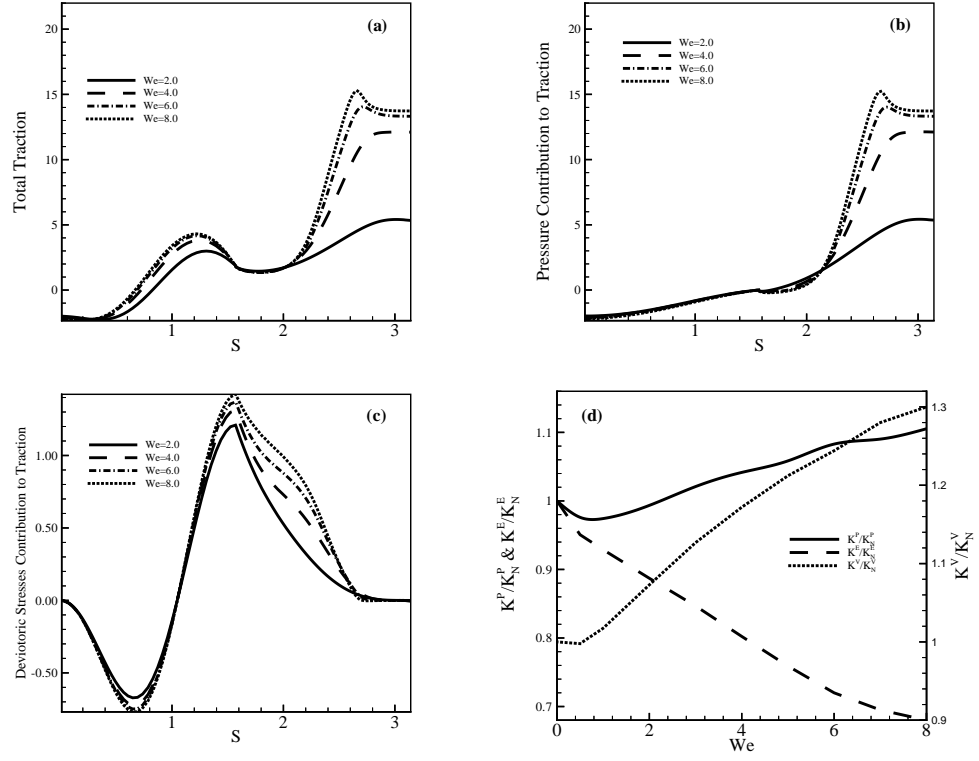


**Figure 5.10:** The contribution of purely elastic and viscous stresses as well as the pressure to the traction on the surface of the sphere (a,b,c) and total drag on the sphere (d) at  $\chi = 0.121$ .

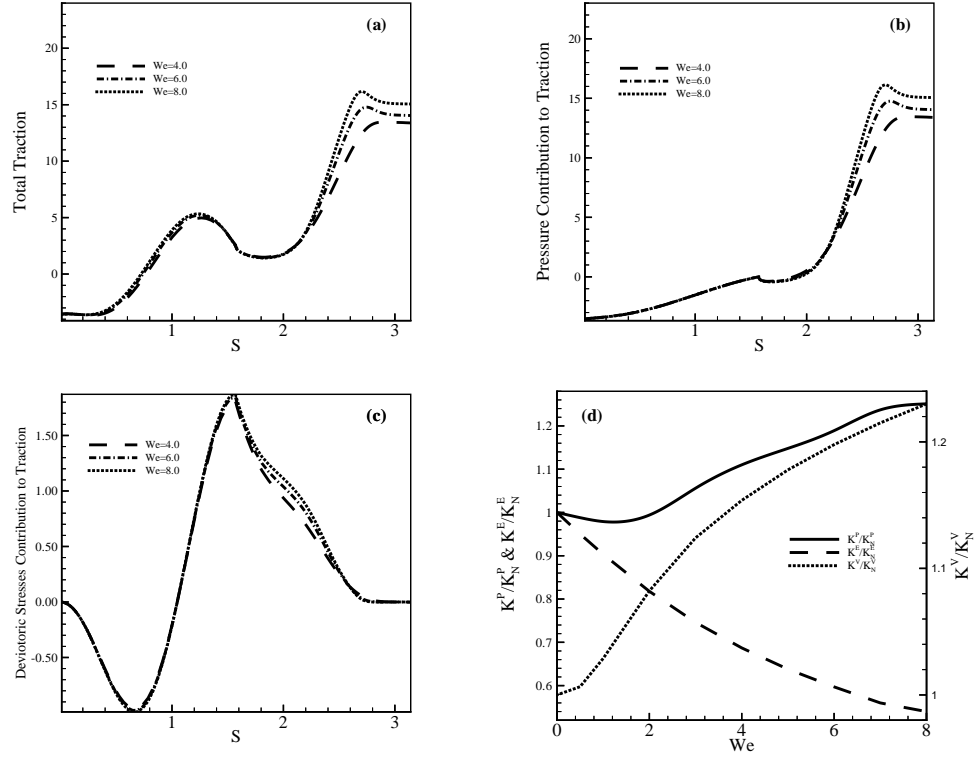


**Figure 5.11:** The contribution of purely elastic and viscous stresses as well as the pressure to the traction on the surface of the sphere (a,b,c) and total drag on the sphere (d) at  $\chi = 0.243$ .

### 5.4.3 Elastic Effects on the Structure of the Wake

In addition to an integrated property such as the drag on the sphere which has been shown not to be a very sensitive measure of elastic effects on the overall flow [McKinley (2001)], a number of studies have investigated the influence of flow elasticity on the velocity and stresses in the wake of bluff objects. Specifically, experiments show that the axial extent of this elastic wake depends on both  $We$  and  $\chi$  and decays slowly over a distance of 30 radii for the highest reported  $We$ , i.e.  $We = 9.092$  for  $\chi = 0.243$  and  $We = 7.557$  for  $\chi = 0.121$  [Arigo et al. (1995); McKinley (2001)]. It has also been shown that continuum calculations with dumbbell based models can capture qualitatively the wake structure but the predicted effect is much more localized (2-3 radii) in comparison with experimental observations [Arigo et al. (1995); McKinley (2001)].

In figure 5.12 the axial centerline velocity upstream and downstream of the spheres calculated by FENE dumbbell and chain models is depicted for both  $\chi$ 's. As expected at low  $We$  the velocity field in the downstream wake of the sphere is fore/aft symmetric with the velocity measured in the quiescent fluid upstream of the sphere and as strain rates in the fluid increase at higher  $We$ , the velocity field progressively loses its fore/aft symmetry and a viscoelastic wake develops. The FENE chain model predicts a slower decay than the dumbbell model. Specifically the distances predicted by FENE dumbbell and chain models for the velocity to decay to its equilibrium value is approximately 15 & 25 and 8 & 15 for  $\chi = 0.121$  and  $\chi = 0.243$  at  $We = 8.0$ , respectively. The superior predictions of the chain models can be rationalized by its more accurate description of the macromolecular dynamics in the fast transient extensional flows in the wake of the sphere. This in turn, leads to a more accurate description of the polymer body force that gives rise to the extended velocity wake.

Birefringence measurements can also be used to study elastic effects on the wake structure behind bluff objects. In fact, presence of high level of molecular orientations in the wake of a cylinder confined in a channel up to 10 radii downstream of the

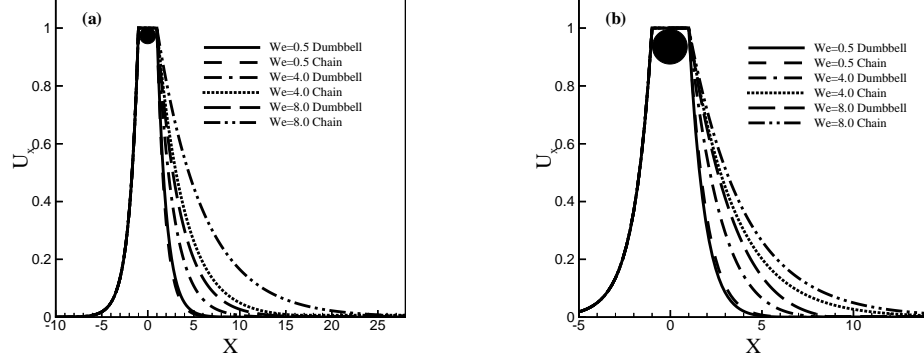


**Figure 5.12:** Predicted velocity along the centerline of the tube and surface of sphere at (a)  $\chi = 0.121$  and (b)  $\chi = 0.243$ ;  $b = 4000$ .

cylinder have been observed for polymeric solutions at  $We \approx 2$  [Baaijens et al. (1995)]. To examine the extent of the birefringent strand in the sedimenting sphere problem, we have examined the stress contours in the wake of the sphere (see figure 5.13). Clearly, the bead-spring chain FENE model predicts strands which extend dramatically with increasing  $We$  at both  $\chi$ 's and even reaches the end of computational domain ,i.e., 60 radii, for  $We > 8$ .

It should be noted that even though the distance from the sphere where the velocity decay to its equilibrium value predicted by the 3 segment bead-spring model is significantly larger than that predicted by continuum constitutive equations or the mesoscale dumbbell model, it still is somewhat smaller than the experimentally measured value. However, our simulations clearly suggest that a better description of the experimental data can be obtained with chain models with larger number of segments. Considering the computational requirements of such simulations, the use of more sophisticated Coarse grained models such as the configuration based Coarse grained model [Venkataramani et al. (2008a)] should also be considered.

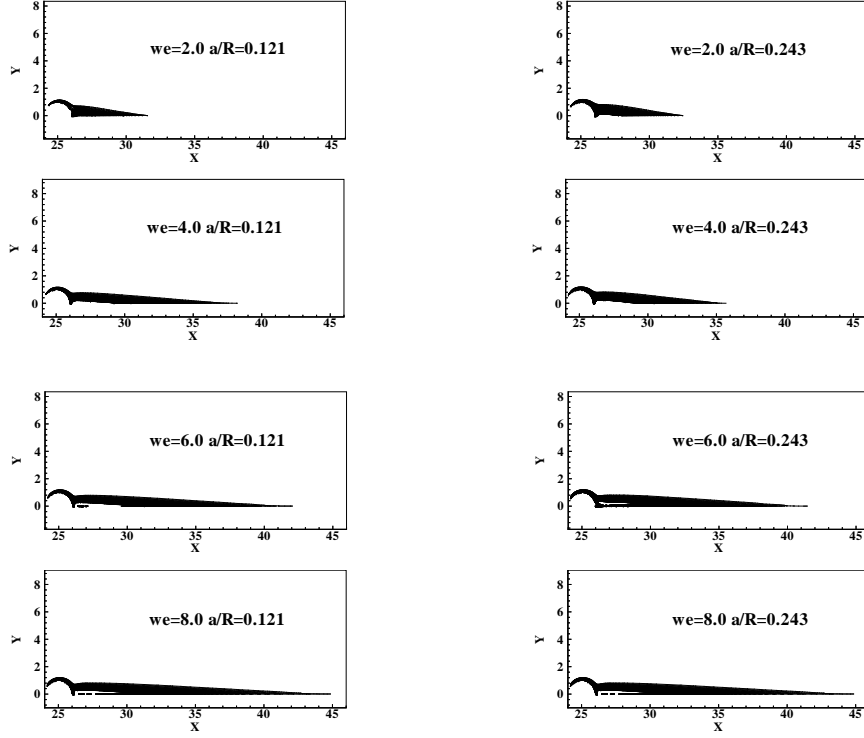


**Figure 5.13:** Stress contour plots in the wake of the sedimenting sphere (multi-segment bead spring FENE model with ( $b = 4000$ )). To facilitate the comparison all the results are plotted at the same range and number of contour levels, i.e. 50 levels in 1-10 range.

## 5.5 Conclusion

Self-consistent multiscale flow simulations of a highly elastic dilute polymeric solution, described by first principles micromechanical models for sedimentation of a sphere in a tube filled with a dilute polymeric solution has been investigated. Through comparisons with experimental measurements, we have demonstrated that the evolution of the drag coefficient as a function of fluid elasticity can be accurately predicted when the macromolecular dynamics is described by realistic micromechanical models that closely capture the transient extensional viscosity of the experimental fluid at high extension rates. Specifically, for the first time we have computed the drag coefficient on the sphere at high  $We$  utilizing multi-segment bead-spring chain models with appropriate molecular parameters and have demonstrated that hi-fidelity multiscale numerical simulations are not only capable of quantitatively describing the drag on the sphere as a function of  $We$  at various sphere to tube diameter ratios but also they can faithfully reproduce the experimentally observed velocity and the stresses in the wake of the sphere.

# Chapter 6

## A computational study of the influence of viscoelasticity on the interfacial dynamics of dip coating flow

### 6.1 Introduction

Free surface displacement flows of Newtonian and viscoelastic fluids plays an important role in several industrial applications such as polymer processing, coating technology, gas-assisted injection molding and enhanced oil recovery [Taylor (1960); Bretherton (1961); Ruschak (1985); Bonn et al. (1995); Coyle et al. (1990); Poslinski et al. (1995)]. Consequently, numerous researchers have focused their attention on modeling Newtonian displacement flows in a variety of geometries to better understand the interfacial dynamics of free surface flows [Coyle et al. (1990); Pearson (1959); Pitts and Greiller (1961); Sullivan and Middleman (1979); Rabaud et al. (1990); Saffman and Taylor (1958)]. However, the number of studies dealing with

viscoelastic displacement flows is limited [Linder et al. (2002); Huzyak and Koelling (1997); Lee et al. (2005, 2002); Bhatara et al. (2004a); Ruschak (1985)].

Turning to the literature on experimental studies of free surface displacement flows of viscoelastic fluids, we again find a relatively small body of work. Bonn [Bonn et al. (1995)] using solutions of polyethylene oxide (PEO) reported an increase in the film thickness over that found for Newtonian fluids. Lidner [Linder et al. (2002)] carried out experiments in a Hele-Shaw cell geometry and observed a film thickness increase over that found for Newtonian fluids using solutions of PEO, and a film thickness decrease using xanthane solutions. They attributed the film thickening effect for PEO to the high elongational viscosity and large normal stresses that PEO exhibits, although no clear correlations were developed as a function of the Weissenberg number,  $We$ , that provides a measure of the elasticity of the flow through the relaxation time of the polymer (i.e.,  $We = \frac{\lambda U}{b}$ , where  $\lambda$  is the relaxation time of the polymer,  $U$  is the mean fluid velocity and  $b$  is the gap separation between the plates). Huzyak [Huzyak and Koelling (1997)] reported strong film thickening effects using highly elastic, non-shear thinning, polyisobutene-polybutene (PIB-PB) based Boger fluids. Lee [Lee et al. (2005)] in a study of free surface displacement flow of PIB-PB Boger fluids under gravity stabilization in an eccentric cylinder geometry, found significant film thickening due to presence of elasticity.

Recently, a number of numerical simulation of the steady-state displacement of viscoelastic fluids by an air bubble in long narrow tubes have been performed [Bhatara et al. (2004a); Gauri and Koelling (1999a,b); Giavedoni and Saita (1997); Pasquali and Scriven (2002); Lee et al. (2002, 2005); Bhatara et al. (2005b)]. Specifically, Pasquali and Scriven [Pasquali and Scriven (2002)] examined the flow dynamics of air displacing fluid for a slot coating flow using dilute and semi-dilute polymer solutions. They observed the formation of layers of molecular stretch under the free surface downstream of the stagnation point, in the capillary transition region. Furthermore, they demonstrated that the layers of molecular stretch are largest for the extensible and semi-extensible molecules and effectively smaller for more rigid

molecules. Lee [Lee et al. (2002, 2005)], examined both the Hele-Shaw and slot coating geometries for dilute polymer solutions using the Oldroyd-B, FENE-CR and FENE-P constitutive equations. In the Capillary number regime considered in their study (i.e.,  $Ca < 1.0$ ), the flow is characterized by a recirculation pattern and elastic normal stress boundary layers in the capillary transition region at moderate values of  $We$  are observed. Furthermore, this study demonstrated that the formation of these stress boundary layers generates a strong positive normal stress gradient in the flow direction in the capillary transition region that results in film thickening. Bhatara and Lee [Bhatara et al. (2004a); Lee et al. (2002, 2005)] extended the FENE-CR simulations to a much larger range of  $Ca$  and  $We$  and also incorporated the effect of gravity. These authors identified the presence of two distinct flow regimes, (in the absence of gravity) a recirculation flow at low  $Ca$  ( $Ca < 1.0$ ) and a bypass flow at high  $Ca$  ( $Ca > 1.0$ ). In the recirculation flow, in addition to the film thickening effect, the authors observe a meniscus invasion phenomenon when the stresses in the boundary layer created by planar extensional flow near the free surface, become very large. In a separate study Romero [Romero et al. (2004)] have experimentally demonstrated that the viscoelastic nature of the fluid significantly reduces the contact angle due to meniscus invasion, leading to a non-uniform coating. In addition, Bhatara [Bhatara et al. (2004a)] demonstrated that the formation of the elastic normal stress boundary layer is a local phenomenon, largely independent of geometrical considerations. Moreover, these authors considered the effect of concentration and chain architecture on the viscoelastic displacement flow dynamics, by modeling semi-dilute, concentrated solutions and polymeric melts. In turn, they established that the interfacial dynamics depend on the extensional hardening and shear thinning characteristics of the fluid [Bhatara et al. (2005b)]. Specifically, they demonstrated that the coating film thickness is mainly governed by two forces, shear stress gradients at the wall that have a film thickening effect, and normal stress gradients in the flow direction that, if positive, have a film thickening effect [Lee et al. (2002); Bhatara et al. (2005b); Ro and Homsy (1995)].

In addition to the prototype flow problem involving air-fluid displacement in a capillary tube or in a gap between two closely spaced parallel plates i.e., the Hele-Shaw cell flow, the dip coating problem [White and Tallmadge (1965); Spiers et al. (1975); Adachi et al. (1978)], in which a thin liquid film is formed on a flat plate drawn vertically at a constant speed from a liquid bath (see 6.1-(a) ) is also a classic problem in free surface displacement flows. The withdrawal of a Newtonian fluid under dominant capillary forces was considered by Landau and Levich [Landau and Levich (1942)] in their pioneering work. In the case where the effect of viscous forces is negligible in comparison to surface tension forces (i.e., low values of  $Ca$ ), the authors determined the steady state dimensional film thickness,  $t_f$  , to be,

$$t_f = 0.994 \frac{(\mu U)^{2/3}}{\sigma^{1/6}(\rho g)^{1/2}} \quad (6.1)$$

where  $\mu$  is the fluid viscosity,  $U$  is the speed of the plate,  $\sigma$  is the fluid surface tension,  $\rho$  is the fluid density and  $g$  is the acceleration due to gravity. This equation can be recast as,

$$\frac{t_f}{(\sigma/(\rho g))^{1/2}} = 0.994 Ca^{2/3} \quad (6.2)$$

An inspection of this equation indicates that the film thickness scales with  $Ca^{2/3}$ , if the film thickness is made dimensionless with a characteristic length scale  $l$ , where  $l = (\frac{\sigma}{\rho g})^{1/2}$ , i.e. the capillary length [Landau and Levich (1942)]. Other significant contributions have been made by White [White and Tallmadge (1965)], who compared the theoretical results of Landau and Levich with experimental measurements of film thickness and found good agreement at low  $Ca$ , and by Esmail [Esmail and Hummel (1975)] who included the contributions of fluid inertia.

The corresponding problem for non-Newtonian fluids, i.e., fluids with a shear dependent viscosity, has been treated by Spiers [Spiers et al. (1975)], and by Gutfinger [Gutfinger and Tallmadge (1965)]. However, inertial effects were not included, nor was fluid elasticity. Spiers [Spiers et al. (1975)] compared the results of their experiments

with the theories for the Bingham, Ellis and power-law models. However, only a small number of their experimental results were in good agreement with their theoretical predictions. Adachi [Adachi et al. (1978)] used a modified four-constant Oldroyd model to predict non-Newtonian effects on the film thickness concluded that the inclusion of viscoelasticity reduces the film thickness in comparison to predictions from purely viscous theory. Ro and Homsy [Ro and Homsy (1995)] extended their Hele-Shaw flow theory to dip coating in the weak elasticity regime, i.e.,  $We \ll Ca^{1/3} \ll 1$ . Specifically, the authors determined that the characteristic length scale in the outer region (Region III in figure 6.1-(a)) is the capillary length  $l$ , as proposed by Landau and Levich [Landau and Levich (1942)]. Furthermore, by neglecting the influence of gravity in the inner region (Region II in figure 6.1-(a)), they determined that in this weak elastic regime fluid elasticity gives rise to film thinning and obtained the following expression for the dimensionless film thickness ( $h$ ),

$$h = \frac{t_f}{l} = 0.9454Ca^{2/3} - 0.09454WeCa^{1/3} + \dots \quad (6.3)$$

Figure 6.2 shows the cross-section of the flow interface created for a fluid film as it is pulled out from a liquid bath. This problem was first analyzed by Mysels [Mysels and Frankel (1978)] for the case of flexible and inextensible soap films drawn from a bath of Newtonian soap solution. The authors regarded the pulling of the film out of the solution as a liquid entrained by two inextensible surfaces and analyzed the hydrodynamics where the velocity gradient is zero at the centerline. In effect, a fluid film, as depicted in figure 6.2, is equivalent to the film formed in dip coating (see figure 6.1-(a)) plus its mirror image, i.e., a liquid layer of twice the thickness. Hence, the solution of this problem is identical to that of the dip coating with the thickness of the pulled film being twice that of the dip coating film. Therefore, an analysis of the interfacial dynamics of the dip coating flow can be extended in a straight forward manner to examine the interfacial dynamics of inextensible fluid films pulled from a viscoelastic solution. The purpose of this study is to illustrate an approach

by which Hele-Shaw type flow simulations can be extended to simulate dip coating flows by appropriate rescaling of the governing equations in the Hele-Shaw problem formulation and increasing the  $Bo$  until the dip coating flow limit is reached.

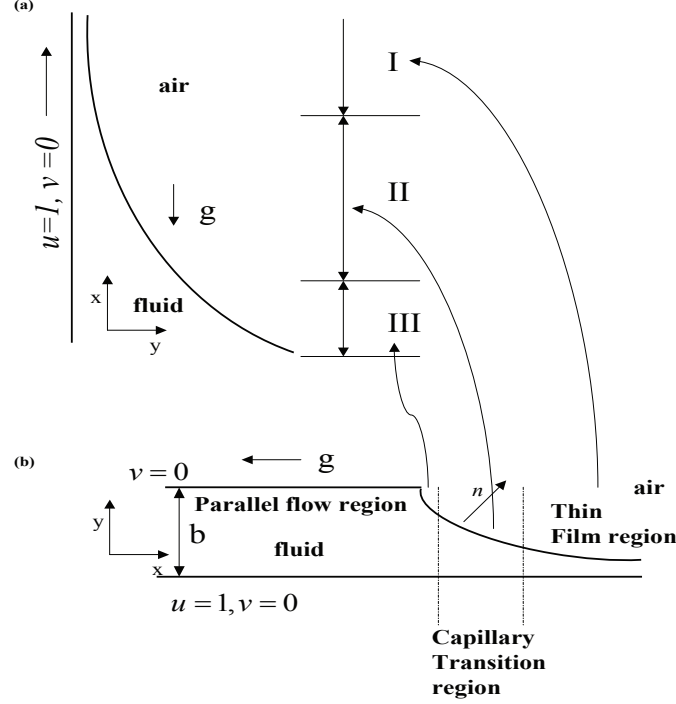


**Figure 6.1:** Problem formulation: (a) Cross-section of the flow interface created in dip coating, (b) Schematic of the Hele-Shaw flow.

## 6.2 Problem Formulation

To formulate dip coating free surface displacement flow of a single vertical plane pulled out of a liquid bath, as depicted in figure 6.2, we consider the flow between two parallel vertical plane pulled simultaneously out of a liquid at the same speed. In turn, the distance between the planes, i.e. the gap width, is progressively increased to minimize the effect of the presence of the second plane on the flow properties. In the other words, the flow near a single plane pulled out of a liquid bath, is similar to the flow between parallel planes pulled out of liquid bath in the limit of large gap width,

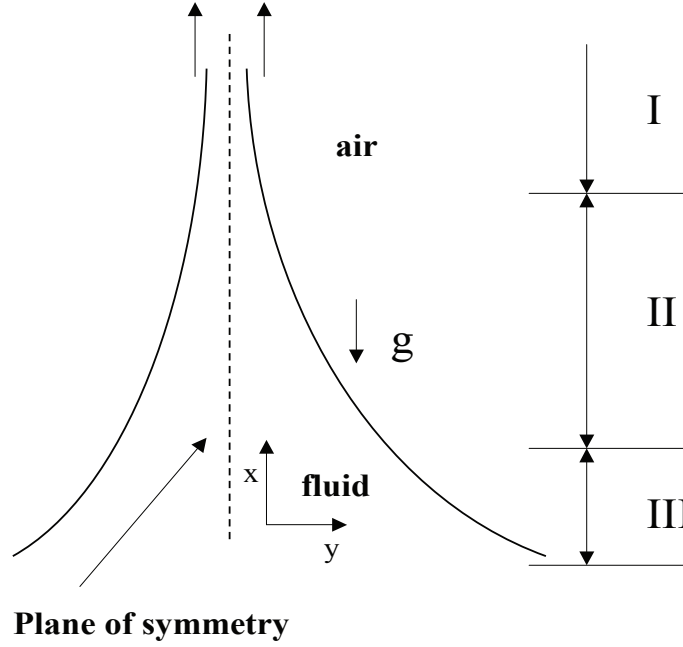


**Figure 6.2:** Cross-section of the flow interface of a soap film.

where the appropriate length scale of the problem, namely the capillary length scale becomes much smaller than the gap width. In this limit, the problem formulation for the steady free surface displacement flow represented in figure 6.1-(a) becomes identical to the problem formulation for the Hele-Shaw flow [Bhatara et al. (2004a)]. As illustrated in figure 6.1-(b), the cross-sections of the flow interface created in both the dip coating flow and the Hele-Shaw flow are similar. In both flows, a thin film region is connected to a parallel flow region by a transition region. The difference in the two problems is the direction of the gravity force in the dip coating flow as compared to the Hele Shaw flow.

In the other words one could think of dip coating problem as a Hele-Shaw problem in the limit of infinite gap width, where the relevant length scale is the capillary length ( $l$ ) instead of the half gap width ( $b$ ). Hence, the ratio of the characteristic length scales for the Hele-Shaw flow and the dip coating flow is given by the Bond number, i.e.,

$$Bo = \frac{\rho g b^2}{\sigma} = \frac{b^2}{l^2}, \quad (6.4)$$

where  $\rho$  is the fluid density,  $g$  is the acceleration due to gravity,  $b$  is the gap width and  $\sigma$  is the fluid surface tension. Therefore, in order to reach the dip coating limit, the Hele-Shaw simulations have to be performed at high values of  $Bo$ , i.e., when the gap width between the parallel planes becomes much larger than the length scale of the problem, i.e., the capillary length. To further illustrate this basic approach, a scaling analysis of the governing equations in the limit of large  $Bo$  is performed.

Specifically, the equations of continuity and motion are considered:

$$\vec{\nabla} \cdot \vec{u} = 0, \quad (6.5)$$

$$-\vec{\nabla} P + \vec{\nabla} \cdot \boldsymbol{\tau} + \rho g \vec{I}_x = 0, \quad (6.6)$$

where  $\vec{u}$  is the velocity vector,  $\vec{I}_x$  is the unit vector in the  $x$  direction, (vertical direction in figure 6.1-(a)),  $P$  is the pressure and  $\boldsymbol{\tau}$  is the total stress tensor formed by the sum of the Newtonian solvent stress,  $\boldsymbol{\tau}_s$ , and the polymer stress,  $\boldsymbol{\tau}_p$ .

In turn, the equations are non-dimensionalized as

$$(x, y) [=] (b, b), \quad (\vec{u}, \vec{v}) [=] U, \quad P [=] \frac{\sigma}{b}, \quad \boldsymbol{\tau} [=] \frac{\eta U}{b}, \quad (6.7)$$

where  $\eta$  is the total viscosity of the fluid at zero shear rate and  $U$  is the characteristic velocity of the problem.

With the gap width as the length scale, the dimensionless form of Equation 6.6 is given by,

$$-\vec{\nabla} \frac{P}{Ca} + \vec{\nabla} \cdot \boldsymbol{\tau} + \frac{Bo}{Ca} \vec{I}_x = 0, \quad (6.8)$$

Now in the limit of  $Bo \rightarrow \infty$ , i.e.  $b \rightarrow \infty$ , the last term on the left hand side of this equation becomes large, indicating that in order to recover the correct form of the equation of motion in this limit, we must rescale the problem. As mentioned earlier in this limit, the appropriate length scale is the capillary length. Specifically with the capillary length as the length scale, the dimensionless form for Equation 6.6 becomes,

$$-\vec{\nabla} \frac{P}{Ca} + \vec{\nabla} \cdot \boldsymbol{\tau} + \frac{1}{Ca} \vec{I}_x = 0, \quad (6.9)$$

This equation illustrates that choosing the appropriate length scale (i.e., scaling with the capillary length) one can model dip coating flows using Hele-Shaw simulations in the limit of large  $Bo$ .

To model the dynamics of the dilute polymeric solution, the FENE-CR [Chilcott and Rallison (1988); Bird et al. (1980)] model is used, as it provides a good description of the rheology of Boger fluids (non shear thinning, bounded extensibility) [Boger and Mackay (1991)], that have been widely used in experimental studies of viscoelastic free surface coating flows [Huzyak and Koelling (1997); Lee et al. (2002); Grillet et al. (1999a)]. Under steady flow conditions, the constitutive equation for a FENE-CR model is given by

$$\vec{u} \cdot \vec{\nabla} \boldsymbol{C} = \boldsymbol{C} \cdot \vec{\nabla} \vec{u} + \vec{\nabla} \vec{u} \cdot \boldsymbol{C} - \frac{f(R)}{We} (\boldsymbol{C} - \boldsymbol{I}), \quad (6.10)$$

where  $\boldsymbol{C}$  is the polymer conformation tensor and represents an ensemble average of the dyadic product  $\vec{R}\vec{R}$  of the dumbbell end to end vector  $\vec{R}$  and  $f(R)$  is the spring force law, given by

$$f(R) = \frac{1}{1 - \frac{Tr(\boldsymbol{C})}{L^2}}, \quad (6.11)$$

where  $L$  is the finite extensibility parameter. In the limit  $L \rightarrow \infty$ , the FENE-CR model reduces to the Oldroyd-B model. The total stress is written as the sum of the

viscous stress and the polymer stress

$$\boldsymbol{\tau} = 2S\dot{\boldsymbol{\gamma}} + \frac{(1-S)}{We}f(R)(\boldsymbol{C} - \boldsymbol{I}), \quad (6.12)$$

where  $S$  is the ratio of the solvent viscosity to the total viscosity.

### 6.2.1 Boundary Conditions

The boundary conditions applied on the free surface are the kinematics condition

$$\vec{u} \cdot \vec{n} = 0, \quad (6.13)$$

the normal stress balance

$$\vec{n} \cdot (\boldsymbol{\tau} - \boldsymbol{I}P) \cdot \vec{n} = \frac{\vec{\nabla}_s \cdot \vec{n}}{Ca}, \quad (6.14)$$

and the vanishing of shear stresses

$$\vec{n} \cdot \boldsymbol{\tau} \cdot \vec{t} = 0, \quad (6.15)$$

where  $\vec{n}$  and  $\vec{t}$  are the unit vectors normal and tangent to the free surface respectively and  $\vec{\nabla}_s$  denotes the surface divergence operator. The governing equations are solved by considering a coordinate system that moves at the same speed as the interface tip. In this reference frame, the corresponding boundary conditions are :

On the solid wall, no slip condition applies

$$u = 1, v = 0; \quad y = 0, \quad 0 \leq x \leq \infty. \quad (6.16)$$

At the centerline, symmetry conditions apply

$$\tau_{sy} = 0, v = 0; \quad y = \frac{1}{2}, \quad 0 \leq x \leq x_c \quad (6.17)$$

$$x_c, \quad \vec{u} = 0, \quad (6.18)$$

where  $x_c$  refers to the x coordinate of the interface tip.

At the outflow, a fully developed velocity profile is assumed in the thin film, i.e.,

$$\frac{\partial^2 u}{\partial y^2} = \frac{Bo}{Ca}, \quad (6.19)$$

while far from the air fluid interface the velocity profile takes on the following form [Lee et al. (2002); Reinelt and Saffman (1985)],

$$u = 6(1 - 2h_\infty(1 - (h_\infty)^2 \frac{Bo}{3Ca}))y(y - 1) + 1; v = 0. \quad (6.20)$$

The quantity  $h_\infty$  is the dimensional thickness of the hydrodynamic coating left on the moving plane, and its value is determined as part of the solution.

At the inflow, we assume a unidirectional shear flow ( $u = F(y)$ ) and evaluate the conformation tensors using Eqn.(6).

$$f(C_{xx}) = \frac{L^2}{L^2 - C_{xx} - 2}, \quad (6.21)$$

$$C_{xx} = 1 + \frac{2We^2}{f(C_{xx})^2} \left( \frac{du}{dy} \right)^2, \quad (6.22)$$

$$C_{xy} = \frac{We}{f(C_{xx})} \frac{du}{dy}, \quad (6.23)$$

$$C_{yy} = C_{zz} = 1, \quad (6.24)$$

$$C_{xz} = C_{yz} = 0. \quad (6.25)$$

All the boundary conditions specified above are essential boundary conditions i.e. they replace the respective governing equations at the boundary nodes, with the exception of  $\vec{n} \cdot \boldsymbol{\sigma} \cdot \vec{n}$  which is imposed naturally.

### 6.2.2 Finite Element Formulation of the Governing Equations

The FEM formulation is essentially the same scheme employed by Lee et al. and Bhatara [Lee et al. (2002); Bhatara et al. (2004a)] and we present a brief account of it here. For further details refer to [Lee et al. (2002); Bhatara et al. (2004a)]. The DEVSS formulation proposed by Guenette and Fortin [Guenette and Fortin (1995); Yurun and Crochet (1995); Szady et al. (1995); Talwar and Khomami (1992)], is used to discretize the fluid governing equations. Hierarchic shape functions,  $N_k$ , formed by linear combination of Legendre polynomials are used to approximate the variables of the problem [Talwar and Khomami (1992); Talwar et al. (1994); Khomami et al. (1994)]. Since the flow is incompressible, the velocity and pressure fields must satisfy the Ladyzhenskaya-Babuska-Brezzi (LBB) condition that requires the velocity interpolant to be of higher order than the pressure interpolant. Hence the basis functions are quadratic for velocity and bilinear for other variables.

$$\vec{u} = \sum_{i=1}^9 \vec{u}^i N_i \quad \dot{\gamma} = \sum_{i=1}^4 \dot{\gamma}^i N_i \quad P = \sum_{i=1}^4 P^i N_i \quad \tau_p = \sum_{i=1}^4 \tau_p^i N_i \quad (6.26)$$

$$\vec{x} = \sum_{i=1}^{Mx} (\vec{X}_i + \vec{d}^i) N_i \quad (6.27)$$

where  $\vec{X}_i$  is the initial fixed nodal position and  $\vec{d}$  is the unknown displacement vector that contains information about the flow domain deformation. No constraint analogous to the LBB condition exists for the mesh displacement vector since a compressible pseudo-solid approach is used to model the mesh deformation.

A standard Galerkin formulation is used to discretize the momentum and continuity equations. We use the Streamline Upwind Petrov-Galerkin method (SUPG) proposed by Brooks and Hughes [Brooks and Hughes (1982)] to integrate the constitutive equation. To avoid excessive discretization error all second-order derivatives are integrated by parts using the divergence theorem. In addition, the

strain rate is discretized in order to provide numerical stabilization [Guenette and Fortin (1995)].

### 6.2.3 Free Boundary Formulation

A computational mesh that conforms to the fluid domain is used to perform the simulations. The edges of the mesh conform to both the free and fixed boundaries of the domain. Hence, the mesh must deform as the fluid surfaces deform. This section briefly describes the methodology used to generate the mesh deformation. We employ the pseudo-solid domain mapping technique developed by Sackinger [Sackinger et al. (1996)]. We treat the mesh as a fictitious elastic solid, which deforms in response to boundary loads. As the mesh boundary conforms to the domain occupied by the fluid, the mesh interior adjusts as though it were a compressible elastic solid. The advantages of using this method are that it can be easily applied to unstructured meshes, and it is easily implemented in an Eulerian finite element framework for analysis of non-linear problems. The basic premise of pseudo-solid deformation is that the internal mesh is a stress free state of the fictitious solid,  $X$ . Then as the mesh boundaries get distorted, the mesh deforms to a new stressed state,  $x$ . The relationship between the stressed state and the stress-free state is the deformation field

$$\vec{x} = \vec{X} + d, \quad (6.28)$$

where  $d$  is the displacement field that represents how the material points in the pseudo-solid have deformed to accommodate fictitious elastic stresses. A central objective of the problem is, hence, to determine the mapping  $d$ . The deformation of the pseudo-solid in the interior of the mesh is governed by a quasi-static momentum equation

$$\vec{\nabla} \cdot \mathbf{S} = 0, \quad (6.29)$$

where  $S$  is the Cauchy stress in the pseudo-solid. The pseudo-solid stress  $S$  is related to the deformation field through a constitutive equation. We are using a Hookean elasticity formulation, which has been previously shown to provide acceptable mesh deformation behavior [Lee et al. (2002); Sackinger et al. (1996)]

$$\mathbf{S} = \text{tr}(\mathbf{E})\mathbf{I} + 2\mathbf{E}, \quad (6.30)$$

where  $I$  is the identity matrix and  $E$  is the Eulerian strain tensor. Previous attempts at pseudo-solid mesh deformation utilized a small deformation, linear strain tensor [Lee et al. (2002); Sackinger et al. (1996)]. We employ a non-linear form for  $E$

$$\mathbf{E} = \frac{1}{2}[\vec{\nabla}\vec{d} + \vec{\nabla}\vec{d}^T - \vec{\nabla}\vec{d}.\vec{\nabla}\vec{d}^T]. \quad (6.31)$$

The use of the finite strain form is important for flows in which the domain experiences large deformation, as it can alleviate undesirable mesh deformation by eliminating artificially induced stresses [Cairncross et al. (2000)]. This non-linear form for the strain rate tensor does not greatly affect the computational cost as the set of discretized equations for fluid flow are non-linear and hence additional increase in computational memory and time due to an introduction of non-linearity in the pseudo solid deformation is not significant.

#### 6.2.4 Boundary conditions on mesh deformation

The body of the pseudo-solid mesh deforms in response to boundary deformation. Hence, the boundary conditions on the mesh dictate the solution of the mesh deformation. There are two main types of conditions applied on mesh surfaces. Dirichlet conditions and distinguishing conditions. Dirichlet conditions specify the value of the displacement field at each node along a specified boundary; hence they specify both boundary shape and the distribution of nodes on the boundary. Distinguishing conditions are equations that prescribe the shape of the free surface

but not the distribution of nodes along the free surface, hence allowing the nodes to redistribute tangentially to minimize the pseudo-solid shear stresses on the boundary, i.e.

$$t\vec{n} : \mathbf{S} = 0, \quad (6.32)$$

where  $t$  is the tangent to the surface and  $n$  is the normal. This procedure yields acceptable mesh deformation [Lee et al. (2002); Sackinger et al. (1996)].

The kinematics boundary condition is also a distinguishing condition on the mesh deformation, i.e., the boundary deforms to make the normal component of fluid velocity equal to zero,

$$\vec{n} \cdot (\vec{u} - \vec{u}_s) = 0. \quad (6.33)$$

This condition makes the free surface a material surface in the normal direction, i.e., no mass crosses the surface. Similar to geometric distinguishing conditions it is convenient to allow the nodes on a free surface to redistribute to minimize pseudo-solid stresses. Attention has to be paid to special points like corners, which are the junctions or intersections of two or more boundaries, and at which it is mathematically impossible to impose a tangential traction free constraint or define a unique normal vector. Hence, multiple distinct constraints apply at the corner points and the deformation of the point is determined by using the corresponding set of distinguishing conditions. The normal hierarchy is that Dirichlet conditions take precedence over distinguishing conditions, and geometric conditions take precedence over free boundary conditions. However, care must be taken not to lose valuable boundary data. For instance, in order to correctly detect the deformation of the corner, we enforce the interfacial force balance in the  $x$  direction as the last boundary condition.

The boundary conditions on the pseudo-solid momentum equations are often difficult to apply because these distinguishing conditions are usually applied on arbitrarily oriented surfaces. Spurious mesh stresses can appear if the surface projection of the distinguishing condition is non-zero. Hence, it is important that the

distinguishing condition constrains only the normal deformation of the boundary and permits the nodes to redistribute freely in the tangential direction. So, it is convenient to express the pseudo-solid equations in normal and tangential components. The normal component is replaced by the distinguishing condition and the tangential components allow shear-free distribution of the nodes.

### 6.2.5 Mesh Convergence

The residual equations obtained via the FEM formulation [Lee et al. (2002)] are solved via the Newton's iteration method, with first order continuation in both  $Ca$  and  $We$ . In the earlier study conducted by Lee [Lee et al. (2002)], the authors tested their convergence for a FENE-CR model, with  $L = 10$ . With their finest mesh, convergence up to a  $We$  of 0.61 (at a  $Ca$  of 0.2), was attained. The convergence was limited because of stress oscillations in the capillary transition region that could not be resolved given the level of discretization and the choice of polynomial spaces. So for comparison purposes we have used the aforementioned choice of the parameters. In addition, this choice of parameters is motivated by the prior experimental studies [Lee et al. (2005)].

To resolve the resolution issue, meshes should have sufficient discretization. Hence, the mesh design strategy employed in this study, is to maximize the number of elements in the capillary transition region, where the stress boundary layers develop, while minimizing the number of elements in the rest of the fluid domain. The numerical solution has been tested for convergence by varying the mesh density, as depicted in figure 6.3. Two different meshes with numbers of elements equal to 16123 and 17136 respectively have been used. Although the number of elements in these two discretizations are not very different, using the above strategy we have been able to reduced the size of the elements in the capillary region by a factor of approximately 2.5 (see figure 6.4 for details). The convergence criterion adopted requires the norm between two consecutive iterations to be equal or smaller than  $10^{-5}$ . We performed

a convergence study similar to what has been performed by Lee [Lee et al. (2002)]. The numerical scheme is very robust in terms of the mesh deformation and capturing the boundary layer stresses. In case of recirculation flow (low  $Ca$ , low  $Bo$ ), the convergence is limited by the resolution of the stress boundary layers. We quantify this by conducting a normal stress and a normal stress gradient probe along various heights in the flow domain. At higher  $We$  oscillations in the polymer stresses start to appear (see figure 6.5). These sharp stress gradients cannot be captured given our mesh sizes and choice of polynomial spaces. The value of  $We$  to which convergence can be attained increases with increasing  $Ca$  or decreasing  $Bo$  (refer to Table 6.1). This is to be expected since increasing  $Ca$  or decreasing  $Bo$  results in lower strain rates and subsequently leads to lower stresses in the stress boundary layer in the capillary transition region.

$Ca$	0.01	0.05	0.1	0.2
$Bo$	60	60	160	200
$We$	0.57	0.63	0.72	0.79

**Table 6.1:** Convergence studies: Maximum  $We$  attained for fixed  $Ca$  and  $Bo$

## 6.3 Results

### 6.3.1 Low $Ca$

In the absence of gravity, the meniscus is almost circular at the tip of the air-liquid interface near the plane of symmetry while the circular shape of the interface in the capillary transition region is deformed by viscous and elastic forces [Ro and Homsy (1995)]. At high  $Bo$ , the meniscus at the tip of the air-liquid interface near the plane of symmetry and the interface in the capillary transition region are flattened because of the presence of gravity (see figure 6.6). The amount of compression of the air-liquid interface in the capillary transition region and subsequent flattening of the

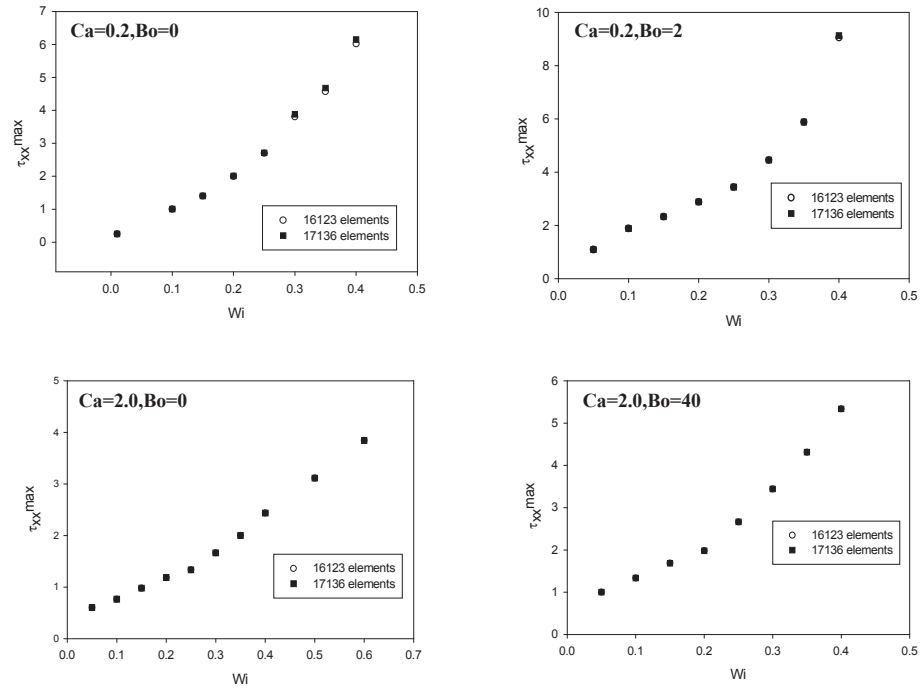


**Figure 6.3:** Convergence studies,  $\tau_{xx}$ , for two different meshes, for low and high  $Ca$  flows.

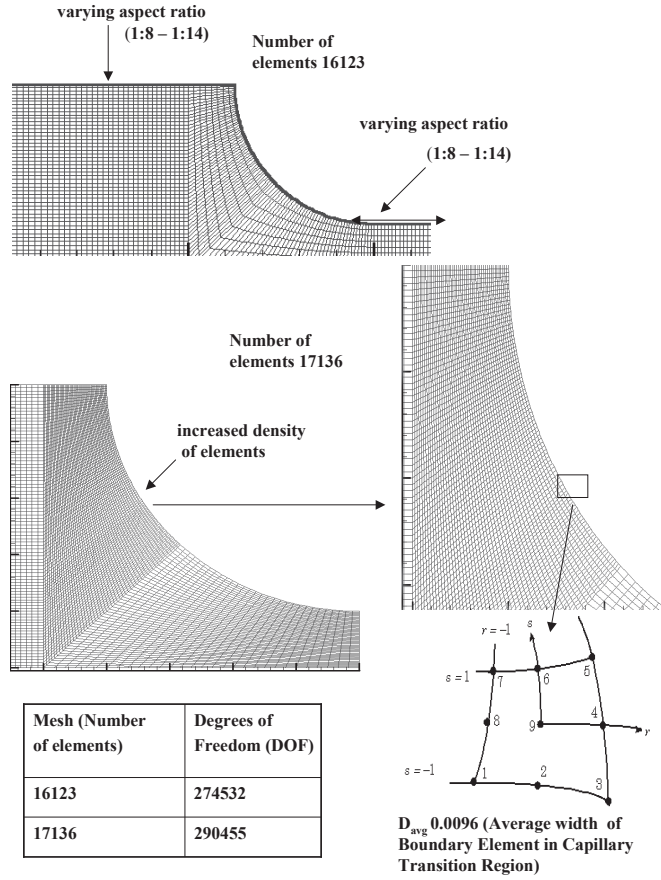


**Figure 6.4:** Details of the computational grids. The design philosophy is to have fine discretization in the capillary transition region and near the tip of the air-liquid interface close to the plane of symmetry. The average width of smallest element in Capillary transition region is within range of 0.0096 to 0.0250 for meshes with 17136 and 16123 elements, respectively. The computational domain is 14 non-dimensional unit long and 0.5 wide. The position of air-liquid interface near the plane of the symmetry is located at  $x = 5$ , and the flow properties are independent of  $x$  for  $x < 3$  and  $x > 7$ . The results with a computational domain which is 10 non-dimensional unit long are exactly the same as the computations performed with the longer domain (i.e. 14 non-dimensional unit long).

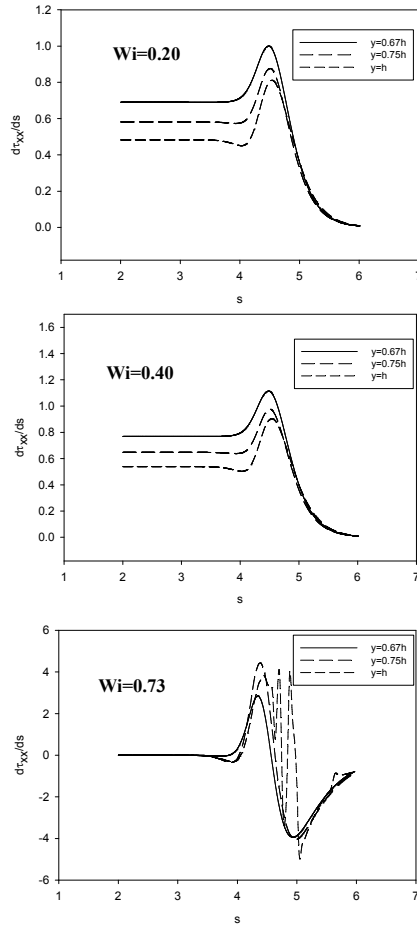


**Figure 6.5:** Illustration of the normal stress resolution for different  $We$  flows, ( $Ca = 0.1, Bo = 160$ ).  $s$  is the distance along the interface measured from the tip of the air-liquid interface near the plane of symmetry.

interface increase with increasing  $Bo$ . The flow streamlines and the effective strain rate (defined as the second invariant of the strain rate tensor [Bhatara et al. (2005b)]) are illustrated in figure 6.7 for representative values of  $Ca$ ,  $We$  and  $Bo$ . Figure 6.7-(a) corresponds to  $Ca = 0.01$ ,  $Bo = 40$  and  $We = 0.5$ , while figure 6.7-(b) corresponds to  $Ca = 0.01$ ,  $Bo = 60$  and  $We = 0.5$ . The flow is characterized by a recirculation pattern and an interfacial stagnation point, in addition to the stagnation point at the tip of the air-liquid interface near the plane of symmetry. The strain rates are highest adjacent to the wall under the thin film region and at the interface in the capillary transition region. The flow near the wall is predominantly a shear flow, while under the free surface is a planar extensional flow [Bhatara et al. (2004a); Lee et al. (2005); Bhatara et al. (2005b)]. A close examination of the streamlines and the strain rates indicates a strengthening of the recirculation region and an increase in the maximum effective strain rate with increasing  $Bo$ .

Figure 6.8 depicts contours of the elastic normal stress ( $\tau_{xx}$ ) at  $Ca = 0.01$  and  $We = 0.5$ , for a variety of  $Bo$ . As in the Hele-Shaw flow, formation of a normal stress boundary layer at the free surface downstream of the interfacial stagnation point is observed at high values of  $We$  [Bhatara et al. (2004a); Lee et al. (2005); Bhatara et al. (2005b)]. It has been ascertained previously that these normal stress boundary layers occur because of the local extensional flow at the interface [Bhatara et al. (2004a, 2005b)]. In addition to the normal stresses formed at the interface, high strain rates at the wall result in an increase in the normal stresses at the wall under the thin film (see figure 6.8). For fixed  $We$ , as the value of  $Bo$  is increased, there is an increase in the magnitude of the maximum normal stress in the stress boundary layer (see figures 6.8 and 6.9). However, despite of the increase in the normal stresses and their gradients that have been shown to lead to film thickening [Bhatara et al. (2004a, 2005b)], the film thickness is reduced with increasing  $Bo$  (see figure 6.12), as gravitational force resists the passage of fluid elements in the thin film region and becomes dominant at high  $Bo$ . The interplay of various forces responsible for determination of the film thickness are the same as in the Hele-Shaw flow, i.e.,

viscous stresses at the wall  $\frac{\partial\tau_{xy}}{\partial x}$  have a film thickening effect, normal stress gradients  $\frac{\partial\tau_{xx}}{\partial x}$  have a film thickening effect if positive in the direction of flow, and gravity has a film thinning effect [Bhatara et al. (2004a, 2005b)]. This is illustrated schematically in figure 6.10. This can be clearly ascertained by examining the line plots of the stress gradients,  $\frac{\partial\tau_{xx}}{\partial x}$  and  $\frac{\partial\tau_{xy}}{\partial y}$ , in figure 6.8. The two vertical lines indicate the location of the interfacial stagnation point A and the point at which the gradient of the free surface variation falls below  $10^{-5}$ . The line plots of the stress gradients indicate that, once the stress boundary layer forms, the normal stress gradient  $\frac{\partial\tau_{xx}}{\partial x}$  near the interface is much larger than the shear stress gradient  $\frac{\partial\tau_{xy}}{\partial y}$  near the wall. Furthermore, a close examination of the stress gradients shows the presence of a net positive normal stress gradient that results in a film thickening effect.

In order to separate the effects of normal stress gradients and gravity on film thickness, we plot the percentage deviation from the Newtonian film thickness as a function of  $We$  in figures 6.11-(a) and (b) as well as figures 6.12-(a) and (b), where the film thickness,  $h$ , has been made dimensionless with the gap half width  $b$ . For the same  $Ca$  and  $We$ , increasing  $Bo$  results in thinner films, while for the same  $Ca$  and  $Bo$ , increasing  $We$  results in thicker films. Figures 6.12-(a) and (b) also indicate that the film thickness made dimensionless with the gap width is a function of both  $Ca$  and  $Bo$ . Furthermore, as in the Hele-Shaw flow, a film thinning effect is observed at low  $We$  followed by a film thickening effect at high  $We$ . The onset of the film thickening effect occurs at the same value of  $We$  at which the formation of the normal stress boundary layer occurs. It has been shown previously that in the Hele-Shaw flow, in the limit of low  $Ca$  and  $We$ , the film thinning occurs due to the presence of negative normal stress gradients in the flow direction, i.e.,  $(\frac{\partial\tau_{xx}}{\partial x} < 0)$ , that are greater than the shear stress gradients. The onset of the normal stress boundary layer results in positive normal stress gradients  $(\frac{\partial\tau_{xx}}{\partial x} > 0)$  that triggers film thickening [Bhatara et al. (2004a)].

To examine the flow characteristics in the dip coating flow limit, the film thickness scaled with the Bond number (i.e.,  $hBo^{1/2}$ ) as a function of  $We$  is plotted in figures

6.13-(a) and (b). It can clearly be seen that the film thickness nearly collapses onto a single curve at high  $Bo$ , indicating that the film thickness scaled with the correct characteristic length, i.e. the capillary length,  $l$ , is independent of  $Bo$  and it only is a function of only  $Ca$  and  $We$ . This result shows that at small  $Ca$  and for  $Bo > 10$  the flow near one of the plane is not effected by the presence of the other plane, hence, the dip coating flow limit has been reached. Furthermore, at low values of  $We$  the scaled film thickness shows good agreement with the Ro and Homsy expression (see Equation 6.3 which is valid in limit of small  $We$ ). However as expected a significant departure is seen between the result of our simulations and the Ro and Homsy expression as the value of  $We$  is increased. This is due to the fact that the Ro and Homsy used an asymptotic expansion that is valid in the limit of low  $We$  to obtain Equation 6.3. Hence, their expression can only capture film thinning observed at low  $We$ . Moreover, given the fact that our simulations for low values of  $We$  agree with the Ro and Homsy expression for the dip coating flow further underscores that the capillary length is indeed the appropriate length scale at sufficiently high  $Bo$ , i.e., the dip coating flow limit.

### 6.3.2 Moderate $Ca$

Similar to the observations for interface shapes at low values of  $Ca$ , the meniscus at the tip of the air-liquid interface near the plane of symmetry and the interface in the capillary transition region are flattened because of the presence of gravity at high values of  $Bo$  (see figure 6.14). However, at  $Bo = 80$  (for both  $Ca = 0.1$  and  $Ca = 0.2$ ), even though there is a flattening of the interface in the capillary transition region, the shape still resembles the interface shape at  $Bo = 0$ , indicating that viscous and elastic forces are still important in determining the interface shape. For higher values of  $Bo$  ( $Bo = 140$  and  $160$  at  $Ca = 0.1$ , and  $Bo = 160$  and  $200$  at  $Ca = 0.2$ ), a pronounced difference in the interface shapes is observed. Specifically, the meniscus is highly flattened indicating that gravity is now the dominant force.

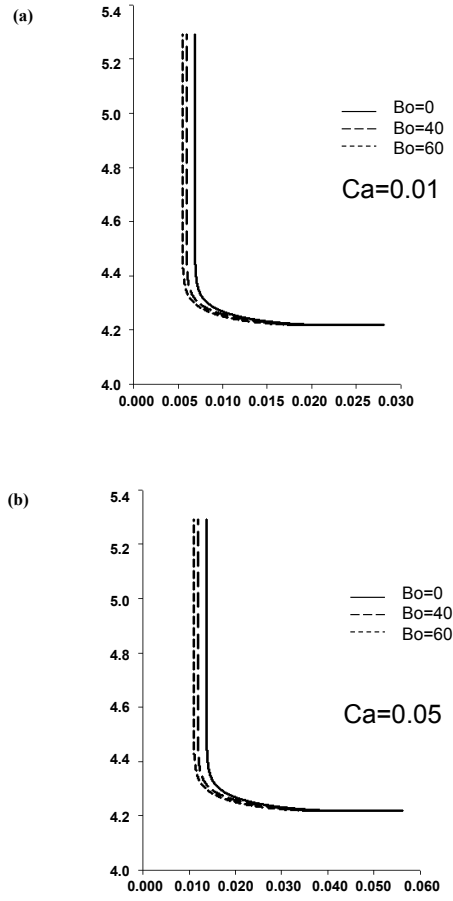


**Figure 6.6:** Interface shapes as a function of  $Bo$ : (a)  $Ca = 0.01, We = 0.5$ , (b)  $Ca = 0.05, We = 0.5$ .

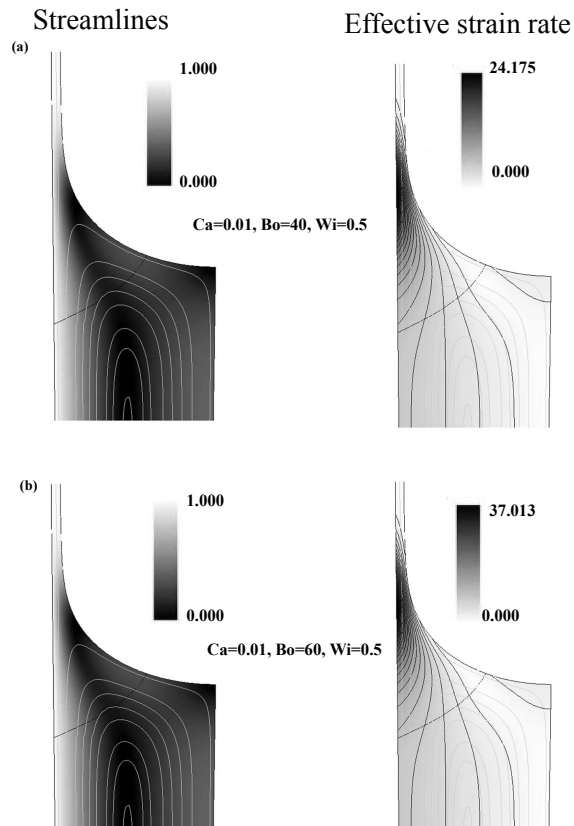


**Figure 6.7:** Contour plots of the streamlines and effective strain rate.

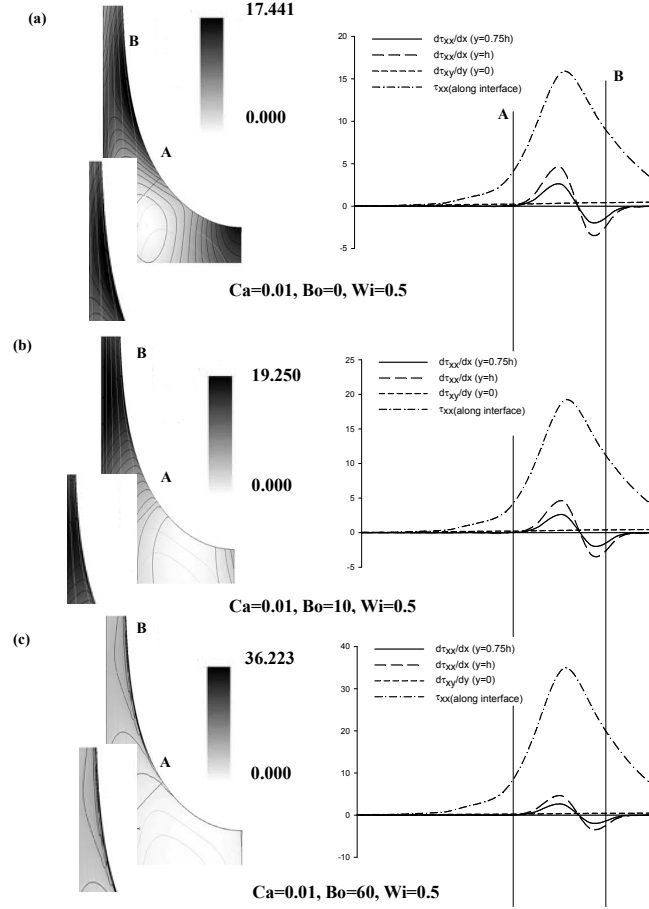


**Figure 6.8:** Contour plots of the the normal stress ( $\tau_{xx}$ ). The insets show a magnified view of the stress contours in the region of large stresses downstream of the interfacial stagnation point. Also corresponding to each figure line plots of stress and stress gradients along the interface are shown.  $A$  represents the location of the stagnation point and  $B$  represents the point where the film thickness variation ( $\frac{dh}{dx}$ ) falls below  $10^{-5}$ .

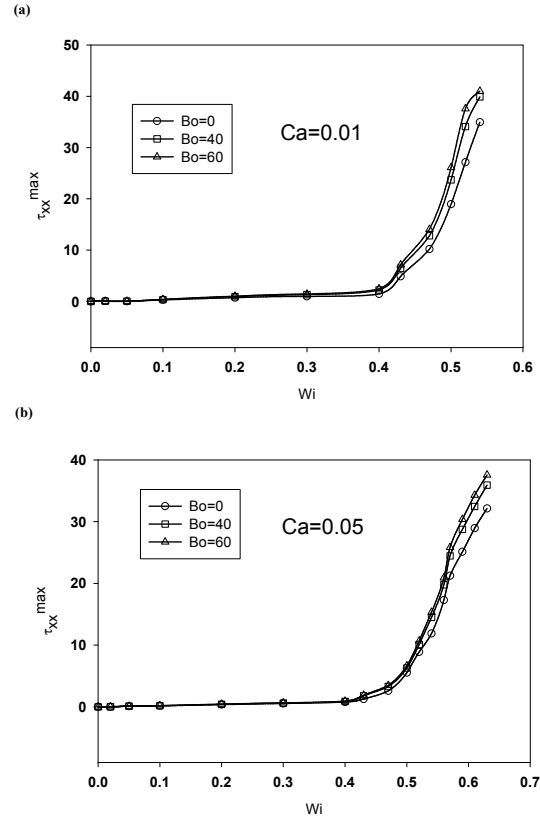


**Figure 6.9:** Maximum normal stress ( $\tau_{xx}^{max}$ ) in the stress boundary layer as a function of  $We$ : (a)  $Ca = 0.01$ , (b)  $Ca = 0.05$ .

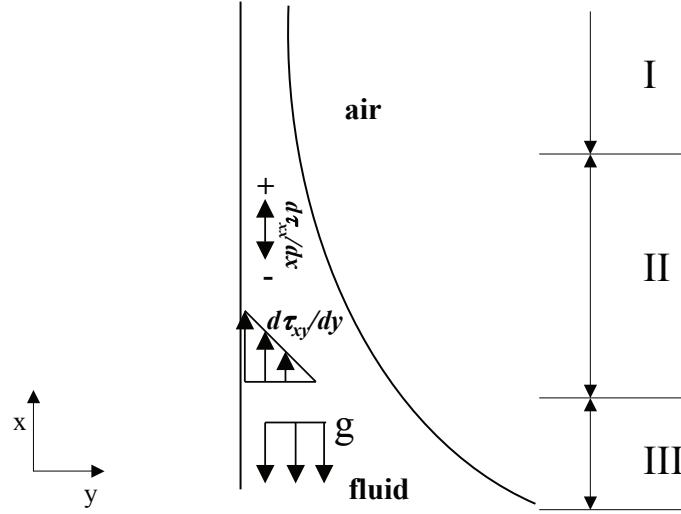


**Figure 6.10:** Schematic illustrating the interplay between various forces that determine the overall film thickness.

This also demonstrates that in order to reach the dip coating flow limit (i.e., gravity dominated regime) at higher  $Ca$ , the corresponding  $Bo$  has to be increased. We plot the streamlines and the effective strain rate at  $Ca = 0.2$  and  $We = 0.5$  for a variety of  $Bo$  values in figure 6.15. The results are very similar to those observed at lower  $Ca$  (see figure 6.7). Specifically, as  $Bo$  is increased, the strength of the recirculation region and the maximum effective strain rate increase.

Contour plots of the normal stress ( $\tau_{xx}$ ) and line plots of stress and stress gradients, are shown in figure 6.16 for  $Ca = 0.2$  and  $We = 0.5$  for a variety of  $Bo$ . As  $Bo$  is increased, the magnitude of the maximum normal stress in the stress boundary layer in the capillary transition region is increased. Furthermore, the development of normal stresses at the wall under the thin film region at high  $Bo$  can be clearly seen (see figure 6.16-(c)). As reported for lower values of  $Ca$ , the maximum normal stress in the stress boundary layer increases with both  $Bo$  and  $We$  (see figure 6.17).

The percentage deviation from the Newtonian film thickness as a function of  $We$  is plotted in figures 6.18-(a) and (b), while the dimensionless film thickness as a

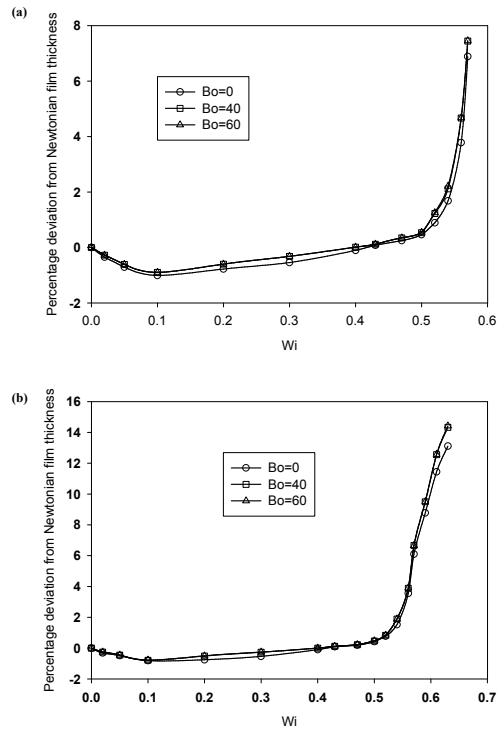


**Figure 6.11:** Percentage deviation from Newtonian film thickness as a function of  $We$ : (a)  $Ca = 0.01$ , (b)  $Ca = 0.05$ .

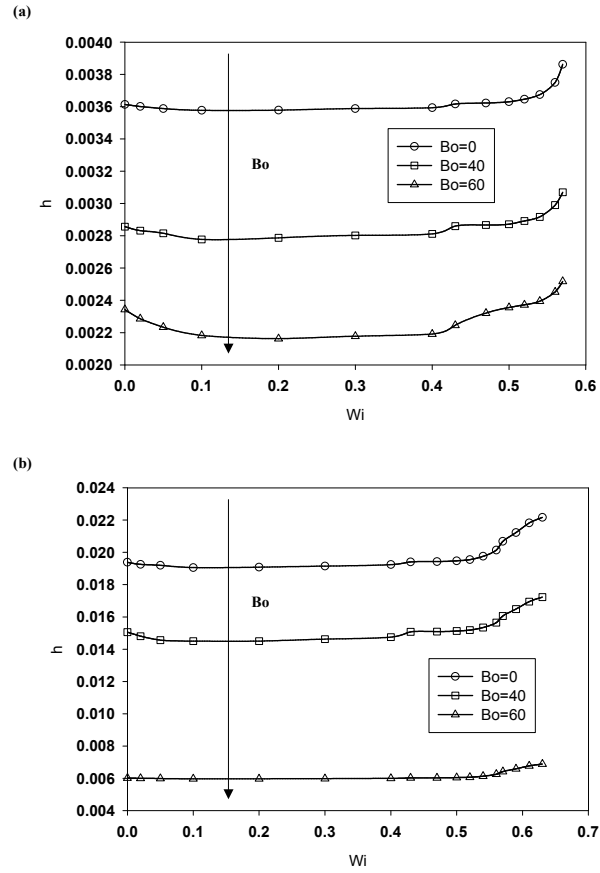


**Figure 6.12:** Film thickness made dimensionless with the gap width ( $b$ ) as a function of  $We$ :(a)  $Ca = 0.01$ , (b)  $Ca = 0.05$ .

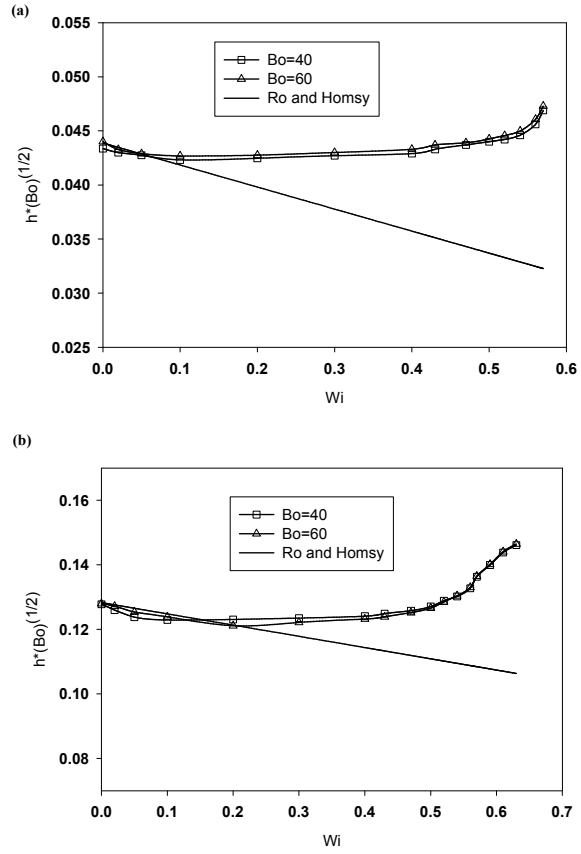


**Figure 6.13:** Film thickness made dimensionless with Bond number ( $Bo$ ) as a function of  $We$ : (a)  $Ca = 0.01$ , (b)  $Ca = 0.05$ .

function of  $We$  is plotted in figures 6.19-(a) and (b). As in the case of lower values of  $Ca$ , it is clear that increasing  $Bo$  has a film thinning effect, while increasing  $We$  results in a film thinning effect followed by a film thickening effect. The mechanism for film thickening is the same as in the low  $Ca$  regime. Plots of the film thickness scaled with the Bond number show that at  $Ca = 0.1$ , the film thickness is nearly independent of the value of  $Bo$  at high  $Bo$  (see figure 6.20-(a)). The scaled film thickness at  $Bo = 140$  and  $Bo = 160$  show good agreement with the Ro and Homsy asymptotic results at low values of  $We$  while the same is not true for the scaled film thickness at  $Bo = 80$ . Similarly at  $Ca = 0.2$ , where the scaled film thickness at  $Bo = 80$  shows significant deviations from the Ro and Homsy correlation at low  $We$ , a good agreement is obtained in this limit between the numerical predictions and the analytical results for  $Bo = 160$  and  $Bo = 200$  (see figure 6.20-(b)). In the other words, the magnitude of  $Bo$  at which the flow near each plane corresponds to dip coating flow increases with an increase in  $Ca$ . Overall, at  $Ca = 0.2$  the dip coating flow regime has been reached at  $Bo \approx 200$ .

## 6.4 Conclusion

In this study we have performed numerical simulations to illustrate that Hele-Shaw simulations can be extended to understand the effects of elasticity on the interfacial dynamics of dip coating flows. Specifically, we have shown that the film thickness scaled with the capillary length, as a function of  $We$ , at low  $Ca$  and high  $Bo$  collapses onto a single curve, and agrees with the Ro and Homsy [Ro and Homsy (1995)] correlation for small values of  $We$ . For a fixed  $Ca$  and  $We$ , an increase in  $Bo$  results in a decrease in the film thickness, an increase in the size of the recirculation region and an increase in the strain rates subsequently leading to an increase in the normal stresses. At low  $We$ , there is a film thinning effect and as the value of  $We$  is increased, there is a film thickening effect that accompanies the formation of a normal stress boundary layer at the free surface in the capillary transition region. Both the

magnitude of the film thickness and the maximum stress in the stress boundary layer increase with increasing  $We$ . Furthermore, the normal stress boundary layer at the free surface is a result of the local planar extensional flow at the interface. These calculations provide a simple way of examining the wealth of interfacial phenomena that are present in dip coating flows.

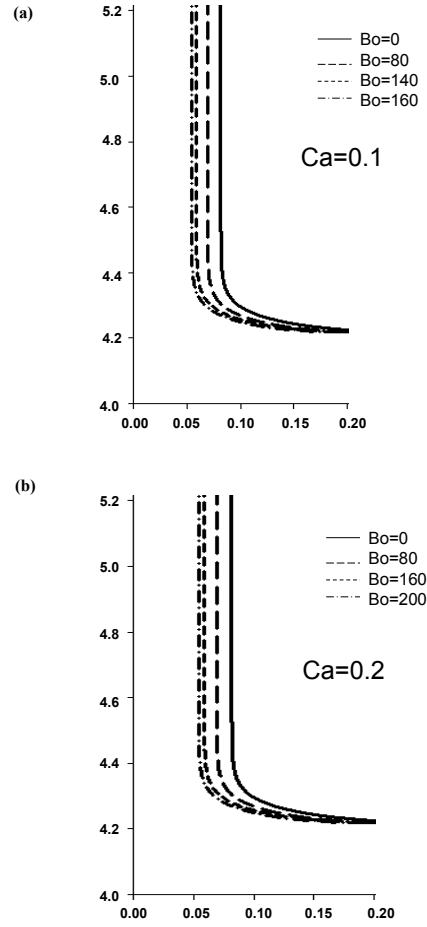


**Figure 6.14:** Interface shapes as a function of  $Bo$ : (a)  $Ca = 0.1, We = 0.5$ , (b)  $Ca = 0.2, We = 0.5$ .

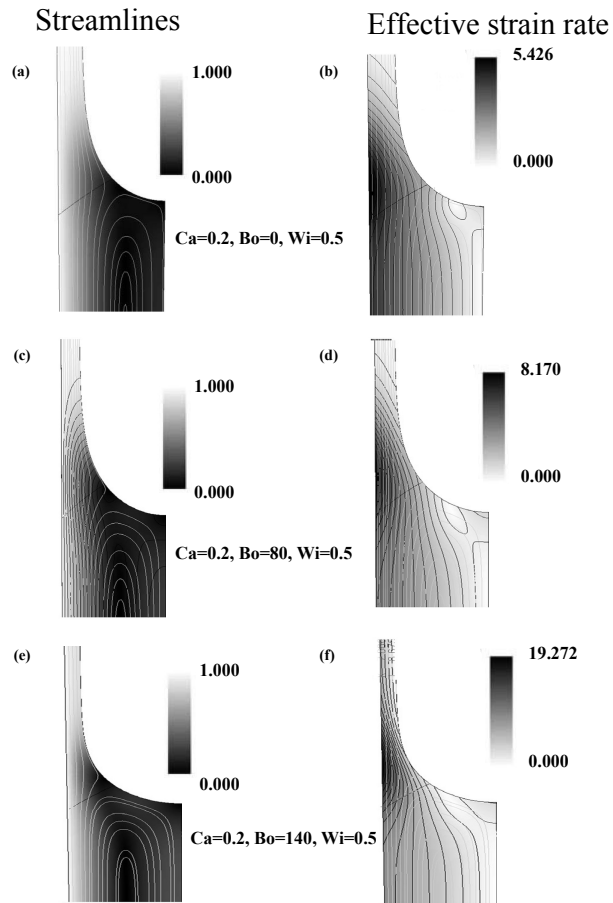


**Figure 6.15:** Contour plots of the streamlines and the effective strain rate.

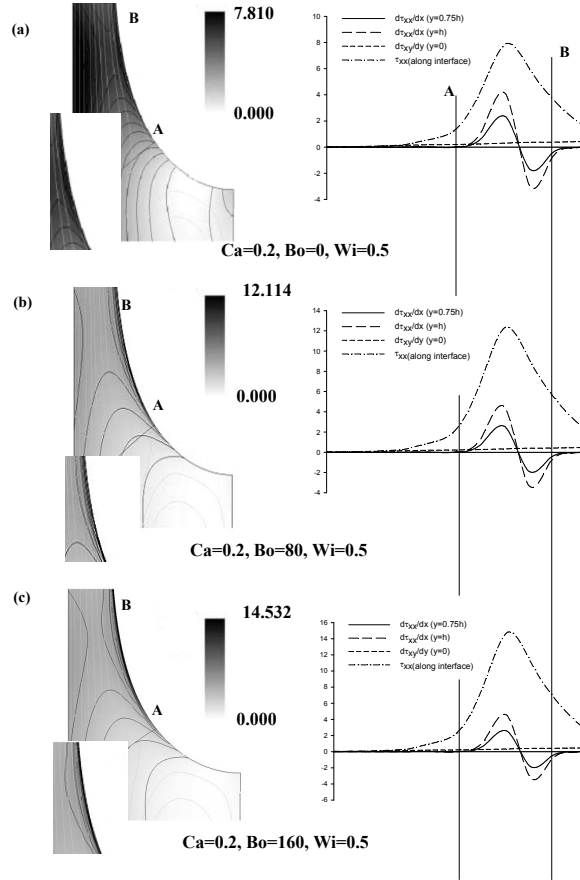


**Figure 6.16:** Contour plots of the the normal stress ( $\tau_{xx}$ ). The insets show a magnified view of the stress contours in the region of large stresses downstream of the interfacial stagnation point. Also corresponding to each figure line plots of stress and stress gradients along the interface are shown.  $A$  represents the location of the stagnation point and  $B$  represents the point where the film thickness variation ( $\frac{dh}{dx}$ ) falls below  $10^{-5}$ .

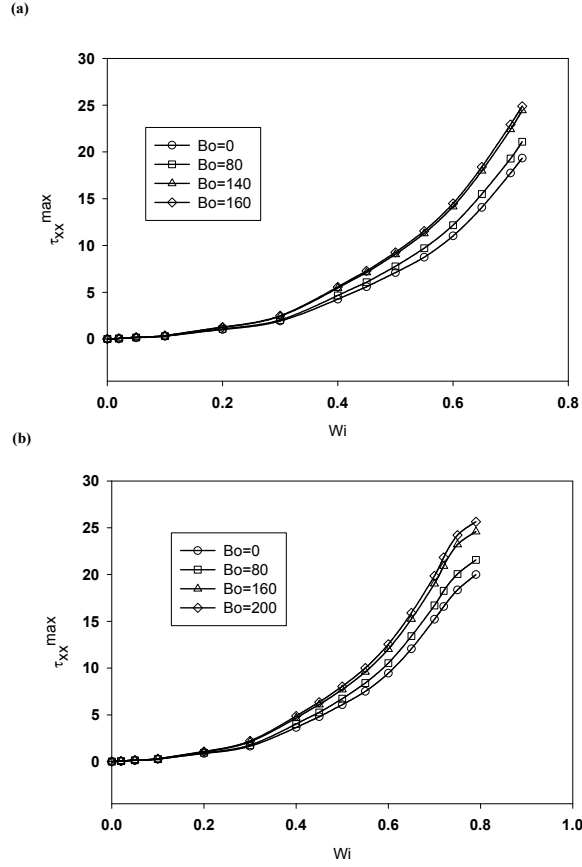


**Figure 6.17:** Maximum normal stress ( $\tau_{xx}^{max}$ ) in the stress boundary layer as a function of  $We$ : (a)  $Ca = 0.1$ , (b)  $Ca = 0.2$ .

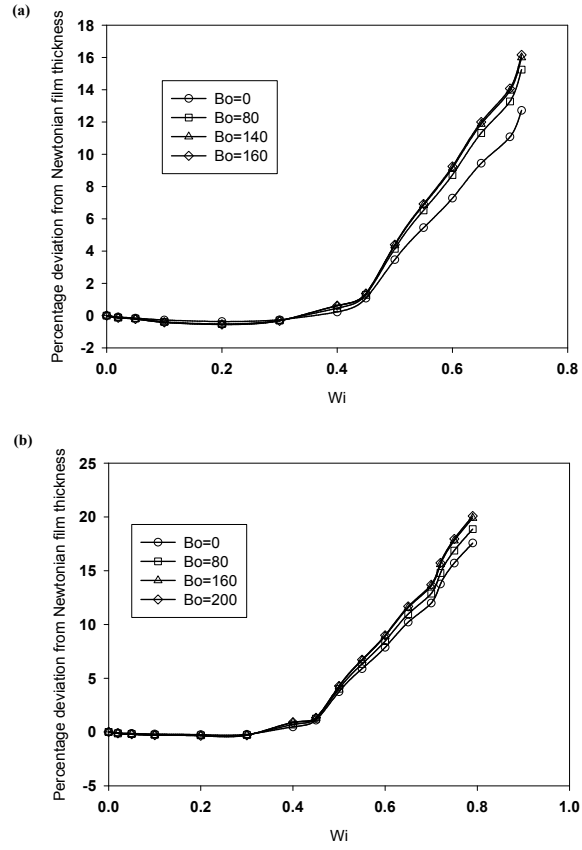


**Figure 6.18:** Percentage deviation from Newtonian film thickness as a function of  $We$ : (a)  $Ca = 0.1$ , (b)  $Ca = 0.2$ .

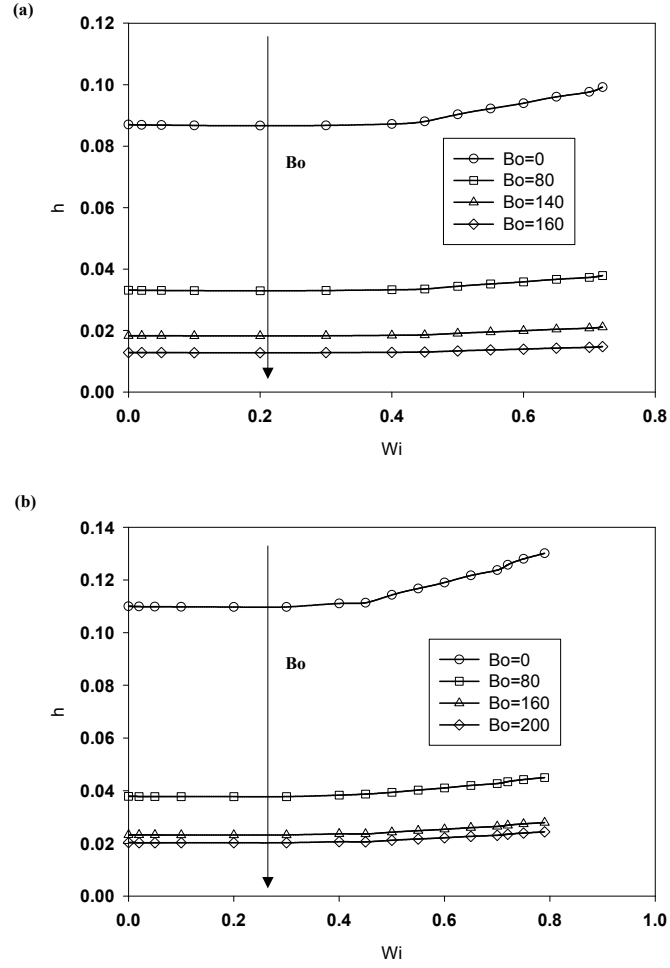


**Figure 6.19:** Film thickness made dimensionless with gap the width ( $b$ ) as a function of  $We$ :(a)  $Ca = 0.1$ , (b)  $Ca = 0.2$ .

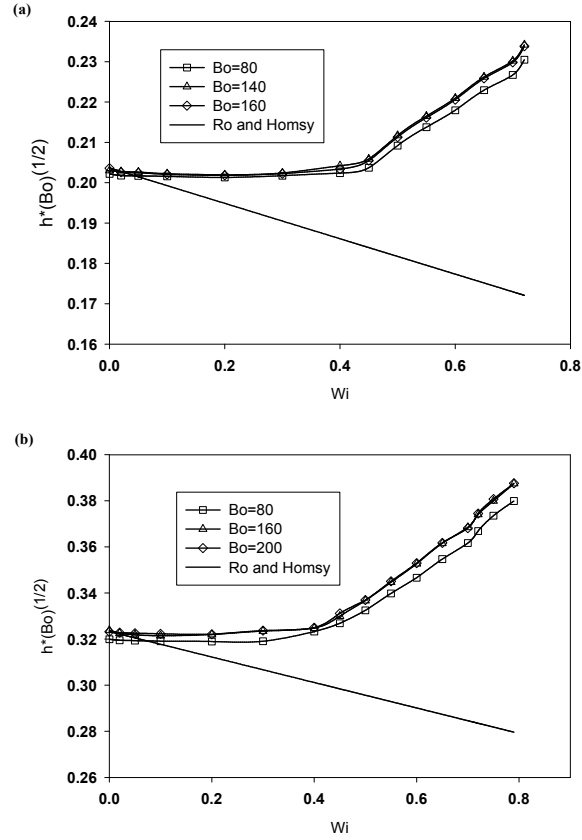


**Figure 6.20:** Film thickness made dimensionless with Bond number ( $Bo$ ) as a function of  $We$ : (a)  $Ca = 0.1$ , (b)  $Ca = 0.2$ .

# Chapter 7

## Plunging of solid surfaces into Newtonian and viscoelastic fluids: an experimental/numerical study

### 7.1 Introduction

As mentioned in the previous chapter, free surface flows are ubiquitous in nature, consequently they are of great fundamental and industrial importance. In one of the most comprehensive studies on influence of fluid elasticity on the interfacial dynamics of coating flows [Lee et al. (2005)], an eccentric-cylinder device was used to examine the dynamics of air-liquid interfaces during immiscible displacement flows. Specifically in this study it was clearly demonstrated that in the eccentric-cylinder forward-roll coating flow with gravity stabilization the elastic liquid free surface readily evolves into stable, two-dimensional sharp interfaces and there is a dramatic increase in coating film thickness with an increase in the flow  $We$ . However, the investigations in this study were mainly focused on the dynamics of the air-liquid interface at the front of coater, assuming that the front interface dynamics is

independent of flow kinematics and interfacial dynamics near the air-liquid interface at the back of coater.

This study constitutes a continuation of an ongoing numerical/experimental investigation of the effect of fluid elasticity on free surface displacement flows in our research group. Specifically, it is focused on the air-liquid interface dynamics in the back of the coater and its impact on the overall flow dynamics. In the back of the coater, the flow is that of wet substrate being plunged into a bath liquid, hence, we have dubbed this flow, the "wet plunge flow". The wet plunging flow problem is the opposite of the dip coating problem discussed in the previous chapter where a thin liquid film is formed on a flat plate drawn vertically from a liquid bath [Landau and Levich (1942); White and Tallmadge (1965); Esmail and Hummel (1975); Adachi et al. (1978); Abedijaberi et al. (2011)]. Hence, studying the influence of flow elasticity on the wet plunging flow is of fundamental importance not only because of its scientific significance but also due to its potential impact on the interfacial dynamics of various industrial coating processes.

## 7.2 Experiment

The experimental apparatus used in this study was developed in our research group by Lee [Lee et al. (2005)] and it consists of two horizontal cylinders of different radii with one placed inside the other (see Figure 7.1). The device is designed in a way that the eccentricity between cylinders and the rotation speed of each cylinder can be accurately controlled and the shape of the interface can be recorded using a laser sheet. More details about this apparatus can be found in [Lee et al. (2005)].

In this study we have focused our attention on the wet plunging flow in the back of the eccentric-cylinder forward-roll coating device (see figure 7.2). The experimental fluid is H-40 Indopol polybutene polymer (Ineos Oligomers) which is a Newtonian fluid with a viscosity of 60 P and surface tension of 30  $\text{dyn cm}^{-1}$ .

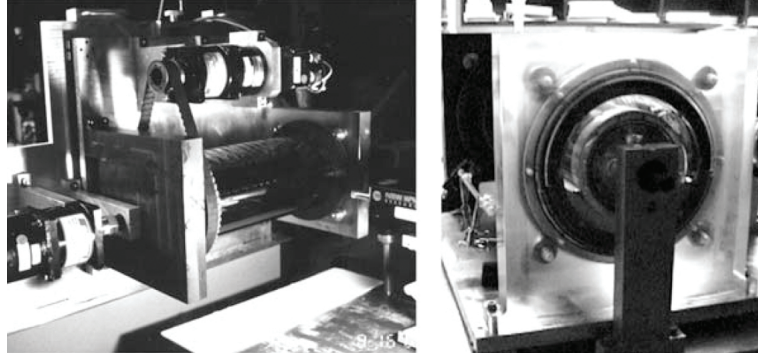


**Figure 7.1:** Eccentric-cylinder coating apparatus: Plexiglas outer cylinder (a) and acrylic end plate (b) for direct visualization of interfacial dynamics.

## 7.3 Problem formulation and numerical technique

We consider the plunging of two parallel pre-wetted vertical planes into a bath of liquid as depicted in Figure 7.2. The problem formulation is identical to dip coating flow (see chapter 6) with the only difference being the direction of motion of the substrate with respect to gravity. Specifically the direction of the wall movement in the wet plunging flow is opposite of the direction of the wall movement in the dip coating flow. It should also be noted that in the wet plunging flow the film thickness on the substrate is prescribed rather than being determined as part of the solution, as it is in the simulation of the dip coating flow. The numerical technique used to solve the set of governing differential equations are described in details in chapter 6.

### 7.3.1 Mesh Convergence

The residual equations obtained via the FEM formulation are solved using the Newton's iteration method, with first order continuation in  $Ca$  and  $We$ . The numerical solution has been tested for convergence by varying the mesh density. Specifically, two different meshes with numbers of elements equal to 5074 and 19515 respectively have been used (see figure 7.3). With both meshes converged solutions are obtained for  $0.1 \leq Ca \leq 5$ . Although it is possible to continue the calculations to

a wider range of  $Ca$ , most of the interesting interfacial dynamics are observed in this range of  $Ca$ . It should also be noted that the results presented in the remainder of this chapter are based on the mesh with 5074 elements and are mesh converged (see figure 7.4).

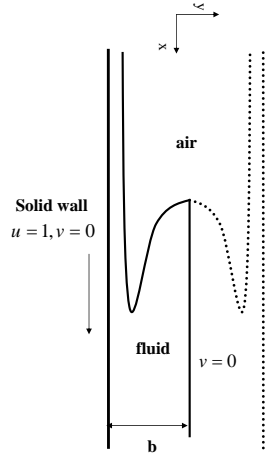


**Figure 7.2:** Schematic of wet plunging flow.

## 7.4 Results and discussion

As mentioned earlier, prior experimental and numerical investigations have elucidated the effects of  $Ca$ ,  $We$  and gravity on the front air-liquid interface in the cylindrical coater [Bhatara et al. (2004a); Lee et al. (2005)]. Specifically it has been shown that in the absence of gravity, a recirculation flow occurs near the tip of the air bubble at low  $Ca$  ( $Ca < 1.0$ ) and a bypass flow is observed at high  $Ca$  ( $Ca > 1.0$ ). As fluid elasticity is enhanced an increase in the hydrodynamic film thickness and meniscus invasion (formation of a sharp interface) is observed. Gravity has a film thinning effect [Bhatara et al. (2004a); Lee et al. (2005)]. In this study we have examined the effect of these key variables on the dynamics of the air-liquid interface at the

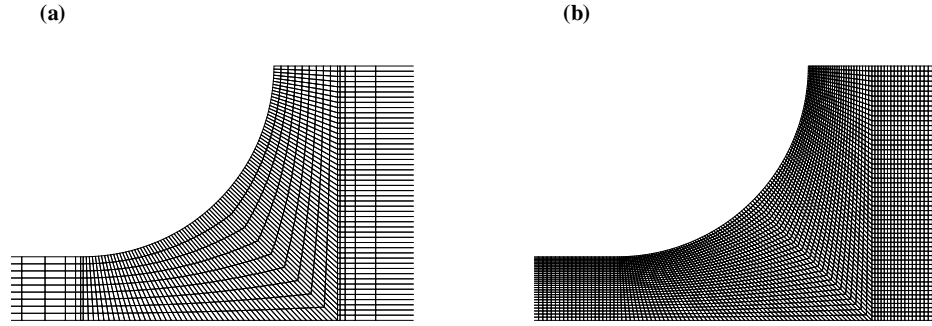


**Figure 7.3:** The computational domain near the air-liquid interface for meshes with (a) 5074 elements and (b) 19515 elements.

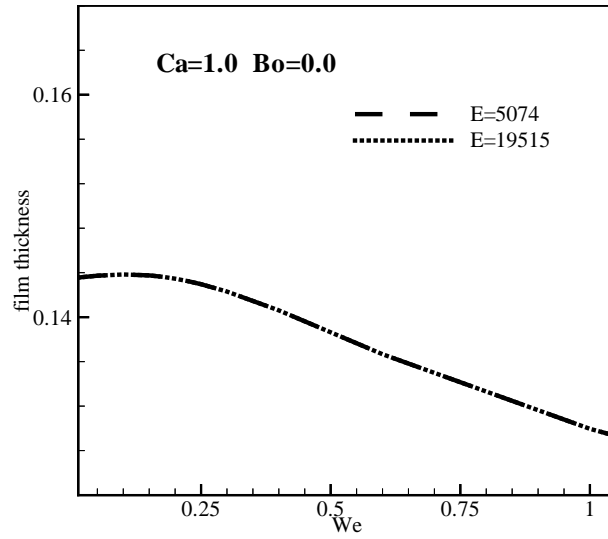


**Figure 7.4:** Convergence studies for two different meshes used in the wet plunging flow simulations.

back of the eccentric cylindrical coater for Newtonian fluids. In addition, preliminary computations to examine the influence of fluid elasticity on the interfacial dynamics of the wet plunging flow have been performed.

### 7.4.1 Newtonian wet plunging flow

#### Simulation results

At steady state, the air-liquid interface is in mechanical equilibrium, i.e. there is no motion of any part relative to any other part. As in mechanical equilibrium the state of stress is isotropic, the only force exerted by the liquid on the interface is the equilibrium pressure, which locally acts normal to the interface. The equilibrium interfacial normal force in liquid phase is the sum of hydrostatic pressure, which develops due to the body forces, hydrodynamic pressure and stresses created due to the fluid motion. The local difference in the pressures exerted on the interface by the air and liquid force exerted normal to the interface must be balanced by the capillary force. Earlier studies [Brown (1979)] have clearly shown that for complex non-linear interface shapes various solution families can be obtained for the Young-Laplace equation. Consequently, if the Capillary force is the dominant force near the air-liquid interface, for instance in the absence of gravity in the flow direction, one could obtain multiple equilibrium interface shapes, many of which have been observed experimentally [Brown (1979)]. For example, various equilibrium shapes, i.e. axisymmetric, C-shaped, two-lobed and annular shapes, could form when a rotating liquid drop is attached to a rod and immersed in a liquid of equal density where the drop is held together solely by surface tension [Brown (1979)]. Therefore, in this study we have carefully investigated the existence of multiple steady state solutions under condition of no gravity and minimal flow force near the air fluid interface at the plane of symmetry.

The simulations indeed exhibit multiple solutions for the shape of the interface; moreover it is shown that the thickness of the liquid on the surface that is being

plunged and  $Ca$  determine which solution family is attained. Specifically, different families of solutions with a given initial film thickness is observed depending on whether  $Ca$  is ramped up or down. In fact, complex bifurcations are observed in the intermediate  $Ca$  regime, i.e.  $Ca \approx 1$ . Moreover, the initial guess used to start the computations at small or high  $Ca$  (i.e., ramp up or ramp down modes) influences the solution family that is approached. Hence, to capture all possible families of solutions we have performed an extensive set of numerical simulations with 5 initial film thicknesses, namely  $h_{initial} = 0.025, 0.05, 0.075, 0.1$  and  $0.125$  (see figure 7.5). Clearly in the absence of gravity in the flow direction multiple steady state solutions are observed in the range of  $Ca$  studied (see figure 7.6). To quantify the difference between different solution families we have chosen the film thickness as the characteristics parameter. Steady state value of this parameter in the absence of gravity as a function of  $Ca$  is shown in figure 7.7. Clearly, significant hysteric behavior in the film thickness as a function of  $Ca$  is observed at  $Ca \approx 1.0$ . Moreover, at any given  $Ca$  the film thickness obtained via continuously ramping up the  $Ca$  is larger than those obtained with a continuous ramping down of the  $Ca$ , i.e. starting the simulation at a high  $Ca$ . Overall, there are two distinct branches of solution at high and low  $Ca$ , however the  $Ca$  dependence of the film thickness exhibits complex behavior at  $Ca \approx 1$  due to aforementioned solution bifurcations. It should also be noted that the interface shapes are significantly different for the two solution families (see figure 7.6). Specifically, for the case where we observe sharp interfaces the film thickness variations are a direct consequence of the interface shape in the Capillary transition region while in the case where the interface has a smooth shape, the film thickness is mainly determined by the initial film thickness.

Introducing gravity in the flow direction causes different branches of solution to collapse into a single solution for the interface shape and hence a single film thickness as a function of  $Ca$  is obtained (see figure 7.8). This is due to the fact that with the gravity in the flow direction, the interface shape is no longer mainly determined by the Capillary pressure as gravitational forces favor the solution with the sharp

interface shape. To shed some light into the mechanism by which gravity influences the flow, we have carefully examined the influence of gravity on the interface shape and normal forces along the free surface at various  $Ca$  (see figure 7.9 for the results at  $Ca = 1.0$ ). Overall, gravity tends to pull liquid out of the thin film region which leads to development of a significant normal stresses boundary layer on the free surface near the tip of the bubble (see figure 7.9). In turn this effect leads to formation of a sharp interface. Consequently solution family with sharper interface is favored in presence of gravity in the flow direction. In fact, between the two branches of solutions, the force balance at the free surface in the one obtained with the small film thickness on the substrate as the initial guess is much more similar to the solutions obtained with finite  $Bo$ . This is due to the fact that with a small initial film thickness on the substrate "viscous effects" are much higher when the plate is plunged in the liquid bath, consequently the normal stress boundary layer which forms near the air interface is similar to that observed in finite  $Bo$  simulations.

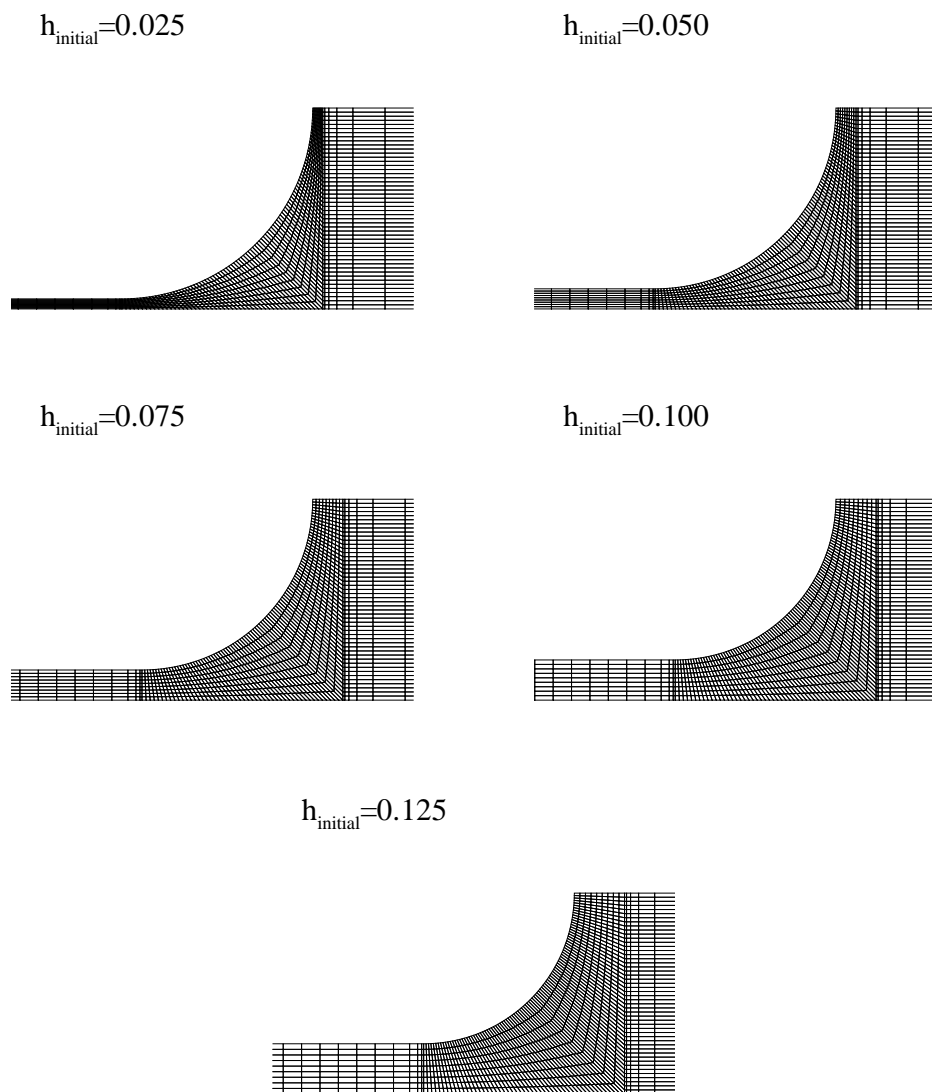


**Figure 7.5:** The computational domain near the air-liquid interface for the meshes used as the initial guess for the simulation.

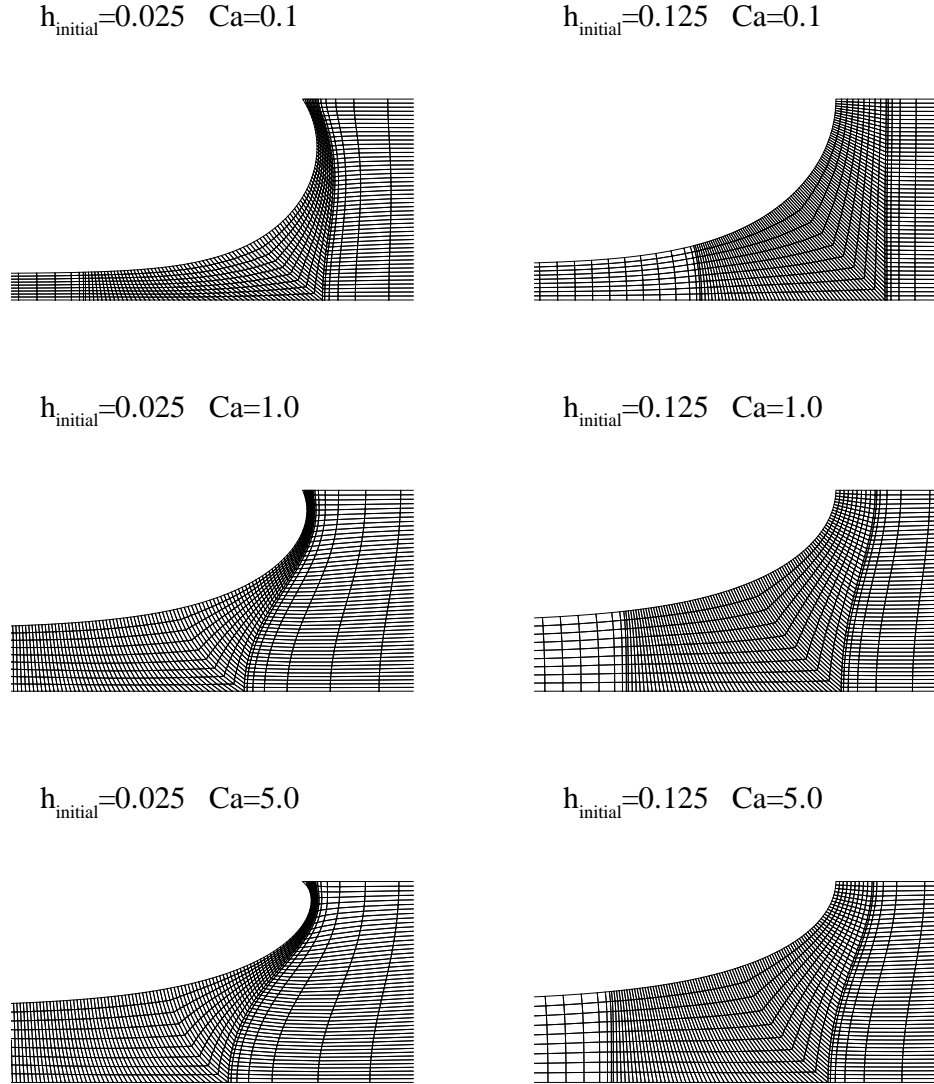


**Figure 7.6:** The interface shape near the air-liquid interface in the two steady state solution families (i.e. sharp and smooth curve) observed in the absence of gravity in the flow direction.

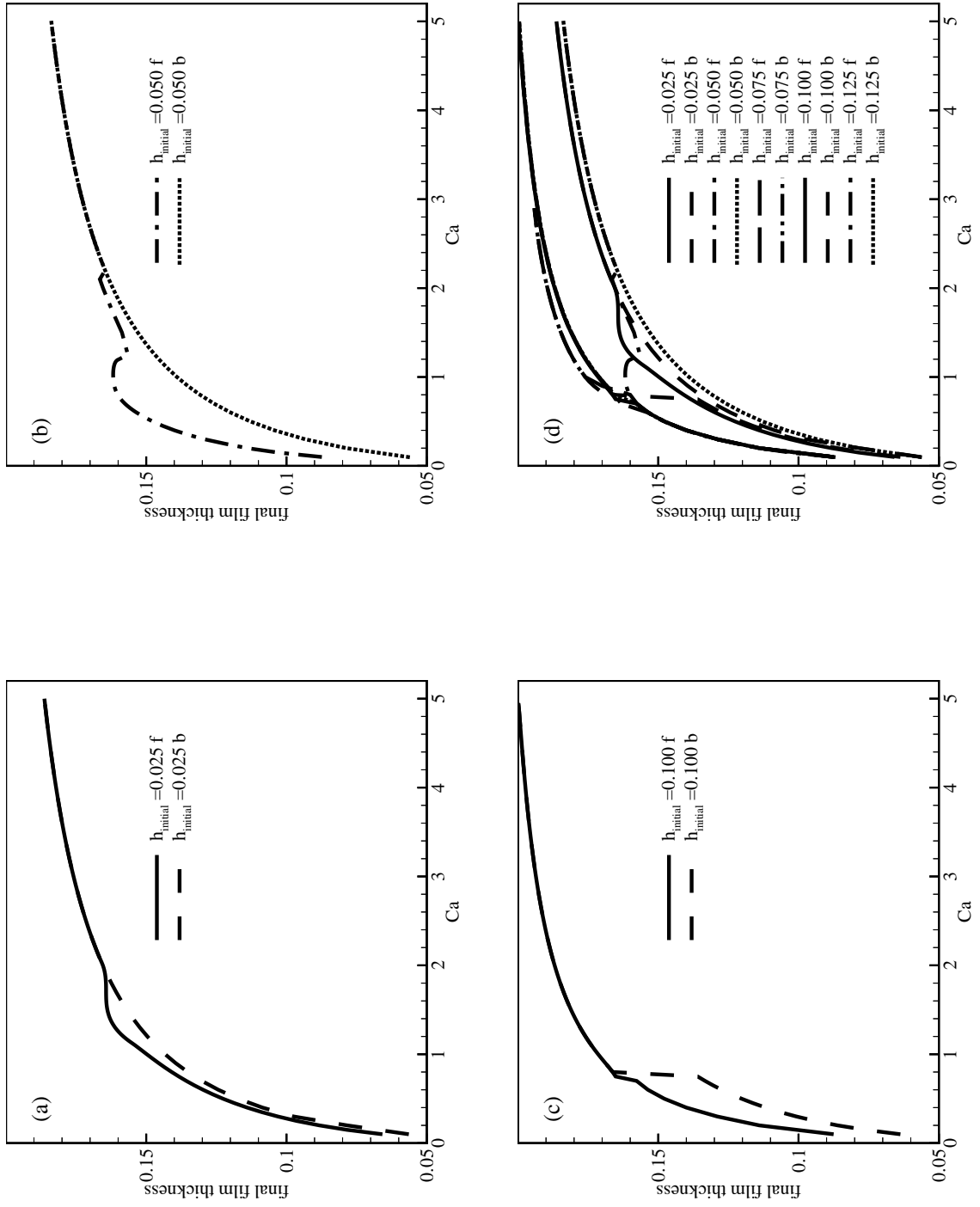


**Figure 7.7:** Film thickness as a function of  $Ca$  predicted from various initial guesses. f means that the solution was calculated with a positive step in  $Ca$  and b means the opposite.

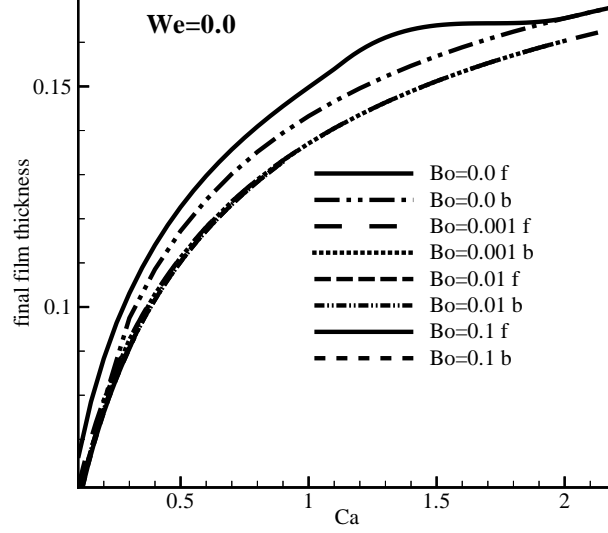


**Figure 7.8:** Film thickness as a function of  $Ca$  predicted by mesh with  $h_{initial} = 0.025$ . f means that the solution was calculated with a positive step in  $Ca$  and b means the opposite.

## Experimental results

As mentioned earlier the experiment apparatus is designed to allow precise control of cylinder eccentricity and the rotation speed of each cylinder. The entire set up can be rotated 90 degrees which allows investigation of the effect of gravity on flow properties (i.e. both in the flow direction and perpendicular to it, see figure 7.10). In addition, the initial film thickness on the wetted wall can be controlled by changing the eccentricity between cylinders at a desired  $Ca$ . This is due to the fact that the film thickness on the substrate plunging in the liquid bath is determined by the film thickness in the front of the cylinder and earlier studies have shown that the film thickness in the front of the coater will increase with a decrease in  $b$  (width of the channel at the meniscus) at a constant  $Ca$  [Lee et al. (2005)]. It should also be noted that even though the film thicknesses on both cylinders in the front are equal, the film thickness on the inner cylinder in the back of the coater is larger than the one on

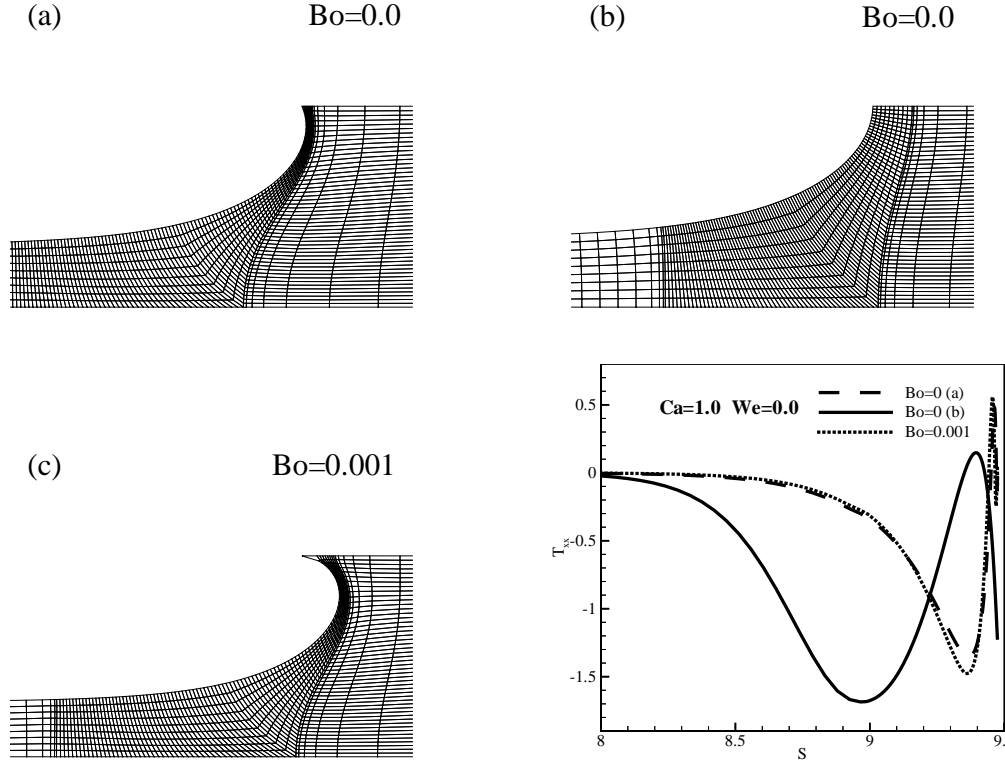


**Figure 7.9:** The interface shape near the air-liquid interface at  $Ca = 1.0$  with and without inclusion of gravitational force in the flow direction. The line plot shows the normal forces along the free surface for three cases whose interface have been shown in parts a to c.

the outer cylinder as the liquid on the outer cylinder drains easier compared to inner cylinder. All the experiments reported in this section have been performed with a Newtonian fluid at 6 different eccentricity, both with the vertical and horizontal device setup modes (see 7.11). In all experiments the interface shapes have been recorded using the image of the cross section of the flow generated via a laser sheet (see figure 7.12 for a sample laser).

The interface shapes at various  $Ca$  for representative eccentricities have been depicted in figure 7.13. Two general classes of air-liquid interface shapes (i.e. sharp or smooth curve) are observed depending on the direction of the gravity. Specifically, when the gravity is in the flow direction, only sharp interfaces are observed and the interface gets sharper with increasing  $Ca$ . However, when the gravity is perpendicular to the flow direction, both sharp and smooth interface shapes are observed. For instance at  $b/R_1 = 0.27$  and  $b/R_1 = 0.14$  (see figure 7.13-(b)) and  $Ca \approx 8.0$ , the air-liquid interface shapes at similar azimuthal positions are significantly different. The difference between these two experiments is the initial thickness of the liquid film on the wet substrate before plunging in the liquid. Consequently, with slight change in the initial parameters of the wet plunging flow, significant changes occur in the interface shapes at this  $Ca$ . This suggests the existence of multiple steady state interface shapes in the absence of gravity in the flow direction which is consistent with our simulation results discussed earlier. It should also be noted that for large eccentricity and in the vertical setup mode, where the gap width between the cylinders is very small ( $b/R_1 = 0.06$ ), a different trend in the evolution of the interface shape as a function of  $Ca$  is observed. Specifically, the air-liquid interfaces form at similar azimuthal positions around the cylinder for all ranges of  $Ca$ . This is due to large lubrication pressure formed in the small gap region which pushes the air-liquid interface back.

Clearly the interface shapes observed experimentally are somewhat sharper than their numerical counterparts. This is due to the fact that with current formulation the equations can be solved only for small  $Bo$ , i.e.  $Bo \approx 0.001$  to  $Bo \approx 0.1$ , which is much

smaller than the experimental  $Bo$ , i.e.  $Bo \approx 10$ . As mentioned before gravitational forces tend to make the interface shaper due to formation of significant normal stress boundary layer near the tip of the bubble and that is why the experimental interfaces are much sharper. In order to do a one-to-one comparison between simulation results and experimental measurements, the simulations should be continued to higher  $Bo$ . To accomplish this task one needs to rescale the equations with the Capillary length instead of gap width as it was done for dip coating flow (see previous chapter for more details) as well as using much more refined meshes to capture the steep normal stress boundary layers formed at high  $Bo$ .

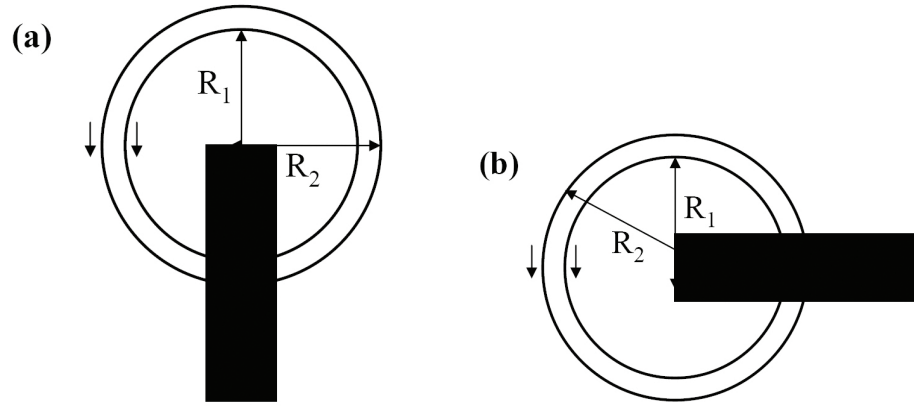


**Figure 7.10:** Schematic view of two positions of the eccentric coater, i.e. (a) horizontal and (b) vertical .

### 7.4.2 Effect of fluid elasticity

In this section preliminary numerical simulations of the influence of fluid elasticity on the interfacial dynamics of the wet plunging flow are presented. Specifically, the interface shape and resulting film thickness as a function of  $We$  are depicted in figures 7.14 and 7.15. In contrast to the Newtonian flow at  $Ca = 1.0$  and  $Bo = 0.0$  in addition to the stagnation point at the tip of the bubble, another stagnation point in the Capillary transition region is observed. This stagnation point continuously migrates

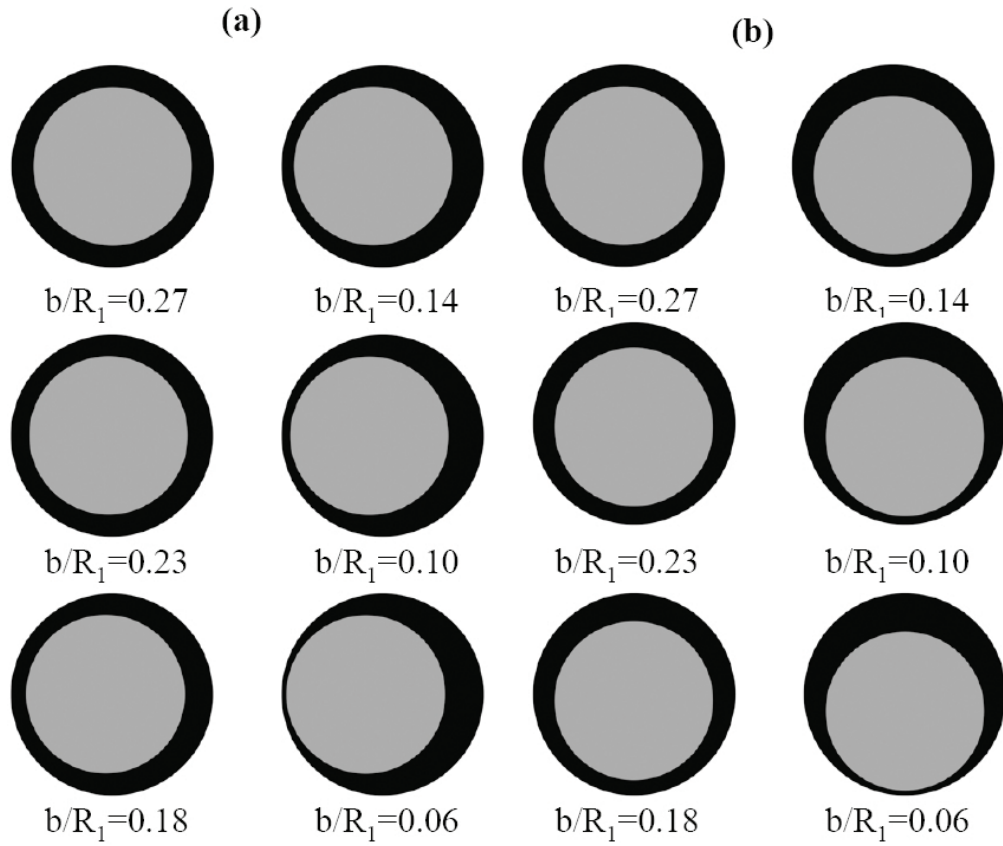


**Figure 7.11:** Schematic view of eccentricities examined at (a) the horizontal and (b) the vertical positions.

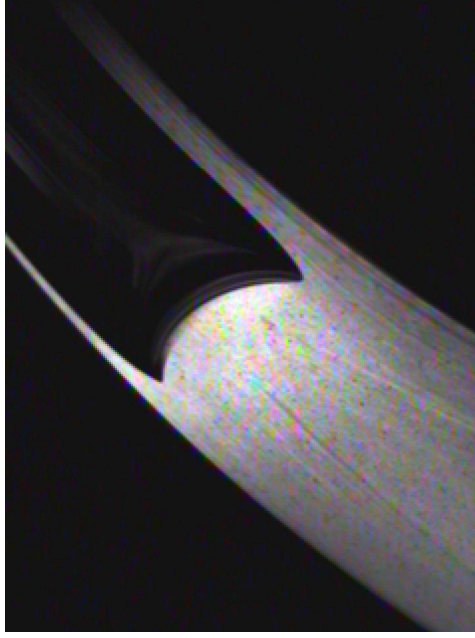


**Figure 7.12:** The air-liquid interface shape recorded by a laser sheet at  $Ca = 1.0$ .

towards the plane of symmetry as  $We$  is increased. There is also a recirculation region between these two stagnation points whose strength decreases with an increase in  $We$ . Clearly fluid elasticity leads to sharper interfaces near the plane of symmetry and significant modification of the interface shape (in comparison to the Newtonian flow) is observed in capillary transition region at high  $We$ .

The variation in the film thickness as a function of  $We$  has also been examined and typical results are depicted in figure 7.16-(a) for  $Ca = 0.7$  and  $Ca = 1.0$ . Elasticity at both  $Ca$  has a film thinning effect due to the presence of positive normal stresses in the flow direction, i.e.  $\partial\tau_{xx}/\partial x > 0$ , that pulls liquid out of the thin film region (see figure 7.17). Consequently, fluid elasticity leads to formation of a normal stress boundary layers near the air interface similar to those observed for Newtonian fluids at finite  $Bo$  (see figure 7.16-(b)). It should also be noted that fluid elasticity influences the wet plunging flow in a different manner than the dip coating flow where there is a film thinning effect for weakly elastic solutions followed by thickening effect at higher  $We$ . In order to investigate the possibility of formation of multiple steady



**Figure 7.13:** The shape of air-liquid interface at different eccentricities at (a) the horizontal and (b) the vertical positions. The interface shapes have been depicted at the azimuthal positions around the cylinder that they are formed and if several interfaces are formed at the similar angles, they have been shown side by side.

state solutions and the effect of gravity on it in the case of viscoelastic fluids, more simulations at finite  $Bo$  and over a wide range of  $Ca$  and  $We$  is required, however we believe that due to formation of the normal stress boundary layer near the air interface, existence of different solution branches is highly unlikely even at relatively small  $We$  (see figure 7.16-(b)).

## 7.5 Conclusion

The flow properties near the air-liquid interface on the back of an eccentric-cylinder coating device, where a wet substrate is plunged into a liquid bath, has been investigated. It has been shown both numerically and experimentally that for Newtonian fluids, two major branches of steady state solution exist in the absence of gravity in the flow direction. It is also shown numerically that fluid elasticity has a film thinning effect in the wet plunging flow for all ranges of  $We$ . In order to comprehensively investigate the fluid elasticity effects on interfacial dynamics of the wet plunging flow, simulations over a broad range of  $We$  and  $Bo$  need to be performed. In turn, the simulation results should be compared with the wet plunging flow experiments at least with several Boger fluids with elasticity number, i.e.  $N = We/Ca$ , ranging from 0.2 to 2.0.

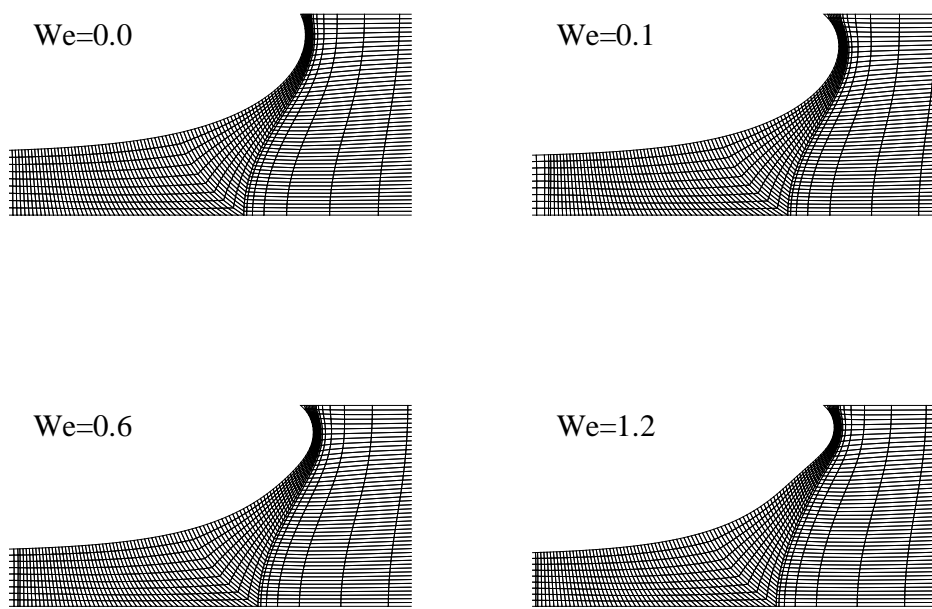


**Figure 7.14:** The interface shape near the air-liquid interface at  $Ca = 1.0$ .

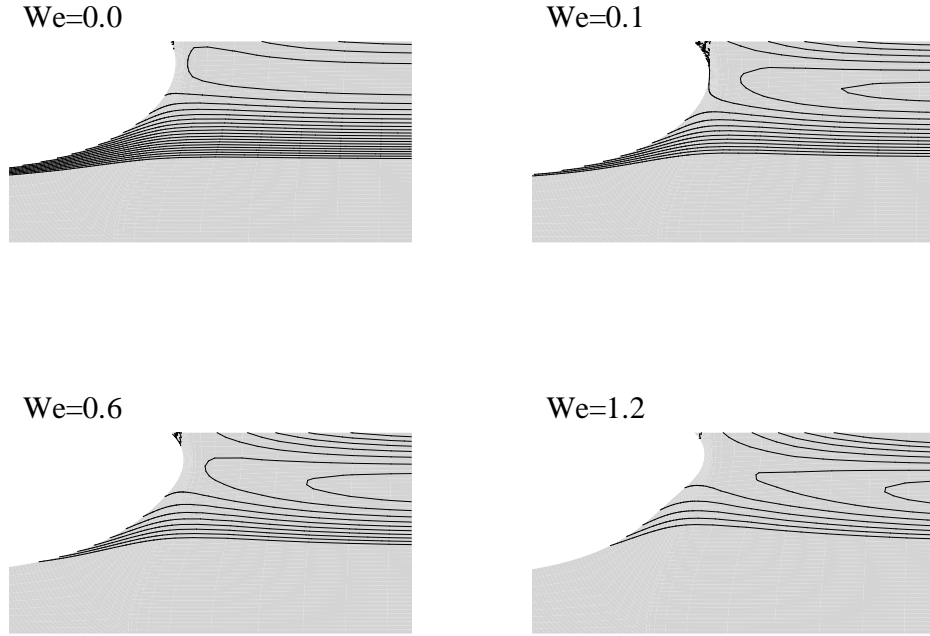


**Figure 7.15:** The streamlines near the air-liquid interface at  $Ca = 1.0$ .

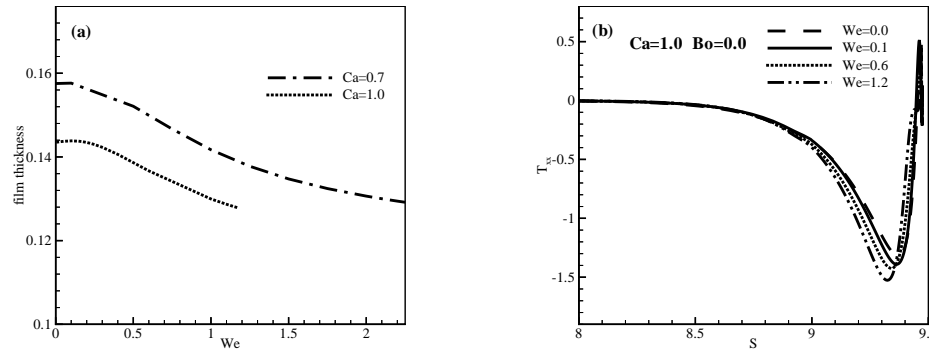


**Figure 7.16:** (a) Film thickness as a function of  $We$ , (b) the normal forces along the free surface.

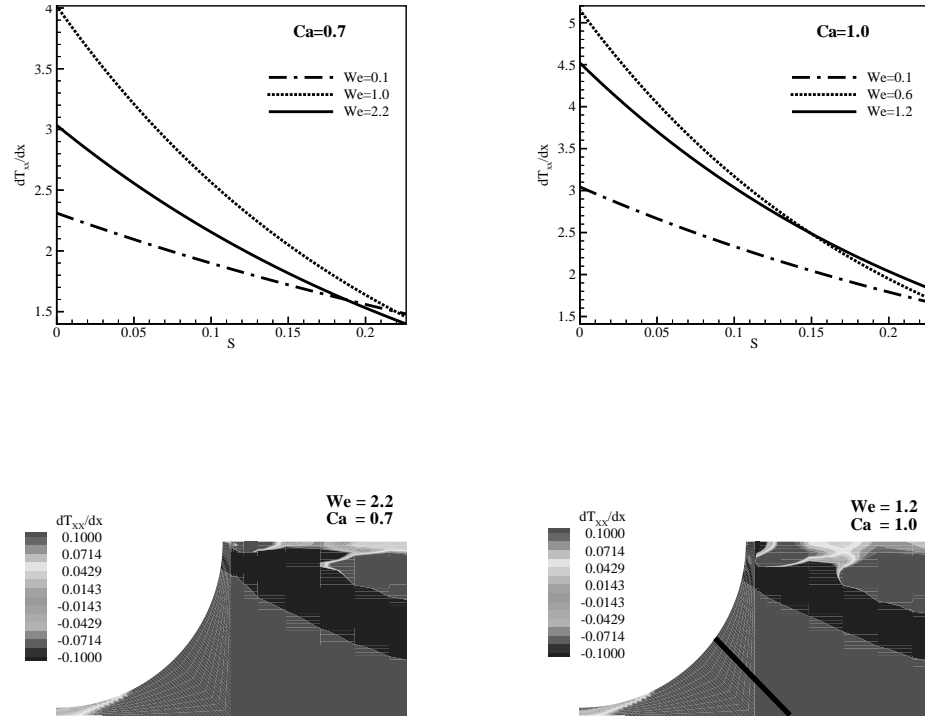


**Figure 7.17:** Line and contour plots of stress gradient, i.e.  $\partial\tau_{xx}/\partial x$ . The line plots are along the line shown in the last contour plot, where zero is on the wall.

# Chapter 8

## Summary and future work

In order to develop a quantitative understanding of the flow-micro-structure coupling mechanisms in viscoelastic polymeric fluids and in turn predict, consistent with experiments, their essential macroscopic flow properties e.g. frictional drag, interface shape, etc., extensive continuum and multiscale flow simulations in several industrially relevant bulk and free surface flows have been performed. The primary motivation for the selection of the specific flow problems is based on their ability to represent different deformation types, and the ability to experimentally verify the simulation results as well as their scientific and industrial significance. Specifically, finite element simulations of a well characterized branched low density polyethylene melt in a lubricated cross-slot channel geometry have been performed for a wide range of  $We$ . The comparison between the 2D experimental and computed optical birefringence data shows that the multimode Giesekus model can accurately predict the flow characteristics at moderate  $We$  in the region of the flow cell of mixed kinematics. However, the model predictions at large  $We$  ( $We = 29$ ) remain qualitative in the channel outlet. In particular, experimental limitations in the stagnation region of the channel do not allow an effective assessment of the constitutive model performance. The experimental interpretation issues have been shown to mainly arise from multiple order of retardations within the laser beam diameter and oil film reflections occurring

close to the stagnation point. Ongoing work by our collaborators involves developing an improved experimental design and a better data analysis technique to try to solve the aforementioned issues [Sadati et al. (2010)].

We have also performed extensive continuum and multiscale flow simulations in two benchmark flow problems, namely sedimentation of sphere in a tube and flow past a cylinder in a channel, utilizing the FENE-P (continuum and BCF) and Giesekus (continuum) constitutive equations as well as the FENE (BCF) dumbbell micromechanical model to provide insight into the dependence of the upper  $We$  limit encountered in continuum level viscoelastic flow simulations with typical constitutive equations for dilute polymeric solutions that predict bounded extensional viscosities in geometries with internal stagnation points on solid surfaces. To this end, a strong correlation between significant contribution of over-stretched states to the total polymeric stress and existence of very large and localized polymeric stress gradients and divergence of numerical simulations in both benchmark problems with the FENE-P and Giesekus models for highly strain hardening has been established. The consequence of the over prediction of polymeric stresses and stress gradients by the FENE-P model in comparison to the FENE model on the kinematics in the wake of the solid objects has also been examined. In general, closed form constitutive equations can either give rise to very highly localized region of high strain rate or recirculation regions downstream of the object that are absent in the corresponding multiscale simulations with the FENE model. Hence, the accuracy of FENE-P model predictions at  $We$  and  $b$  values where a significant portion of the polymeric stress arises due to over-stretched states is questionable. Hence, regularization techniques for polymeric stresses should be used in FENE-P computation of flows with strong straining components.

Self-consistent multiscale flow simulations of a highly elastic dilute polymeric solution, described by first principles micromechanical models for sedimentation of a sphere in a tube filled with a dilute polymeric solution has been performed. Through comparisons with experimental measurements, we have demonstrated

that the evolution of the drag coefficient as a function of fluid elasticity can be accurately predicted when the macromolecular dynamics is described by realistic micromechanical models that closely capture the transient extensional viscosity of the experimental fluid at high extension rates. Specifically, for the first time we have computed the drag coefficient on the sphere at high  $We$  with multi-segment bead-spring chain models with appropriate molecular parameters and have demonstrated that this class of high fidelity multiscale numerical simulation is not only capable of describing the drag on the sphere as a function of  $We$  at various sphere to tube diameter ratios quantitatively but also it can faithfully reproduce the experimentally measured velocity and stresses in the wake of the sphere.

We have also performed numerical simulations to elucidate the effects of elasticity on the interfacial dynamics of dip coating flows. Specifically, we have shown that the film thickness scaled with the capillary length, as a function of  $We$ , at low  $Ca$  and high  $Bo$  collapses onto a single curve, and agrees with the Ro and Homsy [Ro and Homsy (1995)] correlation for small values of  $We$ . For a fixed  $Ca$  and  $We$ , an increase in  $Bo$  results in a decrease in the film thickness, an increase in the size of the recirculation region and an increase in the strain rates subsequently leading to an increase in the normal stresses. At low  $We$ , there is a film thinning effect and as the value of  $We$  is increased, there is a film thickening effect that accompanies the formation of a normal stress boundary layer at the free surface in the capillary transition region. Both the magnitude of the film thickness and the maximum stress in the stress boundary layer increase with increasing  $We$ . Furthermore, the normal stress boundary layer at the free surface is a result of the local planar extensional flow at the interface. These calculations provide a simple way of examining the wealth of interfacial phenomena that are present in dip coating flows.

Finally, the flow properties near the air-liquid interface on the back of an eccentric-cylinder coating device, where a wet substrate is plunged into a liquid bath, has been investigated. It has been shown both numerically and experimentally that for Newtonian fluids, two major branches of steady state solution exist in the absence

of gravity in the flow direction. It is also shown numerically that fluid elasticity has a film thinning effect in the wet plunging flow for all ranges of  $We$ . In order to comprehensively investigate the fluid elasticity effects on interfacial dynamics of the wet plunging flow, simulations over a broad range of  $We$  and  $Bo$  need to be performed. In turn, the simulation results should be compared with the wet plunging flow experiments at least with several Boger fluids with elasticity number, i.e.  $N = We/Ca$ , ranging from 0.2 to 2.0.

# Bibliography

# Bibliography

- Abedijaberi, A., Bharata, G., Shaqfeh, E., and Khomami, B. (2011). A computational study of the influence of visco-elasticity on the interfacial dynamics of dip coating flow. J. Non-Newt. Fluid Mech. 123
- Abedijaberi, A. and Khomami, B. (2011). On the limitations of elastic dumbbell based constitutive equations in simulation of flow of dilute polymeric solutions with stagnation points. J. Non-Newt. Fluid Mech., 166:533–545. 2, 56, 58, 68
- Abedijaberi, A., Soulages, J., Kroger, M., and Khomami, B. (2008). Flow of branched polymer melts in a lubricated cross-slot channel: a combined computational and experimental study. Rheologica Acta, 48:97–108. 56
- Adachi, K., Spiers, R., and Wilkinson, W. (1978). Free coating of viscoelastic fluids onto a vertical vertical surface. J. Non-Newtonian Fluid Mech., 3:331–345. 86, 87, 123
- Arigo, M., Rajagopalan, D., Shapely, N., and McKinley, G. (1995). The sedimentation of a sphere through an elastic fluid: p. i - steady motion. J. Non-Newtonian Fluid Mech., 60:225–257. 32, 33, 34, 38, 56, 58, 60, 64, 67, 68, 69, 79
- Baaijens, F., Baaijens, H., Peters, G., and Meijer, H. (1994). An experimental and numerical investigation of a viscoelastic flow around a cylinder. J. Rheology, 38:351–376. 2, 33, 38, 56, 58, 64

- Baaijens, H., Peters, G., Baaijens, F., and Meijer, H. (1995). Viscoelastic flow past a confined cylinder of a polyisobutylene solution. J. Rheology, 39:1243–1277. 33, 38, 56, 58, 64, 80
- Bajaj, M., Pasquali, M., and Prakash, J. R. (2008). Coil-stretch transition and the breakdown of computations for viscoelastic fluid flow around a confined cylinder. J. Rheology, 52:197–223. 33, 34, 43
- BASF (2010). BASF Report 2010. 1
- Becherer, P., Morozov, A. N., and Saarloos, W. V. (2008). Scaling of singular structures in extensional flow of dilute polymer solutions. J. Non-Newtonian Fluid Mech., 153:183–190. 34
- Becherer, P., Saarloos, W. V., and Morozov, A. N. (2009). Stress singularities and the formation of birefringent strands in stagnation flows of dilute polymer solutions. J. Non-Newtonian Fluid Mech., 157:126–132. 34
- Beraudo, C., Fortin, A., Coupez, T., Y.Demay, B.Vergnes, and Agassant, J. (1998). A finite element method for computing the flow of multi-mode viscoelastic fluids: comparisons with experiments. J. Non-Newtonian Fluid Mech., 75:1. 2
- Bhatara, G., Shaqfeh, E., and Khomami, B. (2004a). Influence of viscoelasticity on the interfacial dynamics of air displacing fluid flows - a computational study. J. Non-Newtonian Fluid Mech., 122:313–332. 84, 85, 89, 94, 103, 104, 125
- Bhatara, G., Shaqfeh, E., and Khomami, B. (2004b). Influence of viscoelasticity on the interfacial dynamics of air displacing fluid flows-a computational study. J. Non-Newtonian Fluid Mech., 122:313. 33
- Bhatara, G., Shaqfeh, E., and Khomami, B. (2005a). The influence of polymer concentration and chain architecture on free surface displacement flows of polymeric liquids. J. Rheology, 49:929. 33

- Bhatara, G., Shaqfeh, E., and Khomami, B. (2005b). The influence of polymer concentration and chain architecture on free surface displacement flows of polymeric liquids. J. Rheology, 49:929–963. 84, 85, 103, 104
- Bhave, A., Menon, R., Armstrong, R., and Brown, R. (1993). A constitutive equation for liquid-crystalline polymer solutions. J. Rheology, 37:413–441. 35
- Bird, R., Dotson, P., and Johnson, N. (1980). Polymer solution rheology based on a finitely extensible bead-spring chain model. J. Non-Newtonian Fluid Mech., 7:213–235. 91
- Bird, R. B., Curtiss, C. F., Armstrong, R. C., and Hassager, O. (1987). Dynamics of polymeric liquids- Vol 2. Wiley, New York. 6, 7, 9, 13
- Boger, D. and Mackay, M. (1991). Continuum and molecular interpretation of ideal elastic fluids. J. Non-Newtonian Fluid Mech., 41:133–150. 91
- Bonn, D., Kellay, H., Braunlich, M., Amar, M. B., and Meunier, J. (1995). Viscous fingering in complex fluids. Physica A, 220:60–73. 83, 84
- Bretherton, F. (1961). The motion of long bubbles in tubes. J. Fluid Mech., 10:166–188. 83
- Brooks, A. and Hughes, T. (1982). Streamline upwind/ Petrov-galerkin formulations for convection dominated flows with particular emphasis on the incompressible Navier-Stokes equations. Comp. Methods Appl. Mech. Eng., 32:199–259. 11, 94
- Brown, R. A. (1979). The shape and stability of three-dimensional interfaces. PhD Thesis. 127
- Burghardt, W., Li, J., Yang, B., and Khomami, B. (1999a). Uniaxial extensional characterization of a shear thinning fluid using axisymmetric flow birefringence. J. Rheology, 43:147–165. 13, 15

- Burghardt, W., Li, J., Yang, B., and Khomami, B. (1999b). Uniaxial extensional characterization of a shear thinning fluid using axisymmetric flow birefringence. J. Rheology, 43:147–165. 56
- Cairncross, R., Schunk, P., Baer, T., Rao, R., and Sackinger, P. (2000). finite element method for free surface flows of incompressible fluids in three dimensions. part i. boundary fitted mesh motion. Int. J. Numer. Meth. Fluids, 33:375–403. 96
- Chilcott, M. and Rallison, J. (1988). Creeping flow of dilute polymer solutions past cylinders and spheres. J. Non-Newtonian Fluid Mech., 29:381–432. 7, 34, 91
- Coyle, D., Macosko, C., and Scriven, L. (1990). Reverse roll coating of non-newtonian liquids. J. Rheology, 34:615–628. 83
- Dealy, J. and Wissbrun, K. (1990). Melt rheology and its role in plastics processing. Theory and applications. Van Nostrand Reinhold, New York. 12
- Doyle, P., Shaqfeh, E., and Spiegelberg, G. (1998). Relaxation of dilute polymeric solutions following extensional flow. J. Non-Newtonian Fluid Mech., 76:79–110. 57, 72
- Esmail, M. and Hummel, R. (1975). Nonlinear theory of coating onto a free surface. AIChE J., 21:958–972. 86, 123
- Feigl, K. and Ottinger, H. (1996). A numerical study of the flow of a low-density-polyethylene melt in a planar contraction and comparison to experiments. J. Rheology, 40:21–35. 13
- Fuller, G. G. (1995). Optical rheometry of complex fluids. Oxford Univ. Press, Oxford. 14, 19
- Galante, S. (1991). An Investigation of Planar Entry Flow Using a High-Resolution Flow Birefringence Method. PhD Thesis, Carnegie-Mellon University. 19

- Gauri, V. and Koelling, K. (1999a). Gas-assisted displacement of viscoelastic fluids: flow dynamics at the bubble front. J. Non-Newtonian Fluid Mech., 83:183–203. 84
- Gauri, V. and Koelling, K. (1999b). The motion of long bubbles through viscoelastic fluids in capillary tubes. Rheologica Acta., 38:458–470. 84
- Ghosh, I., Joo, Y., McKinley, G., Brown, R., and Armstrong, R. (2002). A new model for dilute polymer solutions in flows with strong extensional components. J. Rheology, 46:1057–1089. 36
- Giavedoni, M. and Saita, F. (1997). The axisymmetric and plane cases of a gas phase steadily displacing a newtonian liquid - a simultaneous solution of the governing equations. Phys. Fluids, 8:2420–2428. 84
- Giesekus, H. (1982). A simple constitutive equation for polymer fluids based on the concept of deformation-dependent tensorial mobility. J. Non-Newtonian Fluid Mech., 11:69–109. 8
- Gigras, P. and Khomami, B. (2002). Adaptive configuration fields: a new multiscale simulation technique for reptation-based models with a stochastic strain measure and local variations of life span distribution. J. Non-Newtonian Fluid Mech., 108:99–122. 56
- Gilmore, T., Morgan, E., and Osborne, S. (2011). Advance statistics on gdp by industry for 2010. 1
- Grillet, A., Lee, A., and Shaqfeh, E. (1999a). Observation of ribbing instabilities in elastic fluid flows with gravity stabilization. J. Fluid Mech., 399:49–83. 91
- Grillet, A., Yang, B., Khomami, B., and Sahqfeh, E. (1999b). Modeling of viscoelastic lid driven cavity flow using finite element simulations. J. Non-Newtonian Fluid Mech., 88:99–131. 32, 56

- Guenette, R. and Fortin, M. (1995). A new mixed finite element method for computing viscoelastic flows. J. Non-Newtonian Fluid Mech., 60:27–42. 94, 95
- Gupta, V. K., Sureshkumar, R., and Khomami, B. (2004). Polymer chain dynamics in newtonian and viscoelastic turbulent channel flows. Physics of Fluids, 16:1546–1566. 2, 44
- Gutfinger, C. and Tallmadge, J. (1965). Films of non-newtonian fluids adhering to flat plates. AIChE J., 11:403–418. 86
- Halin, P., Lielens, G., Keunings, R., and Legat, V. (1998). The lagrangian particle method for macroscopic and micro-macro viscoelastic flow computations. J. Non-Newtonian Fluid Mech., 77:153–190. 56
- Happel, J. and Brenner, H. (1973). Low Reynolds Number Hydrodynamics. Martinus Nijhoff, Dordrecht. 65, 67
- Harlen, O. G., Rallison, J. M., and Chilcott, M. D. (1990). High-deborah-number flow of a dilute polymer solution past a sphere falling along the axis of a cylindrical tube. J. Non-Newtonian Fluid Mech., 33:157–173. 38, 64
- Hulsen, M., Fattal, R., and Kupferman, R. (2005). Flow of viscoelastic fluids past a cylinder at high weissenberg number: Stabilized simulations using matrix logarithms. J. Non-Newtonian Fluid Mech., 127:27–39. 35
- Hulsen, M., van Heel, A., and van den Brule, B. (1997). Simulation of viscoelastic flows using brownian configuration fields. J. Non-Newtonian Fluid Mech., 70:79–101. 9, 35, 56
- Hung, H., Gubbins, K., and Franzen, S. (2004). A graduate course on multi-scale modeling of soft matter. Chem. Eng. Education, 38:242. 3
- Huzyak, P. and Koelling, K. (1997). The penetration of a long bubble through a viscoelastic fluid in a tube. J. Non-Newtonian Fluid Mech., 71:73–88. 84, 91

- Janeschitz-Kriegl, H. (1983). Polymer melt rheology and flow birefringence, from the series Polymers, properties and applications. Springer, Berlin. 20
- Keunings, R. (1997). On the peterlin approximation for finitely extensible dumbbells. J. Non-Newtonian Fluid Mech., 68:85–100. 2, 36, 44
- Keunings, R. (2001). Advances in the computer modeling of the flow of polymeric liquids. Comput. Fluid Dyn. J., 9:449–458. 12
- Khomami, B., Talwar, K., and Ganpule, H. (1994). A comparative study of higher and lower order finite element techniques for computation of viscoelastic flows. J. Rheology, 38:255–289. 10, 94
- Kommu, S., Khomami, B., and Kardos, J. (1998). Modeling of injected pultrusion processes, a numerical approach. Polym. Composite, 19:335. 2
- Koppol, A., Sureshkumar, R., Abedijaberi, A., and Khomami, B. (2009). Anomalous pressure drop behaviour of mixed kinematics flows of viscoelastic polymer solutions: a multiscale simulation approach. J. of Fluid Mechanics, 631:231–253. 35, 38, 41, 56, 57, 61, 64
- Koppol, A. P., Sureshkumar, R., and Khomami, B. (2007). An efficient algorithm for multiscale flow simulation of dilute polymeric solutions using bead-spring chains. J. Non-Newtonian Fluid Mech., 141:180–192. 10, 61
- Kroger, M. (2004). Simple models for complex nonequilibrium fluids. Phys. Rep., 390:453. 20
- Kroger, M., Luap, C., and Muller, R. (1997). Polymer melts under uniaxial elongational flow: stress-optical behavior from experiments and nemd computer simulations. Macromolecules, 30:526. 20
- Landau, L. and Levich, B. (1942). Acta Physchim, 17:41–53. 86, 87, 123

- Larson, R. (2005). The rheology of dilute solutions of flexible polymers: progress and problems. J. Rheology, 49:1–70. 57, 72
- Laso, M. and Ottinger, H. (1993). Calculation of viscoelastic flow using molecular models: the connfessit approach. J. Non-Newtonian Fluid Mech., 47:1–20. 35, 56
- Lee, A., Shaqfeh, E., and Khomami, B. (2002). A study of viscoelastic free surface flows by the finite element method: Heleshaw and slot coating flows. J. Non-Newtonian Fluid Mech., 108:327–362. 32, 33, 84, 85, 91, 93, 94, 96, 97, 98, 99
- Lee, A., Shaqfeh, E., and Khomami, B. (2005). Viscoelastic effects on interfacial dynamics in air-fluid displacement under gravity stabilization. J. Fluid Mech., 531:59. 33, 84, 85, 98, 103, 122, 123, 125, 133
- Li, C., Sureshkumar, R., and Khomami, B. (2006). Influence of rheological parameters on polymer induced turbulent drag reduction. J. Non-Newtonian Fluid Mech., 140:23–40. 41
- Li, J., Burghardt, W., Yang, B., and Khomami, B. (1998). Flow birefringence and computational studies of a shear thinning polymer solution in axisymmetric stagnation flow. J. Non-Newtonian Fluid Mech., 74:151–193. 13, 15, 33, 56, 62
- Li, J., Burghardt, W., Yang, B., and Khomami, B. (2000). Birefringence and computational studies of a polystyrene boger fluid in axisymmetric stagnation flow. J. Non-Newtonian Fluid Mech., 91:189–220. 13, 15, 33, 56, 62
- Lielens, G., part Halin, and Jaumain, I. (1998). New closure approximations for the kinetic theory of finitely extensible dumbbells. J. Non-Newtonian Fluid Mech., 76:249–279. 36
- Linder, A., Bonn, D., Poire, E. C., Amar, M., and Meunier, J. (2002). Viscous fingering in non-newtonian fluids. J. Fluid Mech., 496:237–256. 84

- Luap, C., Karlina, M., Schweizer, T., and Venerus, D. (2006). Limit of validity of the stress-optical rule for polystyrene melts: Influence of polydispersity. J. Non-Newtonian Fluid Mech., 138:197–203. 20
- Luap, C., Muller, C., Schweizer, T., and Venerus, D. (2005). Simultaneous stress and birefringence measurements during uniaxial elongation of polystyrene melts with narrow molecular weight distribution. Rheol. Acta, 45:83–91. 20
- Lunsmann, W., Geniser, L., Brown, R., and Armstrong, R. (1993). Finite element analysis of steady viscoelastic flow around a sphere: calculations with constant viscosity models. J. Non-Newtonian Fluid Mech., 48:63–99. 56, 58, 68
- Mangoubi, C., Hulsen, M., and Kupferman, R. (2009). Numerical stability of the method of brownian configuration fields. J. Non-Newtonian Fluid Mech., 157:188–196. 35
- Maroudas, D. (2000). Multiscale modeling of hard materials: challenges and opportunities for chemical engineering. AIChE. J., 46:878. 3
- McHugh, A., Mackay, M. E., and Khomami, B. (1987). Measurement of birefringence by the method of isoclinics. J. Rheology, 31:619–634. 15
- McKinley, G. (2001). Transport Processes in Bubbles, Drops and Particles. Taylor & Francis. 56, 58, 68, 69, 79
- McKinley, G., Armstrong, R., and Brown, R. (1993). The wake instability in viscoelastic flow past confined circular cylinders. Phil. Trans. R. Soc. Lond. A, 344:265–304. 61, 68
- Milliken, W. and Leal, L. (1991). Deformation and breakup of viscoelastic drops in planar extensional flows. J. Non-Newtonian Fluid Mech., 40:355–379. 32

- Mysels, K. and Frankel, S. (1978). The effect of a surface-induced gradual viscosity increase upon the thickness of entrained liquid films and the flow in narrow channels. J. Colloid Int. Sc., 66:166–172. 87
- Nieminen, R. (2002). From atomistic simulation towards multiscale modeling of materials. J. Phys.: Condens. Matter, 14:2859. 3
- Ottinger, H. (1999). Letter to the editor: End effects in flow-birefringence experiments for polymer melts. J. Rheology, 43:253. 15
- Ottinger, H., van den Brule, B. H. A. A., and Hulsen, M. A. (1997). Brownian configuration fields and variance reduce conffessit. J. Non-Newtonian Fluid Mech., 70:255–261. 56
- Pasquali, M. and Scriven, L. (2002). Free surface flows of polymer solutions with models based on the conformation tensor. J. Non-Newtonian Fluid Mech., 108:363–409. 84
- Pearson, J. (1959). The instability of uniform viscous flow under rollers and spreaders. J. Fluid Mech., 7:481–500. 83
- Perkins, T., Smith, D., and Chu, S. (1997). Single polymer dynamics in an elongational flow. Science, 276:2016–2021. 56
- Peters, G., Schoonen, J., Baaijens, H., and Meijer, H. (1999). On the performance of enhanced constitutive models for polymer melts in a cross-slot flow. J. Non-Newtonian Fluid Mech., 82:387–427. 13
- Pitts, E. and Greiller, J. (1961). The flow of thin films between rollers. J. Fluid Mech., 11:33–50. 83
- Poslinski, A., Oehler, P., and Stokes, V. (1995). Isothermal gas-assisted displacement of viscoplastic liquids in tubes. Polym. Eng. Sci., 35:877–892. 83

- Quinzani, L., Armstrong, R., and Brown, R. (1994). Birefringence and laser-doppler velocimetry (ldv) studies of viscoelastic flow through a planar contraction. J. Non-Newtonian Fluid Mech., 52:1–36. 55
- R. Fattal, R. K. (2004). Constitutive laws for the matrix-logarithm of the conformation tensor. J. Non-Newtonian Fluid Mech., 123:281–285. 34
- R. Fattal, R. K. (2005). Time-dependent simulation of viscoelastic flows at high weissenberg number using the log-conformation representation. J. Non-Newtonian Fluid Mech., 126:23–37. 34
- Rabaud, M., Michalland, S., and Couder, Y. (1990). Dynamical regimes of directional viscous fingering - spatiotemporal chaos and wave- propogation. Phys. Rev. Letters, 64:184–187. 83
- Rajagopalan, D., Byars, J., Armstrong, R., Brown, R., Lee, J., and Fuller, G. (1992). Comparison of numerical simulations and birefringence measurements in viscoelastic flow between eccentric rotating cylinders. J. Rheology, 36:1349–1375. 20
- Rallison, J. and Hinch, E. (1988). Do we understand the physics in the constitutive equation? J. Non-Newtonian Fluid Mech., 29:37–55. 33
- Rasmussen, H. and Hassager, O. (1996). On the sedimentation velocity of spheres in a polymeric liquid. Chem. Eng. Sci., 51:1431–1440. 56, 58, 68
- Reinelt, D. and Saffman, P. (1985). The penetration of a finger into a viscous fluid into a channel and tube. SIAM J. Sci. Stat. Comput., 6:542–561. 93
- Renardy, M. (2006). A comment on smoothness of viscoelastic stresses. J. Non-Newtonian Fluid Mech., 138:204–205. 33

- Ro, J. and Homsy, G. (1995). Viscoelastic free surface flows: thin film hydrodynamics of hele-shae and dip coating flows. J. Non-Newtonian Fluid Mech., 57:203–225. 85, 87, 99, 114, 146
- Romero, O., Suszynski, W., Scriven, L., and Carvalho, M. (2004). Low-flow limit in slot coating of dilute solutions of high molecular weight polymer. J. Non-Newtonian Fluid Mech., 118:137–156. 85
- Rothstein, J. and McKinley, G. (1999). Extensional flow of a polystyrene boger fluid through a 4:1:4 contraction/expansion. J. Non-Newtonian Fluid Mech., 86:61–88. 56, 57
- Rothstein, J. and McKinley, G. (2001). The axisymmetric contraction-expansion: the role of extensional rheology on vortex growth dynamics and the enhanced pressure drop. J. Non-Newtonian Fluid Mech., 98:33–63. 56, 57
- Ruschak, K. (1985). Coating flows. Annu. Rev. Fluid Mech., 17:65–89. 83, 84
- Sackinger, P., Schunk, P., and Rao, R. (1996). A newton-rhapson pseudo-solid domain mapping technique for free and moving boundary problems : a finite elementimplementation. J. Comput. Phys., 125:83–103. 95, 96, 97
- Sadati, M., Luap, C., Krger, M., Gusev, A., and Ottinger, H. (2010). Smooth full field reconstruction of velocity and its gradients from noisy scattered velocimetry data in a cross-slot flow. J. Rheology, 55:353. 145
- Saffman, P. and Taylor, G. (1958). The penetration of a fluid into a porous medium or hele-shaw cell containing a more viscous fluid. Proc. R. Soc. London, Ser. A, 245:312. 83
- Satrape, J. and Crochet, M. (1994). Numerical simulation of the motion of a sphere in a boger fluid. J. Non-Newtonian Fluid Mech., 55:91–111. 56, 58, 68

- Schoonen, J., Swartjes, F., Peters, G., , Baaijens, F., and Meijer, H. (1998). A 3d numerical/experimental study on a stagnation flow of a polyisobutylene solution. J. Non-Newtonian Fluid Mech., 79:529–561. 2, 13
- Shaqfeh, E. (2005). The dynamics of single-molecule dna in flow. J. Non-Newtonian Fluid Mech., 130:1–28. 57, 72
- Somasi, M. (2001). Dynamics of polymeric fluids, a combined brownian dynamics finite element approach. PhD Thesis, Washington University in St. Louis. 58
- Somasi, M. and Khomami, B. (2000). Linear stability and dynamics of viscoelastic flows using time-dependent stochastic simulation techniques. J. Non-Newtonian Fluid Mech., 93:339–362. 9, 33, 56, 57
- Somasi, M. and Khomami, B. (2001). A new approach for studying the hydrodynamic stability of fluids with microstructure. Physics of fluids, 13:1811–1814. 33, 56, 57
- Somasi, M., Khomami, B., Woo, N., Hur, J., and Shaqfeh, J. (2002). Brownian dynamics simulations of bead-rod and bead-spring chains: numerical algorithms and coarse-graining issues. J. Non-Newtonian Fluid Mech., 108:227–255. 10, 38, 61, 64
- Soulages, J. (2007). Flow Birefringence and Velocity Measurements for Polymer Melts in a Cross-Slot Flow Channel. PhD Thesis, ETH Zurich. 14, 19, 20
- Soulages, J., Schweizer, T., Venerus, D., Hostettler, J., Mettler, F., Kroger, M., and Ottinger, H. (2008). Lubricated optical rheometer for the study of two-dimensional complex flows of polymer melts. J. Non-Newtonian Fluid Mech., 150:43–55. 15, 18
- Spiers, R., Subbaraman, C., and Wilkinson, W. (1975). Free coating of non-newtonian liquids onto a vertical surface. Chem. Eng. Sci., 30:379–395. 86
- Sullivan, T. and Middleman, S. (1979). Roll coating in the presence of a fixed constraining boundary. Chem. Eng. Commun., 3:469–482. 83

Szabo, B. and Babuska, I. (1987). Finite element analysis. John Wiley and Sons Inc.

11

Szady, M., Salamon, T., Liu, A., Bornside, D., Armstrong, R., and Brown, R. (1995).

A new mixed finite element method for viscoelastic flows governed by differential constitutive equations. J. Non-Newtonian Fluid Mech., 59:215–243. 10, 94

Talwar, K., Ganpule, H., and Khomami, B. (1994). A note on the selection of spaces in computation of viscoelastic flows using the hp-finite element method.

J. Non-Newtonian Fluid Mech., 52:293–307. 10, 62, 94

Talwar, K. and Khomami, B. (1992). Application of higher order finite element methods to viscoelastic flow in porous media. J. Rheology, 36:1977–1416. 10, 17,

62, 94

Talwar, K. and Khomami, B. (1995). Higher order finite element techniques for viscoelastic flow problems with change of type. J. Non-Newtonian Fluid Mech.,

59:49–72. 56

Taylor, G. (1960). Deposition of a viscous fluid on the walls of a tube. J. Fluid Mech.,

10:161–165. 83

Thayer, A. (1990). Advanced polymer composites tailored for aerospace use. Chemical and Engineering News, 68:37–57. 1

Tiefenbruck, G. and Leal, L. (1982). Deformation and breakup of viscoelastic drops in planar extensional flows. J. Non-Newtonian Fluid Mech., 10:115. 32

Venerus, D., Zhu, S., and Ottinger, H. (1999). Stress and birefringence measurements during the uniaxial elongation of polystyrene melts. J. Rheology, 43:795–813. 20

Venkataramani, V., Sureshkumar, R., and Khomami, B. (2008a). Coarse-grained modeling of macromolecular solutions using a configuration-based approach. J. Rheology, 52:1143. 57, 80

- Venkataramani, V., Sureshkumar, R., and Khomami, B. (2008b). A computationally efficient approach for hi fidelity fine graining from bead-spring models to bead-rod models. J. Non-Newtonian Fluid Mech., 149:20–27. 57
- Verbeeten, W., Peters, G., and Baaijens, F. (2002). Viscoelastic analysis of complex polymer melt flows using the extended pom-pom model. J. Non-Newtonian Fluid Mech., 108:301–326. 13
- Verhoef, M., van den Brule, B., and Hulsen, M. (1999). On the modelling of a pib/pb boger fluid in extensional flow. J. Non-Newtonian Fluid Mech., 80:155–182. 34
- Vvedensky, D. (2004). Multiscale modeling of nanostructures. J. Phys.: Condens. Matter, 16:R1537. 3
- Wales, J. (1976). The application of flow birefringence to rheological studies of polymer melts. PhD Thesis, Delft University of Technology. 14, 20
- Wapperom, P., Keunings, R., and Legat, V. (2000). The backward-tracking lagrangian particle method for transient viscoelastic flows. J. Non-Newtonian Fluid Mech., 91:273–295. 56, 57
- Warner, H. (1972). Ind. Eng. Chem. Fundam., 11. 6
- White, D. and Tallmadge, J. (1965). Theory of drag out of liquids on flat plates. Chem. Eng. Sci., 20:33–37. 86, 123
- Wiest, J. and Tanner, R. (1989). Rheology of bead-nonlinear spring chain macromolecules. J. Rheology, 33:281–316. 61
- Woo, N., Shaqfeh, E., and Khomami, B. (2004a). The effect of confinement on the dynamics and rheology of dilute dna solutions. part i: Effective rheology and single chain dynamics. J. Rheology, 48:299. 35

- Woo, N., Shaqfeh, E., and Khomami, B. (2004b). The effect of confinement on the dynamics and rheology of dilute dna solutions. part i: Entropic spring force under confinement and numerical algorithm. J. Rheology, 48:281. 35
- Yang, B. and Khomami, B. (1999). Simulation of sedimentation of a sphere in a viscoelastic fluid using molecular based constitutive models. J. Non-Newtonian Fluid Mech., 82:429–452. 33, 34, 38, 56, 58, 62, 64, 68, 69, 76
- Yourdon, E. (1989). Modern Structured Analysis. Englewood Cliffs, New Jersey, Yourdon Press. 1
- Yurun, F. and Crochet, M. (1995). Higher order finite element method for steady viscoelastic flows. J. Non-Newtonian Fluid Mech., 57:283–311. 94

# Vita

Arash Abedijaberi was born in Isfahan, Iran on April 27, 1981. He was among top 1% Iranian students who were selected in a nationwide entrance examination to pursue their high school studies in National Organization for Development of Exceptional Talents (NODET). Then, he ranked 51 among 600,000 participants in National Entrance Exam for Universities and Colleges in Iran in 1999. Arash graduated from the University of Tehran, Iran, with First Class Honors in Biotechnology, in May, 2005. In the same year he joined the Washington University in St. Louis to pursue his PhD in Chemical Engineering and subsequently followed his PhD advisor, Dr. Bamin Khomami, to University of Tennessee in Knoxville in August 2007.